FIRST PRINCIPLES MODELING AND TIME-RESOLVED CIRCULAR DICHROISM SPECTROSCOPY OF THE FENNA-MATTHEWS-OLSON COMPLEX

by

Zach Mitchell

A Dissertation

Submitted to the Faculty of Purdue University

In Partial Fulfillment of the Requirements for the degree of

Doctor of Philosophy

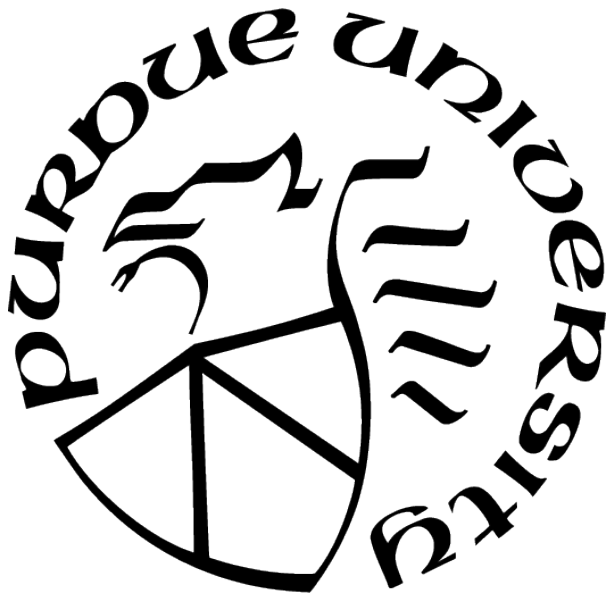

Department of Physics and Astronomy

West Lafayette, Indiana

December 2022

THE PURDUE UNIVERSITY GRADUATE SCHOOL
STATEMENT OF COMMITTEE APPROVAL

Dr. Sergei Savikhin, Chair

Department of Physics and Astronomy

Dr. Yulia Pushkar

Department of Physics and Astronomy

Dr. David Nolte

Department of Physics and Astronomy

Dr. Andrew Hirsch

Department of Physics and Astronomy

Approved by:

Dr. Gabor Csathy

I dedicate the next 100+ pages to myself. This has been a marathon, and I will thank a lot of people for their support, but in the end it was my stubborn need to prove to myself that I could endure and succeed that got me to the end.

ACKNOWLEDGMENTS

This journey has been a long one, one that has been dotted with many productive and supportive relationships, as well as many hardships. The early years would not have been possible without the camaraderie of my cohort, namely Dr. Ian Christie, Dr. Julien Varennes, and Dr. Darryl Masson. My entry into the research world would not have been possible without the mentoring of Dr. Dan Hartzler and Dr. Valentyn Stadnytskyi. For several years the only person sharing the lab with me was Dr. Antoine Martin, with whom many struggles, roadblocks, and small victories were shared. Sandy Formica has also been an institution of the Department of Physics and Astronomy, and every single student who interacts with her has had only good things to say.

The later years were some of the most difficult, but also the most enjoyable. I met another group of lifelong friends in Dr. Brandon Dzuba, Sydney Schieffer, Dr. John Banovetz, and Arnesh Daniel. Their friendship and support made the end of this process bearable. I also need to acknowledge the support of my family, who were there for me every step of the way. Playing another supporting role is Bardstown Bourbon Company, whose spirits were there to share my victories along the way.

Finally, I would be criminally negligent to leave out my partner Keri Good. Being the partner of a graduate student in the thesis writing process is not easy, but she handled it with patience and grace.

TABLE OF CONTENTS

LIST OF TABLES

LIST OF FIGURES

ABBREVIATIONS

BChl	bacteriochlorophyll
CD	circular dichroism
Chl	chlorophyll
DADS	decay-associated difference spectrum
FMO	Fenna-Matthews-Olson complex
PS I	Photosystem I
TRCD	time-resolved circular dichroism
WT	wild-type

ABSTRACT

The Fenna-Matthews-Olson (FMO) complex is a photosynthetic pigment-protein complex that has been the subject of study of decades of research, both experimental and theoretical. The FMO complex is small enough that computational modeling is feasible, while the rich excitonic interactions between the pigments give rise to absorption and circular-dichroism (CD) spectra with many interesting details. This makes FMO an excellent testing ground for new predictive modeling techniques.

In this work we model the FMO complex from first-principles, wherein the only input is the X-ray crystal structure of the protein. We compute steady-state absorption and CD spectra of wild-type (WT) FMO as well as two mutants, Y16F and Q198V, in which amino acid residues near pigment 3 and pigment 7 are replaced respectively. CD spectra contain extra structural information and thus provide another avenue of investigation into the electronic properties of the FMO complex. We find that while there are large structural changes in the mutants, not all of the structural changes produce significant spectral changes. We conclude that the primary contributor to the spectral changes in Y16F is the breaking of a hydrogen bond between the nearby tyrosine and pigment 3. On the other hand, the spectral changes in Q198V are due to a collection of effects cancelling one another out to varying degrees, all induced by widespread structural changes as a result of the mutation.

We then perform time-resolved absorption and CD spectroscopy measurements on WT, Y16F, and Q198V FMO to provide a high quality set of experimental data against which the first-principles spectra can be validated. We find that in order to accurately model the triplet energy transfer dynamics in FMO two effects must be accounted for in the modeling: (1) the Stark shift caused by the rotation of the bacteriochlorophyll's permanent dipole moment upon entering a triplet state, and (2) decays must be modeled as Boltzmann populations rather than individual pigments.

1. INTRODUCTION

Global energy consumption in 2020 was about 18 terrawatts (TW) on average [1]. This is not without consequence, as the concentration of greenhouse gases such as carbon dioxide, methane, and nitrous oxide have reached concentrations unseen for at least 800,000 years [2]. This is projected to cause more intense weather events, acidification of the oceans, increased temperatures on both the surface and in the oceans, as well as a rise in the global sea level [2]. Mitigating the worst effects of climate change requires significant reductions in greenhouse gas emissions over the next few decades, and near elimination of greenhouse gas emissions by the end of the century [2]. Despite the dangers of climate change, global energy consumption is predicted to reach 50 TW by 2050 [3].

Investments in renewable energy have generally increased, and in regions like Africa, Central America, and South America, renewable energy is projected to be the largest share of increased energy production between 2019 and 2030 [4]. Furthermore, growth in renewable energy is driven primarily by solar and wind from utility-scale developments [4]. Estimates place the amount of harvestable wind energy at 72 TW after accounting for theoretical limits in turbine efficiency, the required wind speeds to turn the blades of turbines, the area on land and offshore where turbines can be built, and a variety of other factors [5].

On the other hand, solar energy is the most abundandant energy resource on Earth, with over 100,000 TW of solar radiation reaching the Earth [5]. As such, there has been great interest in light harvesting technologies. One method of solar energy collection is photovoltaics (PV), which use semiconductors to convert light directly into electricity [5]. The estimate for the amount of solar energy harvestable by photovoltaics is 380 TW [5]. It would seem then that PV are a silver bullet for the world's energy production needs. Unfortunately, while PV produce no greenhouse gases during their operation, the rest of the lifecycle must still be considered. The production of PV involves mining rare earth minerals, the use of corrosive and carcinogenic chemicals, and the emission of several heavy metals [6].

Fortunately, nature developed a method of harnessing solar energy billions of years ago: photosynthesis [7].

In this thesis I will present the first time-resolved circular-dichroism measurements of mutants of the Fenna-Matthews-Olson (FMO) complex, a protein involved in the photosynthetic apparatus of the green sulfur bacteria *Chlorobium tepidum*. I will also present simulated absorption and circular-dichroism spectra computed from Hamiltonians that were obtained from first-principles simulations. I will also present progress towards a shot-noise limited femtosecond time-resolved circular-dichroism spectrometer that, when completed, could be used to further investigate the singlet state dynamics of the FMO complex. I will conclude with measurements clarifying the nature of a long-living state in a Photosystem I double-mutant whose picosecond dynamics were presented in a previous work [8]. By bringing together experiment and first principles theory to study the FMO complex, this work provides the opportunity to develop predictive modeling that is applicable to a wide variety of systems.

1.1 Photosynthesis

The FMO complex is just one pigment-protein complex involved in the photosynthetic apparatus of the green sulfur bacteria *C. tepidum*. To understand its function in this apparatus we must first understand the larger picture of photosynthesis and the various processes involved.

Life on Earth began roughly 3.5 billion years ago [9]. 1.5 billion years later oxygen began to accumulate in Earth's atmosphere as a result of photosynthesis in cyanobacteria [9], [10]. Photosynthesis is responsible for producing the sugars, carbohydrates, lipids, and proteins that serve as food for other living creatures [9]. Thus, photosynthesis serves as a process for converting an abundant but inaccessible resource (sunlight) into an accessible source of food for life on Earth.

Photosynthesis is the process by which plants, algae, and bacteria convert light into chemical energy [9]. The overall reaction in plants is

$$n\,(\mathrm{H_2O}) + n\,(\mathrm{CO_2}) \xrightarrow{\hbar\omega} (\mathrm{CH_2O})_n + n\,(\mathrm{O_2})$$

and is ∼30% energy efficient in reducing a mole of CO_2 to a mole of glucose [9]. As shown above, the electron donor is water in plants and some bacteria as both plants and these bacteria perform *oxygenic* photosynthesis. *Anoxygenic* photosynthesis as performed by green sulfur bacteria (GSB) such as *C. tepidum* and purple bacteria may use other compounds such as H_2S as the electron donor [9].

The reaction equation above is highly simplified. The process of photosynthesis may be broken up into *light reactions* and *dark reactions* based on whether the reaction requires light as an input [9]. The light reactions in *C. tepidum* involve the cooperation of several pigment-protein complexes, including the FMO complex. In order to understand the role of the FMO complex we must first examine photosynthetic apparatus of *C. tepidum*.

1.1.1 The Fenna-Matthews-Olson Complex of the Green Sulfur Bacteria *C. Tepidum*

The green sulfur bacteria *Chlorobium tepidum* (*C. tepidum*) is found 145m under water in the Black Sea and is particularly well suited for survival in low light conditions [11]. The photosynthetic machinery of *C. tepidum* are shown in Figure 1.1. The large peripheral antenna complex is called the *chlorosome*, and it consists of up to 200,000 BChl *c* pigments depending on light conditions [9], [12]. Chlorosomes are the largest and most pigment-dense light harvesting antennas found in nature [13]. The chlorosome is attached to the membrane indirectly through a protein *baseplate* [9]. The baseplate contains a trimeric BChl *a* protein complex called the Fenna–Matthews–Olson (FMO) complex, which will be examined in greater detail shortly and is the primary subject of study in this work [9]. In the membrane is a Type I reaction center where the primary electron donor is a pair of BChl *a* pigments that absorb maximally at 840nm [14].

Reaction centers can be classified as either Type I or Type II based on the identity of the terminal electron acceptor [15], [16]. Type I reaction centers are found in both plants and green sulfur bacteria such as *C. tepidum* and employ iron-sulfur clusters as the terminal electron acceptor [15], [16]. Type II reaction centers are found in plants, cyanobacteria, and purple bacteria and employ quinones as the terminal electron acceptor [15], [16].

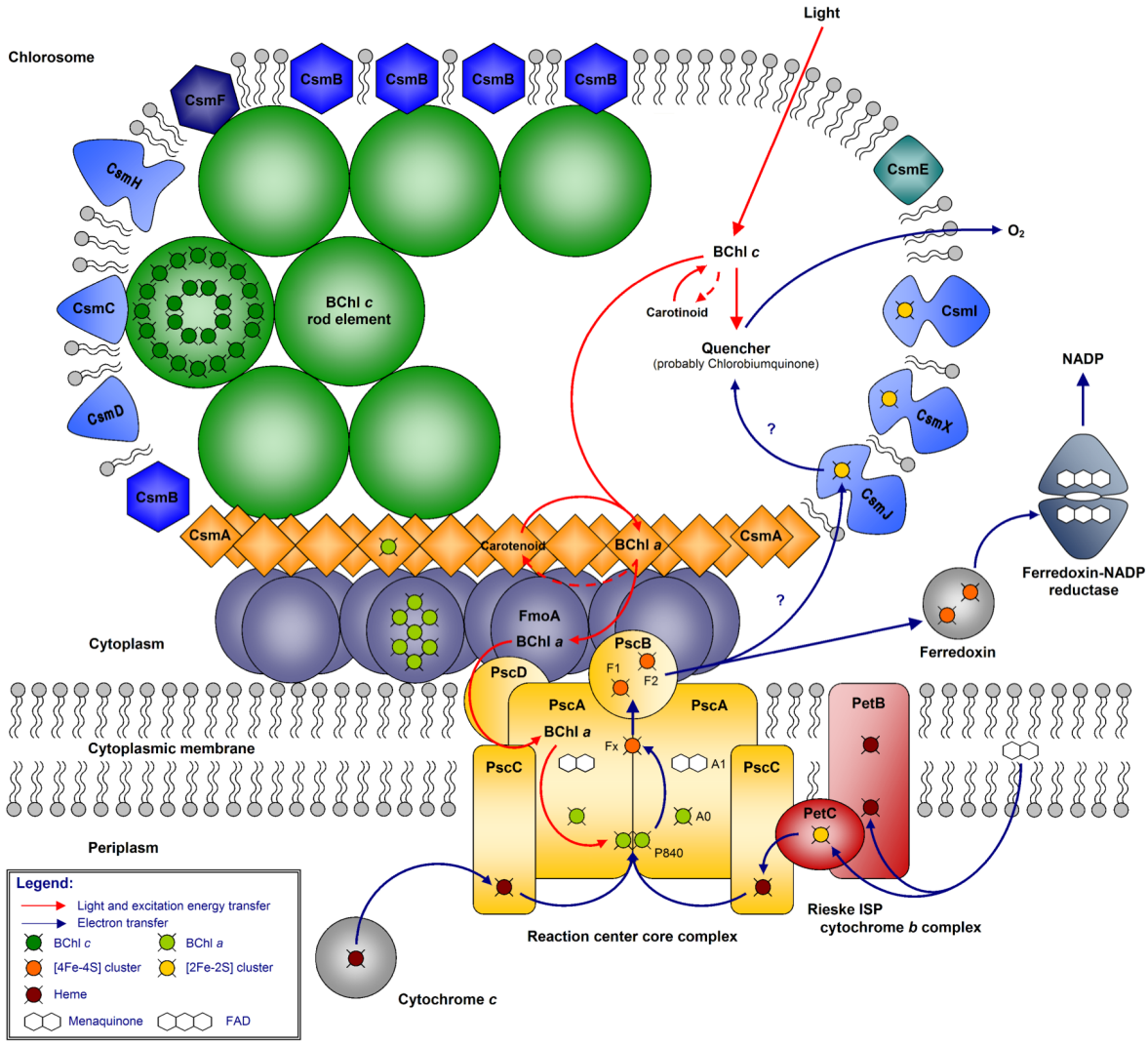

Figure 1.1. Chlorosome, baseplate, and reaction center in the green sulfur bacteria *C. tepidum*. The FMO complex exists in the baseplate through which the chlorosome is attached to the membrane. Image from [17].

The chlorosome absorbs maximally in the 720–750 nm range, but the red edge of the absorption band extends to ∼800 nm [18]. Excitation energy from absorbed light is transferred first between pigments in the chlorosome, then through the FMO complex in the baseplate, and finally to the reaction center [14]. The baseplate maximally absorbs at 795 nm and is made of BChl *a* dimers[18]. This energy transfer from chlorosome to reaction center is driven by a downhill energy gradient both inside the chlorosome and between the chlorosome and the baseplate [13].

The existence of the FMO complex was discovered in 1962 by John Olson at Brookhaven National Laboratory [19]. The atomic structure of the FMO complex was determined by x-ray crystallography in 1979 with a resolution of 2.8Å, making it the first photosynthetic protein to have its structure determined [19]. A more recent structure commonly used for modeling today is known to 2.2Å resolution [20]. The existence of high quality structures allows first principles modeling such as the work presented here and in [20]. The protein sequence was determined in 1992 [19]. The structure of the FMO complex is shown in Fig. 1.2.

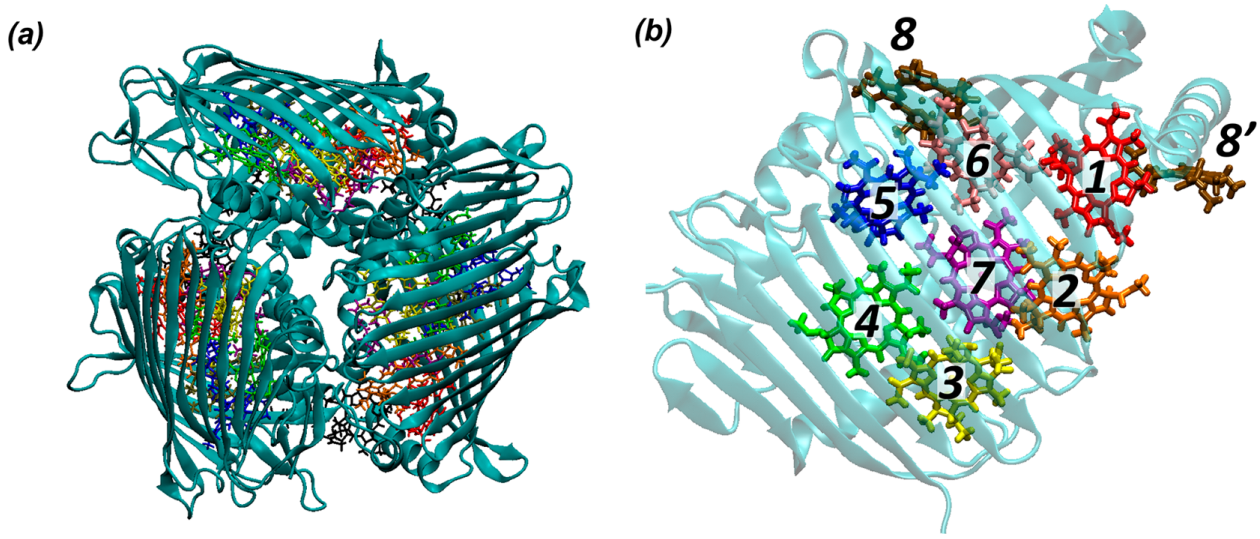

Figure 1.2. The Fenna-Matthews-Olson complex. **(a)** The protein itself is a trimeric complex with a C3 rotational symmetry. **(b)** Each monomer contains 8 pigments, with the 8th pigment lying closer to the next monomer over. Image from [20].

The FMO complex is found in *C. tepidum*, but also in other green sulfur bacteria such as *Prosthecochloris aestuarii*, *Chlorobium limicola*, and *Pelodictyon phaeum* [21]–[23]. The FMO complex is a homotrimer with C3 rotational symmetry, where each monomer contains 8 BChl *a* pigments [24]. Of the 8 pigments, 7 are arranged within a few angstroms of one another, while the 8th pigment is situated further away, closer to the neighboring monomer. The tight packing of pigments into the protein complex means that the pigments are strongly coupled, leading to excitations that are delocalized over multiple pigments [24]. The theory behind these delocalized excitations, called *excitons*, will be discussed in a later section.

The FMO complex is one of the most well-studied photosynthetic proteins. The FMO complex strikes a balance between simplicity and complexity that makes it an interesting system to study while remaining practical to model. With only 8 pigments the system is much simpler than a system like the cholorosome, which contains 200,000 pigments. However, the rich excitonic structure, interactions between the pigments and the surrounding protein, and size of the protein make computational modeling difficult. Quantum mechanical simulations have only become feasible within the last few years.

As mentioned previously, in addition to the experimental measurements and computational modeling of the FMO complex, we have also measured one of the long living states in a double-mutant of plant Photosystem I. An understanding of the photosynthetic machinery in plants is therefore necessary background for the discussion of that work.

1.1.2 Photosynthetic Machinery of Plants

Photosynthesis in plants takes place in organelles called *chloroplasts* [25]. Inside of the chloroplast is a region called the *stroma*, which contains the *thylakoid membrane*, which encloses a region called the *lumen* [25]. Protein complexes embedded in the membrane build up a gradient of hydrogen ions across the membrane through a variety of reactions shown in Figure 1.3. This gradient is used to drive the synthesis of ATP [9]. The photosystems of plants and bacteria follow the same general structure in that they have a *peripheral antenna*, a *core antenna*, and a *reaction center* [9]. The antenna complexes contain various forms of chlorophyll (Chl) or bacteriochlorophyll (BChl), depending on the organism [9].

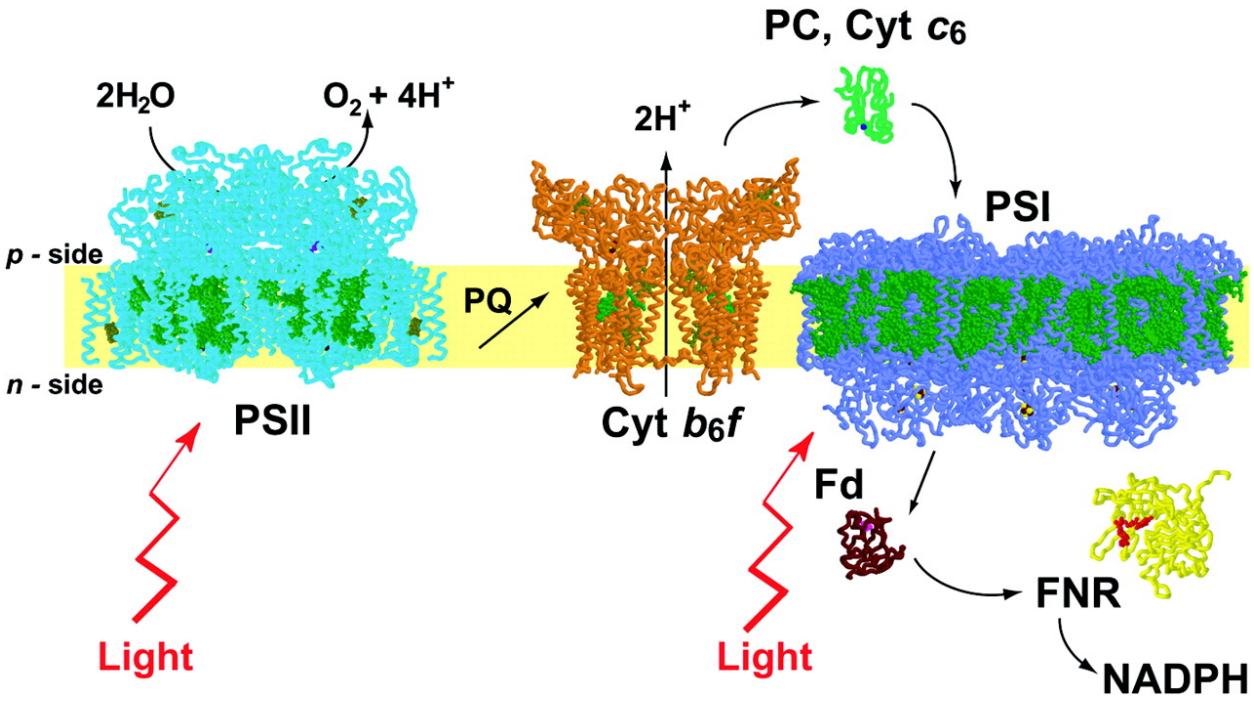

Figure 1.3. Photosynthetic pigment protein complexes embedded in the thylakoid membrane (yellow). Photosystem I (blue), Photosystem II (teal), and Cytochrome b_6f (orange) power the light reactions. Image from [26].

Energy is funneled from the peripheral antenna to the core antenna and then to the reaction center, where charge separation and electron transfer takes place [9]. These energy transfer mechanisms are the primary focus of this work.

The energy transfers that take place in both Photosystem I and the FMO complex are ultimately triggered by the absorption of light in a remote antenna complex. Furthermore both Photosystem I and the FMO complex contain strongly coupled molecules. Therefore a theoretical description of the absorption of light by strongly coupled molecules is necessary for understanding both systems.

1.2 Theoretical Background

The BChl *a* pigments in the FMO complex are coupled strongly enough that they cannot be modeled as isolated systems. This strong coupling leads to delocalization of excited states across multiple pigments. We will work up to the theoretical description of this strongly cou-

pled system by beginning with the theoretical description of how a single pigment absorbs light as the primary method of investigation in this work is spectroscopic techniques and the absorption of light is central to photosynthesis. We will then develop the theory for describing the excited states of strongly coupled molecules. Finally, we will describe the interaction of these strongly coupled systems with circularly polarized light as the work presented here employs time-resolved circular-dichroism spectroscopy. This is particularly interesting because differences in the absorption of circularly polarized light can reveal structural information about a system.

1.2.1 Perturbation of a Two-Level System

Consider an isolated single molecule such as a single BChl a pigment. The Schrödinger equation for the system is

$$i\hbar\frac{\partial\Psi}{\partial t} = H\Psi \tag{1.1}$$

The solutions of (1.1) are the stationary states with energies E_i and wavefunctions in (1.2).

$$\Psi_i = \psi_i(\mathbf{r})e^{-iE_it/\hbar} \tag{1.2}$$

For simplicity, we will restrict the analysis to just two states, Ψ_a and Ψ_b with $E_a < E_b$, so that the molecule resembles a two-level system. If prepared in one of these stationary states, the system will forever remain in that state.

However, we are primarily interested in transitions between these two states such as in the case of energy transfer, electron transfer, or the absorption of light, so we must make a small perturbation to the system that makes the wavefunctions in (1.2) no longer stationary states. We will write the new Hamiltonian as $H = H_0 + H'$, where H_0 is the Hamiltonian of the isolated molecule in (1.1). In this small-perturbation scenario, the Heitler-London approximation allows the new stationary states Ψ' to be written as superpositions of the original stationary states [27].

$$\Psi' = c_a(t)\psi_a(\mathbf{r})e^{-iE_at/\hbar} + c_b(t)\psi_b(\mathbf{r})e^{-iE_bt/\hbar} \tag{1.3}$$

Obtaining the stationary states of the perturbed system amounts to choosing the appropriate $c_i(t)$. Placing (1.3) into (1.1) yields (1.4)–(1.6).

$$\dot{c}_a = -\frac{i}{\hbar}\left[c_aH'_{aa} + c_bH'_{ab}e^{-i(E_b-E_a)t/\hbar}\right] \tag{1.4}$$

$$\dot{c}_b = -\frac{i}{\hbar}\left[c_bH'_{bb} + c_aH_{ba}e^{-i(E_a-E_b)t/\hbar}\right] \tag{1.5}$$

$$H'_{ij} \equiv \langle\psi_i|H'|\psi_j\rangle \tag{1.6}$$

If $H'_{ii} = 0$, (1.4) and (1.5) may be simplified to (1.7) and (1.8).

$$\dot{c}_a = -\frac{i}{\hbar}H'_{ab}e^{-i\omega_0t}c_b \tag{1.7}$$

$$\dot{c}_b = -\frac{i}{\hbar}H'_{ba}e^{i\omega_0t}c_a \tag{1.8}$$

$$\omega_0 \equiv (E_b - E_a)/\hbar \tag{1.9}$$

If the system is prepared entirely in ψ_a at $t = 0$ then $c_a(0) = 1$ and $|c_b(t)|^2$ represents the probability that the system has made the transition into ψ_b. The first order approximation of $c_b(t)$ is found by asserting that $c_b(t)$ is small and thus that $c_a(t) = 1$. This approximation leads to (1.10), but further progress requires knowledge of the form of H'.

$$c_b(t) = -\frac{i}{\hbar}\int_0^t H'_{ba}(t')e^{i\omega_0t'}dt' \tag{1.10}$$

Now consider a perturbation with an arbitrary spatial dependence and an oscillating time component as shown in (1.11). Such is the case for the interaction of a single molecule with an oscillating electric field.

$$H' = V(\mathbf{r})\cos(\omega t) \tag{1.11}$$

The cannonical example of this type of perturbation is the interaction of a single molecule with an external electric field, but it could also represent nuclear vibrations within the molecule or from the surrounding environment. Plugging (1.11) into (1.6) yields the matrix elements in (1.12).

$$H'_{ij} = V_{ij}\cos(\omega t) \tag{1.12}$$

$$V_{ij} \equiv \langle \psi_i \,|\, V(\mathbf{r}) \,|\, \psi_j \rangle \tag{1.13}$$

Placing (1.12) into (1.10), we obtain the solution for $c_b(t)$ in (1.14).

$$c_b(t) \approx -i\frac{V_{ba}}{\hbar}\frac{\sin\left[(\omega_0-\omega)t/2\right]}{(\omega_0-\omega)}e^{i(\omega_0-\omega)t/2} \tag{1.14}$$

The transition probability $P_{a\to b}(t)$ is then given by $|c_b(t)|^2$, as shown in (1.15).

$$P_{a\to b}(t) = |c_b(t)|^2 \approx \frac{|V_{ba}|^2}{\hbar^2}\frac{\sin^2\left[(\omega_0-\omega)t/2\right]}{(\omega_0-\omega)^2} \tag{1.15}$$

There is a resonance between the frequency of the transition and the frequency of the perturbation. In the next section we will examine the particular case of an oscillating electric field and we will see that this resonance determines the frequency of light that is most likely to drive the transition.

In the case of a single molecule interacting with an oscillating electric field we know the particular form of $V(\mathbf{r})$ so the theory can be further developed.

1.2.2 Interaction of a Single Molecule with an Oscillating Electric Field

Suppose that the oscillating perturbation is an electric field. The energy of a collection of charges (a molecule, for example) in an electric field may be decomposed into its multipole expansion [28]:

$$U = qV(0) - \boldsymbol{\mu}\cdot\mathbf{E} + \frac{1}{6}\sum_i\sum_j Q_{ij}\frac{\partial E_j}{\partial x_i} + \ldots \tag{1.16}$$

The total charge of a molecule is typically zero, so the first term vanishes. The next lowest term is the dipole term. The remaining terms are higher order and typically very small, so they may be ignored. Thus, the dominant contribution to the interaction energy comes from the dipole interaction:

$$U \approx -\boldsymbol{\mu} \cdot \mathbf{E} \tag{1.17}$$

Placing (1.17) into (1.11) yields the expression for the matrix elements H'_{ij}.

$$\begin{aligned} H' &= V(\mathbf{r})\cos(\omega t) = (-\boldsymbol{\mu} \cdot \mathbf{E})\cos(\omega t) && (1.18)\\ \boldsymbol{\mu} &\equiv e\mathbf{r} && (1.19)\\ H'_{ij} &= V_{ij}\cos(\omega t) = -\left(\boldsymbol{\mu}_{ij} \cdot \mathbf{E}\right)\cos(\omega t) && (1.20)\\ V_{ij} &= -\boldsymbol{\mu}_{ij} \cdot \mathbf{E} && (1.21)\\ \boldsymbol{\mu}_{ij} &\equiv e\langle\psi_i|\mathbf{r}|\psi_j\rangle && (1.22) \end{aligned}$$

The quantity described in (1.22) is the *transition dipole moment*, which plays a central role in determining the magnitude of the interaction with the electric field via the dot product in (1.20). The transition dipole moment is commonly quoted in the literature in units of *debyes* (D). One debye is 3.336×10^{-30} C m in SI units. For comparison, the transition dipole moment of two electrons separated by 1 Å is 4.803 D. Placing (1.21) in (1.15) yields the transition probability for the molecule in the electric field.

$$P_{a\to b}(t) = \left(\frac{|\boldsymbol{\mu}_{ba} \cdot \mathbf{E}|}{\hbar}\right)^2 \frac{\sin^2\left[(\omega_0 - \omega)t/2\right]}{(\omega_0 - \omega)^2} \tag{1.23}$$

As mentioned above, the transition probability is highest when the oscillation frequency of the electric field, ω, is equal to ω_0.

With the theory of interactions between light and a single molecule developed we may now describe the absorption of light by a single molecule as would be the case with a BChl *a* pigment in the FMO complex under illumination.

1.2.3 Absorption of Light by a Single Molecule

A quantity related to the transition dipole moment is the *dipole strength* of the transition, D_{ij}:

$$D_{ij} = \left|\boldsymbol{\mu}_{ij}\right|^2 = \left|\langle \psi_i \,|\, \boldsymbol{\mu} \,|\, \psi_j \rangle\right|^2 \tag{1.24}$$

The dipole strength is related to the molar extinction coefficient ε_{ij} ($\mathrm{M}^{-1}\,\mathrm{cm}^{-1}$) through (1.25)

$$D_{ij} \approx 9.186 \times 10^{-3} \left(\frac{n}{f^2}\right) \int \frac{\varepsilon_{ij}(\nu)}{\nu} d\nu \frac{\mathrm{D}^2}{\mathrm{M}^{-1}\,\mathrm{cm}^{-1}} \tag{1.25}$$

where n is the refractive index of the medium and f is a local-field correction factor.

The integral in (1.25) is performed over the broadened absorption band associated with the $i \rightarrow j$ transition. The local-field correction adjusts the field around the molecule to account for the properties of the surrounding dielectric medium [29]. A common model used to calculate this local-field correction is that of a point dipole in an empty spherical cavity in a linear isotropic medium.

The molar extinction coefficient can be measured experimentally with a spectrometer. The spectrometer obtains the absorption $A(\lambda)$ by measuring the intensity of a beam of light before and after the sample. The absorption is related to $\varepsilon(\lambda)$ through (1.26)

$$A(\lambda) = \varepsilon(\lambda) C \ell = -\log\left(\frac{I(\lambda)}{I_0(\lambda)}\right) \tag{1.26}$$

where C is the concentration of the sample (mol/L) and ℓ is the optical path length in cm.

Thus, with (1.26) we have connected a microscopic, quantum-mechanical property of the molecule (the transition dipole moment) to an easily measured, macroscopic property (the absorption).

The theory thus far has been focused on either a single molecule or a collection of non-interacting molecules. As mentioned previously, the BChl *a* pigments in FMO are strongly interacting so we must extend the theory to account for these strong interactions. These strong interactions give rise to delocalized excitations called *excitons*.

1.2.4 Absorption of Light by Molecular Excitons

The theory of excitons was originally developed by Yakov Frenkel in 1931 as part of his work describing how light is converted to heat in solids [30]. He noted that light is converted into heat in a monatomic gas when an atom absorbs light, becomes excited, and then inelastically collides with a second atom, increasing the translational kinetic energy of the second atom. However, a solid is modeled as a set of uncoupled harmonic oscillators, and heat in the solid is modeled as the vibrational levels of these oscillators. A photon at 532nm is ∼2eV, whereas k_BT at room temperature is 25meV, so the excitation is ∼100x larger. Transferring this excitation to a nearby atom would require the nearby atom to jump 100 vibrational levels, which isn't possible if the oscillators are harmonic [30]. He also notes that perhaps the excitation could be shared amongst several atoms in the lattice, but that isn't possible if the "oscillators" are uncoupled. What follows is Frenkel's solution to this problem applied to strongly interacting molecules rather than the atoms in a crystal lattice.

We begin with a pair of interacting molecules (such as two BChl *a* pigments in the FMO complex), each of which is a two-level system. A pair of interacting molecules is referred to as a *dimer*. Each molecule in isolation has the Schrödinger equation shown in (1.27)

$$H_i\varphi_i^{(k)} = E_i^{(k)}\varphi_i^{(k)} \tag{1.27}$$

where $\varphi_i^{(k)}$ refers to the wavefunction of molecule i in state k. Let a and b refer to the lower and upper of the $k = 2$ states of each molecule in our dimer respectively.

When the interaction is introduced, we assume that the interaction is weak enough that the new stationary states may be constructed from linear combinations of products of the $\varphi_i^{(k)}$, as shown in (1.28) and (1.29).

$$\Psi_A = \varphi_0^{(a)}\varphi_1^{(a)} \tag{1.28}$$

$$\Psi_B = c_0\varphi_0^{(b)}\varphi_1^{(a)} + c_1\varphi_0^{(a)}\varphi_1^{(b)} \tag{1.29}$$

We also stipulate that there is no exchange of electrons between the molecules in the dimer so that we don't have to antisymmetrize the wavefunctions.

We obtain the energies of the dimer by placing Ψ_A and Ψ_B into the Schrödinger equation that includes individual molecule Hamiltonians and the interaction term H'.

$$(H_0 + H_1 + H')\,\Psi_A = E_A\Psi_A \tag{1.30}$$

$$(H_0 + H_1 + H')\,\Psi_B = E_B\Psi_B \tag{1.31}$$

Multiplying (1.30) from the left with $\langle\Psi_A|$ we get (1.32) for the energy of the new ground state.

$$E_A = E_0^{(a)} + E_1^{(a)} + \left\langle \varphi_0^{(a)}\varphi_1^{(a)}\,|H'|\,\varphi_0^{(a)}\varphi_1^{(a)} \right\rangle \tag{1.32}$$

The last term in (1.32) is referred to as the *displacement energy*, as it simply shifts or *displaces* the energy of the ground state relative to the case where there is no interaction. The displacement energy is typically small, and may be ignored [24].

The energy of the upper state is obtained in a similar manner. Multiplying (1.31) from the left with $\langle\varphi_0^{(b)}\varphi_1^{(a)}|$ or $\langle\varphi_0^{(a)}\varphi_1^{(b)}|$ yields (1.33) or (1.34) respectively.

$$c_0\left(E_0^{(b)} - E_B\right) + c_1 H'_{01} = 0 \tag{1.33}$$

$$c_0 H'_{10} + c_1\left(E_1^{(b)} - E_B\right) = 0 \tag{1.34}$$

$$\left\langle \varphi_i^{(b)}\varphi_j^{(a)}\,|H'|\,\varphi_j^{(b)}\varphi_i^{(a)} \right\rangle \equiv H'_{ij} \tag{1.35}$$

This can be reformulated as a matrix equation as shown in (1.36).

$$\begin{pmatrix} E_0^{(b)} & H'_{01} \\ H'_{10} & E_1^{(b)} \end{pmatrix} \begin{pmatrix} c_0 \\ c_1 \end{pmatrix} = E_B \begin{pmatrix} c_0 \\ c_1 \end{pmatrix} \tag{1.36}$$

What appear on the diagonal of the Hamiltonian matrix are just the individual excited state energies of the molecules, while the off-diagonal elements are the interaction terms between the molecules.

This is an eigenvalue problem with two solutions. The energies are shown in (1.37),

$$E_{B\pm} = E_B^0 \pm \frac{1}{2}\sqrt{\delta^2 + 4\left(H'_{01}\right)^2} \tag{1.37}$$

$$E_B^0 \equiv \left(E_0^{(b)} + E_1^{(b)}\right)/2 \tag{1.38}$$

$$\delta \equiv E_0^{(b)} - E_1^{(b)} \tag{1.39}$$

and the eigenvectors (c_0 and c_1) are shown in (1.40).

$$\Psi_{B\pm} = c_{0\pm}\varphi_0^{(b)}\varphi_1^{(a)} \pm c_{1\pm}\varphi_0^{(a)}\varphi_1^{(b)} \tag{1.40}$$

$$c_{0\pm} = \sqrt{\frac{1 \pm s}{2}}\,,\; c_{1\pm} = \sqrt{\frac{1 \mp s}{2}} \tag{1.41}$$

$$s = \delta/\sqrt{\delta^2 + 4\left(H'_{01}\right)^2} \tag{1.42}$$

From (1.40) one can predict whether the excitation will reside mostly on one pigment or whether it will be more equally shared. When the molecules have very similar energies, then $\delta \to 0$ and $s \to 0$. In this case both $c_{0\pm} \to \sqrt{1/2}$ and the excitation is shared equally between the molecules. When one molecule has a much larger energy than the other, say $E_0^{(b)} \gg E_1^{(b)}$, then $\delta \gg H_{12}$ and $s \to 1$. In this case $c_{0+} \to 1$ and $c_{1+} \to 0$ (or vice versa for c_{0-} and c_{1-}) and the excitation resides predominantly on one molecule at a time. In all cases, the upper energy level E_B is split around the average energy E_B^0 with a splitting determined by the magnitude of the interaction and the difference between individual molecule energies. This splitting is illustrated in Figure 1.4.

The transition dipole moment, and thus the dipole strength, also experiences a split.

$$\boldsymbol{\mu}_{BA\pm} = c_{0\pm}\boldsymbol{\mu}_{0,ba} + c_{1\pm}\boldsymbol{\mu}_{1,ba} \tag{1.43}$$

$$D_{BA\pm} = \left|\boldsymbol{\mu}_{BA\pm}\right|^2 = \left(c_{0\pm}\right)^2 D_{0,ba} + \left(c_{1\pm}\right)^2 D_{1,ba} + 2c_{0\pm}c_{1\pm}^*\left(\boldsymbol{\mu}_{0,ba}\cdot\boldsymbol{\mu}_{1,ba}\right) \tag{1.44}$$

In (1.44) we see that dipole strengths of the D_{BA+} and the D_{BA-} transitions will be different, which means that the absorption of those two transitions will be different. The dipole strengths are now a weighted sum of the individual dipole strengths and there is now a term that takes into account the mutual orientation of the transition dipole moments. The

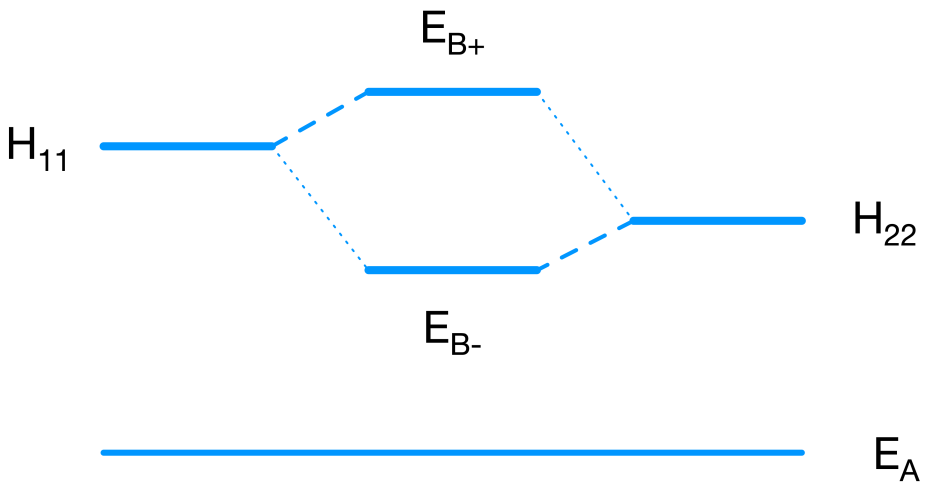

Figure 1.4. Excitonic splitting of two uncoupled transition energies H_{11} and H_{22} into excitonic transitions E_{B+} and E_{B-}.

transition dipole moments are also important for the interaction matrix elements H'_{ij}. For the case of interacting molecules, the interaction is the Coulomb interaction between two molecules. As before in (1.16), the dominant contribution to the interaction energy comes from the dipole interaction.

If the electric field in (1.17) is replaced with the electric field from another dipole (the other molecule in the dimer), one obtains interactions of the form shown in (1.45)

$$U = \frac{\boldsymbol{\mu}_0 \cdot \boldsymbol{\mu}_1 - 3\left(\boldsymbol{\mu}_0 \cdot \hat{\mathbf{R}}\right)\left(\boldsymbol{\mu}_1 \cdot \hat{\mathbf{R}}\right)}{R^3} \tag{1.45}$$

where $\mathbf{R}$ is the relative position vector from one molecule to the other. Placing (1.45) into (1.35) yields (1.46).

$$H'_{ij} = \frac{\boldsymbol{\mu}_{i,ba} \cdot \boldsymbol{\mu}_{j,ba} - 3\left(\boldsymbol{\mu}_{i,ba} \cdot \hat{\mathbf{R}}_{ij}\right)\left(\boldsymbol{\mu}_{j,ba} \cdot \hat{\mathbf{R}}_{ij}\right)}{R_{ij}^3} \tag{1.46}$$

Both (1.45) and (1.46) are sensitive to not only the angle between the two dipoles, but their placement relative to one another.

For example, two parallel dipoles placed side by side do not have the same energy compared to two parallel dipoles placed tip to tail, even if the distance between the dipoles is the same in both cases as shown in Figure 1.5.

This analysis is easily extended to larger systems consisting of N pigments. The wavefunctions take on the form shown in (1.47) and (1.48).

$$\Psi_A = \prod_k \varphi_k^{(a)} \tag{1.47}$$

$$\Psi_{B,k} = \sum_i c_{ik} \varphi_i^{(b)} \prod_{m \neq i} \varphi_m^{(a)} \tag{1.48}$$

The N–pigment system is comprised of an N–way superposition where the dimer was a 2-way superposition. With the dimer there were just two excitonic states (Ψ_{B+} and Ψ_{B-}) and it sufficed to label them with $+/-$. With N excitonic states we replace $\pm$ with the index $k = 1 \ldots N$. The $\{c_{ik}\}$ for a given excitonic state k contain the weights for each combination of wavefunctions with molecule i in its upper state and all others in their lower states.

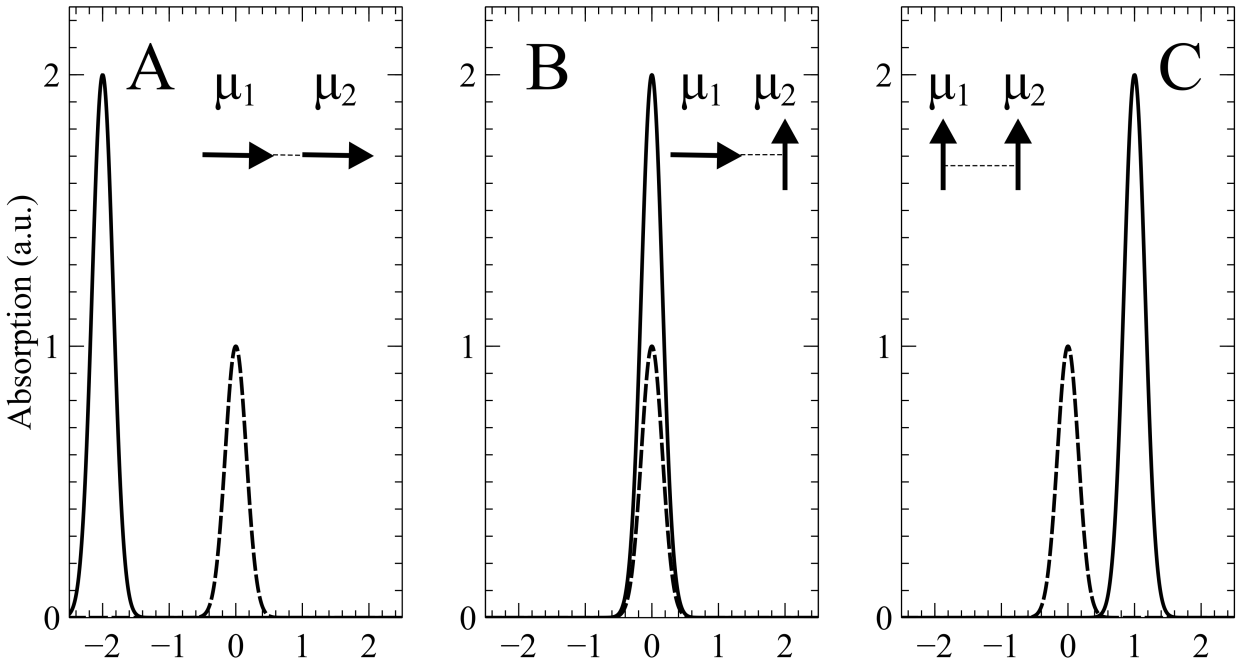

Figure 1.5. Effect of excitonic interactions on absorption band strength and placement for a homodimer. The absorption of each monomer (dashed) and excitonic band (solid) are shown for 3 different orientations of the transition dipole moments of the monomers. The orientation in A is referred to as a "J-aggregate," whereas the orientation in C is referred to as an "H-aggregate." The total dipole strength is conserved regardless of the orientation [28]. The excitonic bands have been given Gaussian band shapes with arbitrary bandwidths. Figure inspired by Figure 8.4 in [28].

The Hamiltonian takes the same form as shown in (1.36) but $N \times N$ rather than 2×2.

$$H_{ij} = \delta_{ij} E_i^{(b)} + H'_{ij} \tag{1.49}$$

If the c_{ik} are placed into a matrix $\mathbf{C}$, then determining the energies $E_{B,k}$ and weights c_{ik} reduces to diagonalizing the matrix $\mathbf{C}^{-1} \cdot \mathbf{H} \cdot \mathbf{C}$ shown in (1.50)

$$\mathbf{C}^{-1} \cdot \mathbf{H} \cdot \mathbf{C} = \mathbf{E}_B \tag{1.50}$$

where $\mathbf{E}_B$ is a diagonal matrix whose elements are the energies $E_{B,k}$. The matrix elements H'_{ij} are the same as those in (1.46).

The exciton dipole moments and dipole strengths are shown in (1.51) and (1.52) respectively

$$\boldsymbol{\mu}_k = \sum_i c_{ik} \boldsymbol{\mu}_{ba,i} \tag{1.51}$$

$$D_k = |\boldsymbol{\mu}_k|^2 = \sum_{i,j} c_{ik} c_{jk}^* \left(\boldsymbol{\mu}_{ba,i} \cdot \boldsymbol{\mu}_{ba,j} \right) = \boldsymbol{\rho}_k \mathbf{D} \tag{1.52}$$

where $\boldsymbol{\rho}_k$ is the density matrix for state k and $\mathbf{D}$ is the dipole strength matrix. It can be shown that the sum of all of the D_k is equal to the sum of the individual dipole strengths, so the excitonic interaction has the effect of redistributing the total dipole strength amongst the different excitonic transitions [24].

Thus far we have focused on the absorption of an excitonic system. Excitonic systems can also exhibit circular dichroism (CD), a difference in the absorption of circularly polarized light, even if the constituent molecules themselves do not exhibit CD. This is the case with the FMO complex as flat molecules such as BChl *a* do not exhibit CD. Excitonic CD is of particular interest because CD carries extra structural information that absorption does not, as will be described shortly. We will begin our treatment of excitonic CD by describing circularly polarized light.

1.2.5 Circularly Polarized Light

A plane-wave solution to Maxwell's equations is shown in (1.53).

$$\mathbf{E}(\mathbf{r},t) = \mathbf{E}_0 e^{i(\mathbf{k}\cdot\mathbf{r}-\omega t)} \tag{1.53}$$

If this wave propagates in the $\hat{\mathbf{z}}$ direction, the polarization lies in the xy–plane with a potentially arbitrary relative phase difference δ between the x- and y-components, as shown in (1.54).

$$\mathbf{E}(z,t) = \left(E_x\,\hat{\mathbf{x}} + e^{i\delta}E_y\,\hat{\mathbf{y}}\right)e^{i(kz-\omega t)} \tag{1.54}$$

The general case is $E_x \neq E_y$ and arbitrary δ. In this scenario the polarization vector traces out an ellipse in the plane of polarization, traversing the ellipse at angular frequency ω. The wave is said to be *elliptically polarized* [31].

When $\delta = n\pi$ for $n = 0, \pm1, \pm2, \ldots$ the x- and y-components oscillate either in phase or exactly out of phase. The polarization vector oscillates along a line at angle $\theta = \arctan(E_y/E_x)$ relative to the x-axis, and the wave is said to be *linearly polarized*.

When $E_x = E_y$ and $\delta = n\pi/2$ for $n = \pm1, \pm3, \ldots$ the polarization vector traces a circle in the plane of polarization, traversing the circle at angular frequency ω. In this scenario the wave is said to be *circularly polarized*. When looking along the direction of propagation, the wave is said to be *left-hand circularly polarized* (LCP) if the polarization vector rotates in the clockwise direction, and *right-hand circularly polarized* (RCP) if the polarization vector rotates counter-clockwise.

The equations for a circularly polarized plane wave are shown in (1.55) and (1.56), where the top signs refer to LCP and the bottom signs refer to RCP.

$$\mathbf{E}(z,t) = E_0\left(\hat{\mathbf{x}} + e^{\pm i\frac{\pi}{2}}\,\hat{\mathbf{y}}\right)e^{i(kz-\omega t)} \tag{1.55}$$

$$\mathbf{E}(z,t) = E_0\left[\cos(kz-\omega t)\,\hat{\mathbf{x}} \mp \sin(kz-\omega t)\,\hat{\mathbf{y}}\right] \tag{1.56}$$

1.2.6 Intrinsic Circular Dichroism of a Single Molecule

When $\varepsilon(\lambda)$ for a system is different for different polarizations of light, the system is said to exhibit *dichroism* [32]. A system with *linear dichroism* (LD) absorbs two perpendicular polarizations differently i.e. $\varepsilon_x \neq \varepsilon_y$. A system with *circular dichroism* (CD) absorbs LCP light and RCP light differently. The most common systems that exhibit CD are proteins and systems consisting of interacting pigments, but individual chiral molecules may exhibit their own "intrinsic" CD as well [24]. We will first focus on the CD of an individual molecule.

To understand the source of this intrinsic CD, we modify (1.17) to include the magnetic dipole moment.

$$U = -\boldsymbol{\mu} \cdot \mathbf{E} - \mathbf{m} \cdot \mathbf{B} \tag{1.57}$$

$$\mathbf{m} = \frac{e}{2mc} \sum_i (\mathbf{L}_i + 2\mathbf{S}_i) \tag{1.58}$$

The analysis that follows is simplified when the electromagnetic field is assumed to propagate in the z-direction, allowing us to rewrite the x- and y-components of $\boldsymbol{\mu}$ and $\mathbf{m}$ in terms of the LCP and RCP components of the field $\mathbf{e}_+$ and $\mathbf{e}_-$.

$$\boldsymbol{\mu} = \mu_- \hat{\mathbf{e}}_- + \mu_+ \hat{\mathbf{e}}_+ + \mu_z \hat{\mathbf{z}} \tag{1.59}$$

$$\mathbf{m} = m_- \hat{\mathbf{e}}_- + m_+ \hat{\mathbf{e}}_+ + m_z \hat{\mathbf{z}} \tag{1.60}$$

$$\mathbf{g} \equiv -i\mathbf{m} \tag{1.61}$$

The interaction elements V_{ij} then become

$$(V_\pm)_{ij} = -(\mu_\pm)_{ij} E_0 - (m_\pm)_{ij} B_0 \tag{1.62}$$

$$\mathbf{m}_{ij} \equiv \langle \psi_i | \mathbf{m} | \psi_j \rangle \tag{1.63}$$

Squaring (1.62) and averaging over all orientations yields (1.64)

$$(V_{\pm})_{ij}^2 = \frac{8\pi I}{3c}\left[\frac{D_{ij}}{n} + nG_{ij} \mp 2R_{ij}\right] \tag{1.64}$$

$$G_{ij} \equiv |\mathbf{g}_{ij}|^2 = \mathbf{m}_{ij} \cdot \mathbf{m}_{ji} \tag{1.65}$$

$$R_{ij} \equiv -\boldsymbol{\mu}_{ij} \cdot \mathbf{g}_{ij} = \mathrm{Im}(\boldsymbol{\mu}_{ij} \cdot \mathbf{m}_{ji}) \tag{1.66}$$

where I is the intensity of the electromagnetic field, n is the refractive index of the medium, and D_{ij}, G_{ij}, and R_{ij} are the electric dipole strength, magnetic dipole strength, and rotatory strength respectively.

The magnetic dipole strength is on the order of 10^{-4} relative to the electric dipole strength, so it is typically not included in further analysis [32]. In light of this, the dominant correction to (1.23) comes from the rotatory strength.

Similar to (1.25) where the dipole strength is proportional to an integral over $\varepsilon_{ij}(\nu)$, the rotatory strength is proportional to an integral over the difference between extinction coefficients.

$$\Delta\varepsilon_{ij} = (\varepsilon_{-})_{ij} - (\varepsilon_{+})_{ij} \tag{1.67}$$

$$R_{ij} \sim \int \frac{\Delta\varepsilon_{ij}}{\nu} d\nu \tag{1.68}$$

The shape of an instrinsic CD band is the same as the absorption band, but with a smaller amplitude [28].

1.2.7 Excitonic Circular Dichroism

As mentioned earlier, CD can arise from the structure of an individual molecule but also as a consequence of excitonic interactions. Even for molecules with intrinsic CD the excitonic CD can be much larger when the pigments are strongly interacting [24]. To examine excitonic CD we begin with (1.56) and assume that $kz \ll 1$.

$$\mathbf{E}_{R/L}(\mathbf{r}, t) = \frac{E_0}{\sqrt{2}}\left[\cos(\omega t)(\hat{\mathbf{x}} \pm kz\hat{\mathbf{y}}) \mp \sin(\omega t)(\hat{\mathbf{y}} \mp kz\hat{\mathbf{x}})\right] \tag{1.69}$$

The transition probability from the ground state A to excited state B_k is proportional to the square of the matrix element H'_{ij} shown in (1.70).

$$H'_{B_k,A} = \langle \Psi_{B_k} | -\boldsymbol{\mu} \cdot \mathbf{E} | \Psi_A \rangle \tag{1.70}$$

The transition probability is

$$P_{A \to B_k} \sim E_0^2 \left[\frac{(\hat{\mathbf{x}} \cdot \boldsymbol{\mu}_k)^2 + (\hat{\mathbf{y}} \cdot \boldsymbol{\mu}_k)^2}{2} \mp \frac{2\pi}{\lambda} \sum_n \sum_m c_{kn} c_{km}^* (\hat{\mathbf{z}} \cdot \mathbf{r}_n)(\hat{\mathbf{z}} \cdot \boldsymbol{\mu}_n \times \boldsymbol{\mu}_m) \right] \tag{1.71}$$

and has an interesting spatial dependence on the mutual orientations of pairs of molecules, but also the position of one of the molecules along the propagation direction of the electric field. This is the origin of the extra structural information that excitonic CD provides that is not found in excitonic absorption. The intuitive understanding of this spatial dependence is that since the polarization vector of the electric field traces out a spiral as it propagates, the polarization vector may align well with the transition dipole moment of one molecule and then align well with another molecule's transition dipole moment after propagating some distance [24].

We can rewrite the dipole strengths as in (1.72).

$$D_k^{R/L} = D_k \mp \frac{2\pi}{\lambda} \sum_n \sum_m c_{kn} c_{km}^* (\mathbf{r}_n \cdot \boldsymbol{\mu}_n \times \boldsymbol{\mu}_m) = D_k \pm R_k \tag{1.72}$$

From (1.72) we can extract an expression for rotational strength, shown in (1.73).

$$R_k \equiv \frac{D_k^L - D_k^R}{4} = \boldsymbol{\rho}_k \mathbf{R} \tag{1.73}$$

$$\rho_{ij,k} \equiv c_{kn} c_{km}^* \tag{1.74}$$

$$R_{ij} \equiv -\frac{\pi}{2\lambda} (\mathbf{r}_{ji} \cdot \boldsymbol{\mu}_j \times \boldsymbol{\mu}_i) \tag{1.75}$$

$$\mathbf{r}_{ij} \equiv \mathbf{r}_i - \mathbf{r}_j \tag{1.76}$$

From (1.72) one can see that the dipole strength D_k splits into D_k^R and D_k^L, where one band is stronger by R_k and one is weaker by R_k. The average of these two bands is the original dipole strength D_k.

1.3 Spectroscopic Methods

As shown in the previous sections, a perturbation in the form of an appropriate oscillating electric field such as produced by a laser can drive a transition between the states of a system. Therefore, optical techniques provide a method for directly probing the electronic structure of microscopic systems. Various optical spectroscopy techniques have been devised to investigate the frequency, polarization, and time dependence of optically accessible properties. In many cases the measurements are ensemble averages over all of the atoms, molecules, proteins, etc in the sample, but single molecule spectroscopic measurements are possible as well [33].

As mentioned previously, the FMO complex is a very well studied system. Various steady-state and time resolved spectroscopic techniques have been employed to examine the electronic structure of the FMO complex. The excitonic theory examined in the previous section predicts that there are 8 different electronic states, and thus 8 different peaks in the absorption spectrum of a single FMO complex. Vibrations of the surrounding protein and vibrations of the pigments themselves, both of which become stronger as temperature increases, serve to broaden the absorption spectrum. This means that much of the fine detail in the spectrum is lost at room temperature, as shown in Figure 1.6.

As mentioned in Section 1.2, a system's absorption describes its ground state interaction with light without regard for its polarization. A system's CD describes its ground state interactions with light that is circularly polarized. Fourier transform infrared spectroscopy (FTIR) is a spectroscopic technique that can be used to examine the vibrational spectrum of a system [28]. Instruments that perform these steady state measurements and other polarization sensitive measurements are readily available.

Time-resolved measurements are typically carried out with custom built instruments, though some commercial instruments are available. Light sources for these instruments are

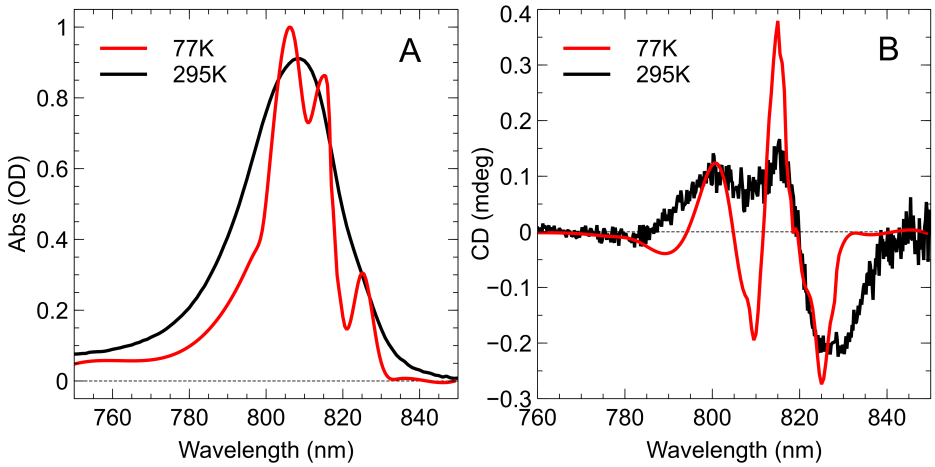

Figure 1.6. FMO WT absorption (A) and CD (B) at room temperature (black) and 77K (red).

often pulsed lasers (nanosecond to attosecond resolution), but flash lamps may also be used for measurements that do not require high time resolution [34]–[38].

Pump-probe is a common technique for measuring transient changes in absorption or CD [36]–[38], but other techniques exist such as two-dimensional electron spectroscopy (2DES) [34], [35], and photon-echo spectroscopy [39]. Only pump-probe will be described here as it is the technique used in the work presented here.

1.3.1 Pump-Probe Spectroscopy

The pump-probe technique typically employs two pulsed lasers, a "pump" beam and a "probe" beam, that are delayed relative to one another. The pump pulse serves to excite the sample, starting energy or electron transfer processes within the sample and causing a transient change in the absorption of the sample. The intensity of the probe pulse is modulated by the absorption of the sample, so the presence of the excitation causes a change in the intensity of the probe pulse [28]. The delay between the pump and probe pulses is varied to sample the kinetics of the energy or electron transfer processes. The probe pulse is typically broad (>10 nm FWHM), so a measurement may be collected at a single wavelength via filters or a measurement may be collected at all wavelengths within the probe bandwidth

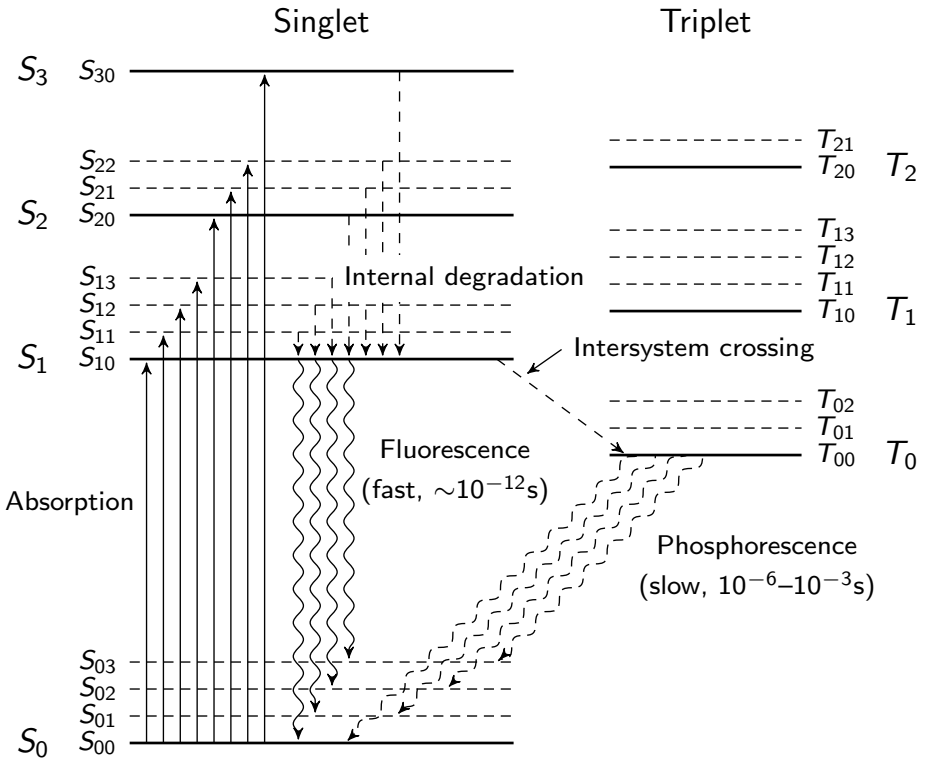

Figure 1.7. Jablonski diagram showing radiative and nonradiative transitions between electronic states and vibrational levels in a model system.

simultaneously by dispersing the probe pulse onto a CCD camera. Additional beams and pulses may be used to prepare a system in a specific state or to compensate for noise.

The work presented here has measured transitions between triplet states of the FMO complex. As described in Section 1.2.3, the transition probability between two states is highest when the frequency of the incident light matches the frequency of the transition. However, some transitions that meet this requirement nonetheless have a very low probability. These so-called *forbidden* transitions are those for which the spin of the system must change in the course of the transition [24], [28]. One such forbidden transition is the transition from a singlet ($S = 0$) ground state to a triplet ($S = 1$) excited state or vice versa. A variety of states and the transitions between them are shown in Figure 1.7.

A molecule in a singlet ground state S_0 excited to singlet excited state S_1 may either decay back to the ground state or undergo intersystem crossing (ISC) to decay to the triplet excited state T_1 [24], [28], [40], [41]. The $T_1 \rightarrow S_0$ transition is much slower than the

$S_1 \rightarrow S_0$ transition because the $T_1 \rightarrow S_0$ transition is forbidden. The analysis of triplet state dynamics has physiological relevance to the FMO complex as it has a high triplet yield but remains photostable without the photoprotection mechanisms found in other pigment-protein complexes [37]. It was found through pump-probe spectroscopy that the lowest triplet state energy in the FMO complex lies below that of singlet oxygen, preventing the formation of damaging radical oxygen [37]. Further examination of triplet state dynamics could be used to design photostable artificial photosynthetic systems.

The signals measured via pump-probe are a combination of several effects which may yield a positive or negative change in absorption at a given wavelength. An absorption band corresponding to a transition from the ground state is lost when a molecule is excited by the pump. This is effect is called photobleaching (PB) and its contribution is a negative change in the absorption. A new absorption band corresponding to a transition from this excited state to a higher state appears in place of this ground state band, and the excited molecule may absorb photons from the probe pulse to reach this higher state. This is called excited state absorption (ESA) and contributes a positive change to the absorption because there is additional absorption at the location of the new band. The excited molecule can undergo stimulated emission (SE) and release a photon, which appears to the detector as a photon that wasn't absorbed and thus contributes a negative change in the absorption [40], [41]. In the case of an excitonic system such as the FMO complex instead of measuring the evolution between electronic states of a single molecule the signals measured in a pump-probe experiment may measure the evolution between different excitonic states.

Analysis of pump-probe data involves decomposing a two-dimensional dataset of the form $\Delta\mathrm{A}(\lambda, t)$ into a set of decay-associated difference spectra $\Delta\mathrm{A}_i(\lambda)$ (DADS) and lifetimes τ_i that are associated with energy transfer or electron transfer processes started by the excitation from the pump pulse.

$$\Delta\mathrm{A}(\lambda, t) = \sum_i \Delta\mathrm{A}_i(\lambda) e^{-t/\tau_i}$$

This is typically accomplished with a global fitting procedure in which the DADS are free parameters at each measurement wavelength while the τ_i are fixed across the entire set of

measurements. Once the DADS have been extracted the analysis moves to assigning them to energy transfer or electron transfer processes. Spectral features in the DADS aid in assigning a DADS to a particular process. However, this is difficult when there is "spectral congestion" i.e. many pigments that absorb in the same region. In these scenarios measurement techniques such as CD spectroscopy that can differentiate between molecules that absorb at the same wavelength become particularly useful.

1.3.2 Time-Resolved Circular Dichroism Spectroscopy

In a typical pump-probe experiment the pump and probe beams are both linearly polarized lasers, but the measurement may not rely on the actual polarization of the beams. However, circular dichroism measurements by their nature rely on the polarization of one or both of the pump and probe beams. Time-resolved circular dichroism (TRCD) measurements fall into two categories: ellipsometric [42]–[45] and absorptive [46]–[51].

The absorptive method simply replaces a linearly polarized pump or probe beam with a circularly polarized one. The handedness of a circularly polarized pump may be switched back and forth to measure the preferential excitation of a sample in its ground state. The handedness of a circularly polarized probe may be switched back and forth to measure the change in CD induced by an excitation. Until recently this method has required prohibitively high sensitivity to measure small signals since CD is on the order of 10^{-3} relative to absorption.

The ellipsometric method prepares the probe beam in a highly elliptically polarized state (which is a superposition of both RCP and LCP light) and relies on the CD of the sample to vary the minor axis of the polarization ellipse. This method was recently advanced to enable measurement of extremely small signals and is used to collect the measurements presented in this work [41]. The apparatus used in this work will be described in detail in Chapter 3 and progress on a shot-noise limited femtosecond CD spectrometer will be described in Chapter 4.

1.3.3 Triplet-Triplet Energy Transfer

The time-resolved spectra collected using the methods described in the previous sections reveal information about the rates at which energy moves through a pigment-protein complex, namely the couplings between pigments and their relative populations. Pigment-pigment couplings are required for the formation of excitonic states, as described in 1.2.4, and allow for a variety of energy transfer mechanisms between individual pigments [28].

Resonant energy transfer occurs when there is a resonance between a downward transition in the donor pigment and an upward transition in the acceptor pigment, or, in other words, when the donor and acceptor absorption spectra overlap [28]. The rate of resonant energy transfer is proportional to the square of the electronic coupling between pigments, and Equation 1.46 illustrates that the dipole-dipole Coulomb interaction is proportional to R_{ij}^{-3}. Thus, the rate of resonant energy transfer is proportional to R_{ij}^{-6}, making resonant energy transfer strongly dependent on the distance between the donor and acceptor pigments. However, resonant energy transfer only occurs when the ground state and excited state have the same spin (i.e. the transition is not "forbidden") [28]. Most pigments have singlet ground states, meaning that a transition from a triplet excited state to a singlet ground state is forbidden.

Once pigments are close enough contributions from other coupling mechanisms become significant, namely the "exchange" interaction. Equation 1.77 illustrates the form of the exchange interaction between two pigments, each with energy levels a and b, where (0) and (1) refer to the coordinates of electron 0 or 1 respectively and $\sigma_0^{(a)}$ refers to the spin of pigment 0 in state a [28].

$$H_{10}^{\text{Exch}} = -\langle \varphi_0^{(a)}(1)\varphi_1^{(b)}(0)|\frac{e^2}{r_{10}}|\varphi_0^{(b)}(0)\varphi_1^{(a)}(1)\rangle \langle \sigma_1^{(b)}|\sigma_0^{(b)}\rangle \langle \sigma_0^{(a)}|\sigma_1^{(a)}\rangle \tag{1.77}$$

The first term is an overlap integral which is only non-negligible when the two pigments are close enough for their orbitals to overlap. This term also describes the excited electron on the donor pigment being transferred to the acceptor pigment while the ground state electron on the acceptor pigment is transferred to the donor pigment, as shown in Figure 1.8.

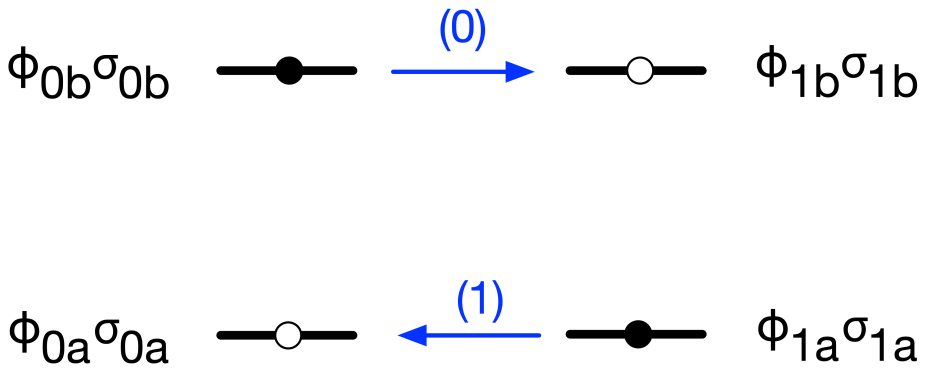

Figure 1.8. Illustration of the exchange interaction between a donor and acceptor pigment. The excited electron on the donor and acceptor pigments exchange electrons without the electrons changing their spins. The (0) and (1) refer to the fact that the electron on pigment 0 and 1 respectively are transferred from one pigment to another.

This exact form of the overlap term depends on the shape of the orbitals, but is generally taken to have the form $e^{-R_{edge}/L}$ where R_{edge} is the edge-to-edge distance between the pigments and L is on the order of 1Å [28]. This is a much stronger spatial dependence than R_{ij}^{-6} and explains why the exchange interaction is only significant for pigments that are very close to one another. The second and third terms are non-zero only when the spins of the upper states on each pigment are the same and the spins on the lower states on each pigment are the same.

The exchange interaction therefore allows the transfer of a triplet excited state between pigments, as the spin of the excited electron does not need to change in order for the excitation to move between pigments. This is also referred to as Dexter energy transfer [28].

1.4 Computational Methods

As mentioned previously, spectral congestion and a large number of pigments make experimental measurements of pigment-protein complexes difficult. In Photosystem I there are 96 Chl *a* pigments, so assigning DADS spectra to any particular population is not straightforward. Furthermore, in pigment-protein complexes where the pigments are strongly interacting such as FMO it is impossible to directly measure individual pigments due to the mixing of individual pigment states into excitonic states. In the case of the FMO complex identifying the pigment energies of even just 8 pigments has proven difficult [24]. One of the original difficulties in modeling FMO was realizing that each of the 8 pigments have different energies despite being otherwise identical molecules [24].

Predicting the interactions of each pigment with the others as well as the protein environment is one focus of computational modeling efforts [20], [24], [52]–[54]. A number of Hamiltonians have been proposed based on modeling and fits of experimental data [55]–[57]. Further improvements have been made by adjusting the line shapes of interactions between excitonic states and the bath of vibrations in the surrounding protein [58].

Recent efforts have focused on simulating the FMO protein from first principles using molecular dynamics (MD) simulations and quantum mechanical refinements [20]. This avenue of investigation is attractive because the only input is the X-ray crystal structure of

the protein. In pure MD simulations Newton's equations of motion are iteratively integrated for all atoms in the system, computing the trajectory of each atom in the system [59]. Approximations are employed to cull the number of interactions necessary to compute the next time step as the computational complexity grows rapidly with the number of atoms in the system [59]. For example, electrons are typically not explicitly included in computations, instead empirical force fields are used to account for the interactions between atoms and their environments [59]. Software packages such as GROMACS, LAMMPS, and NAMD exist and have been developed to run on massively parallel computing clusters as well as GPUs [59].

2. STEADY STATE MODELING OF FMO

2.1 Introduction

As mentioned in previous sections, the pigment-protein complexes involved in photosynthesis are extraordinarily efficient at transferring energy over long distances. This efficiency is due in part to the protein environment tuning the positions and electronic properties of the pigments in the complex. Experimental data provides substantial insight into the details of energy transfer in these proteins, but large, complex systems present experimental difficulties that preclude useful measurements. Systems with many pigments or excitonic states with overlapping absorption make distinguishing just a few interesting pigments nearly impossible. Chemical modification of these systems to allow easier measurement of the pigments of interest can move the system further from physiological conditions to the point of questionable relevance.

Computational modeling provides a complement to experimental measurements in cases where a protein structure and/or Hamiltonian is known. However, computational cost quickly outpaces available computational resources due to the number of electrons in a typical protein. Careful choice of computational methods and approximations enables modeling of moderately sized systems.

In the case of WT FMO, several Hamiltonians have been proposed based on structural data and fits to experimental data [55]–[57]. The off-diagonal elements of the Hamiltonians represent the electronic couplings between pigments and can be approximated via dipole-dipole interactions and X-ray structures. The diagonal elements are the site energies of the pigments and are influenced considerably by the protein environment. To date these diagonal elements have been computed from fits to experimental data with varying degrees of success.

In order to observe the influence of the amino acid residues that coordinate each pigment, Saer et al. [60] prepared 8 site-directed FMO mutants (one for each pigment) and measured their absorption and CD spectra. The amino acids targeted in [60] were chosen from amino acids that were close to oxygen atoms in the chlorin rings of the nearby BChl *a* pigments, and the mutations were intended to replace polar residues with non-polar residues or non-polar residues with polar residues while still allowing the system to grow photosynthetically.

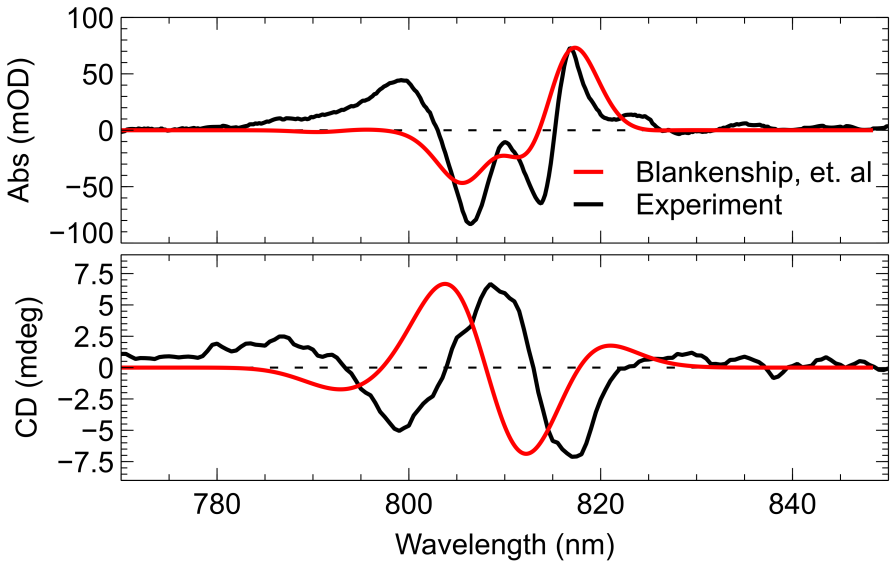

Figure 2.1. Comparison of modeled and measured M7 absorption (77 K) and CD (295 K). The modeled data is obtained by increasing the energy of pigment 7 in the Kell Hamiltonian by 24 cm^{-1} as in [60]. While the computed absorption provides a good match, the computed CD is shifted enough that the experimental and modeled CD have opposite signs.

The authors attempted to model the effect of each mutation by modifying empirical WT Hamiltonians, shifting the site energy of the pigment nearest each mutation.

There was qualitative agreement between the proposed Hamiltonians and the experimental mutant spectra except in the case of pigment 7 (mutant Q198V), shown in Fig. 2.1.

It was proposed that the spectral changes in Q198V could not be explained by a simple shift of pigment 7's site energy and that the spectral changes could instead be attributed to wide-spread structural changes induced by the mutation.

To investigate the cause of the spectral changes in the mutants we have applied a previously reported computational method that can reproduce the electronic properties of WT FMO from first principles based only on available X-ray protein structures. The work presented here will focus primarily on mutants Y16F (pigment 3) and Q198V (pigment 7). The Y16F mutant is of interest because pigment 3 has the lowest energy in FMO and contributes primarily to the easily visible 825 nm band. The Q198V mutant is chosen for investigation precisely because the modeling in [60] could not explain the experimental spectra.

2.2 Computational Methods

Hamiltonians were obtained from first-principles modeling by Prof. Lyudmila Slipchenko and Yongbin Kim using the methods described in [20]. In short, molecular dynamics (MD) simulations are performed on the X-ray structure of the FMO trimer with a time step of 2 fs for a total duration of 80 ns. 100 snapshots are chosen at random from the last 30 ns of the MD simulations, motivated by the assumption that the protein has reached an equilibrium conformation by this time. Quantum-mechanics/molecular-mechanics (QM/MM) geometry optimizations are performed on each pigment and a few surrounding amino acids for each snapshot. Excited state calculations are performed with an effective fragment potential (EFP) model. The optimizations have a significant impact on the site energies of the pigments as described in [20].

The distribution of pigment energies for WT are shown in Figure 2.2, while Figures 2.3 and 2.4 compare the distribution of pigment energies in M3 and M7 respectively to WT.

X-ray structures for the mutants are not yet available, so the mutant structures were created by replacing the appropriate amino acid in the WT structure and minimizing the structure with MD simulations. The subsequent computational steps were otherwise identical to those for WT FMO.

The simulations from which the Hamiltonians were obtained were performed by Yongbin Kim, so the first-principles Hamiltonians will be referred to as "YB Hamiltonians" from here on out. Once the Hamiltonian, pigment positions, and pigment transition dipole moments are extracted from a snapshot, the absorption and CD spectra are computed for each snapshot. As mentioned in Section 1.2, the excitonic states are obtained by diagonalizing the Hamiltonian matrix H_{ij}. The excitonic energies E_i are the eigenvalues of H_{ij} and the eigenvectors c_{ij} represent the contributions of site j to exciton i. The dipole strength and rotational strength for each exciton are computed with Eq. (1.52) and Eq. (1.73) respectively.

Each transition is modeled with a Gaussian band shape located at E_i. The bandwidth depends on the Hamiltonian being modeled and the temperature at which to model. The structures in the simulations were modeled at room temperature (RT), so some broadening is

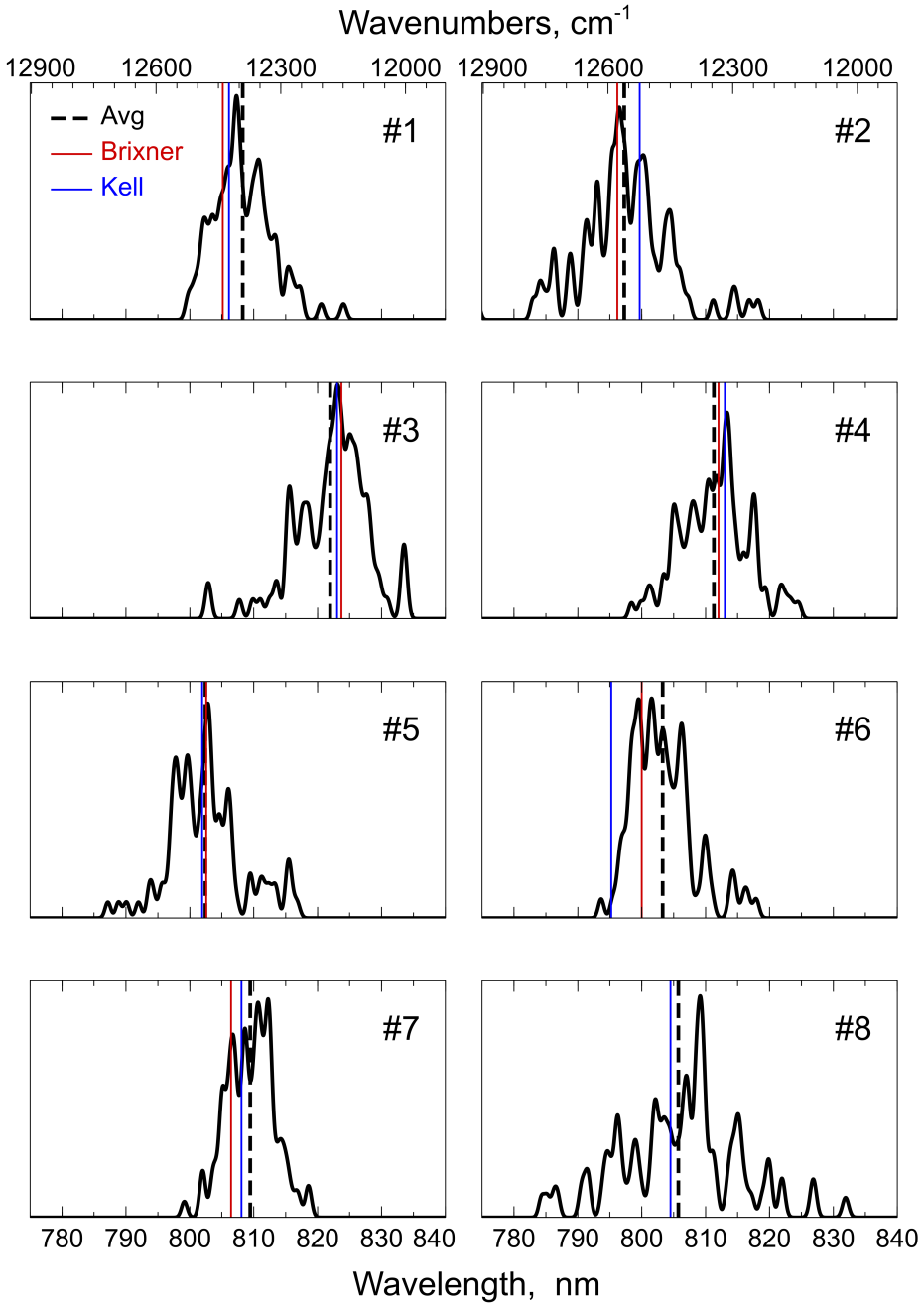

Figure 2.2. Distribution of pigment energies for WT FMO modeled from first principles (black, solid). The average energy (black, dashed), and pigment energies from the Brixner (red) and Kell (blue) empirical Hamiltonians are labeled for comparison.

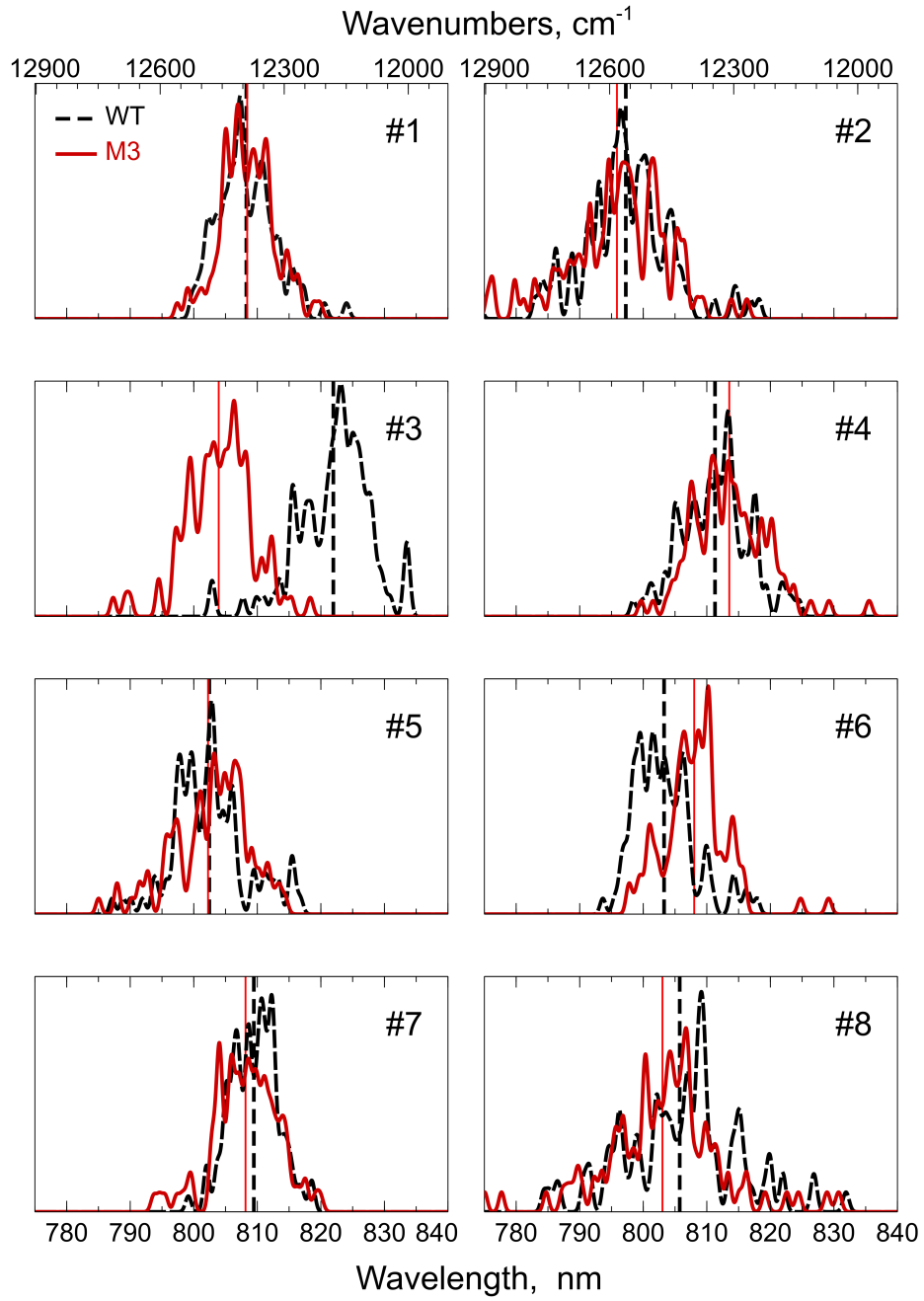

Figure 2.3. Distribution of pigment energies for M3 FMO (red, solid) compared with the distribution of pigment energies for WT FMO (black, dashed). Note the significant shifts in pigments 3 and (to a lesser degree) pigment 6.

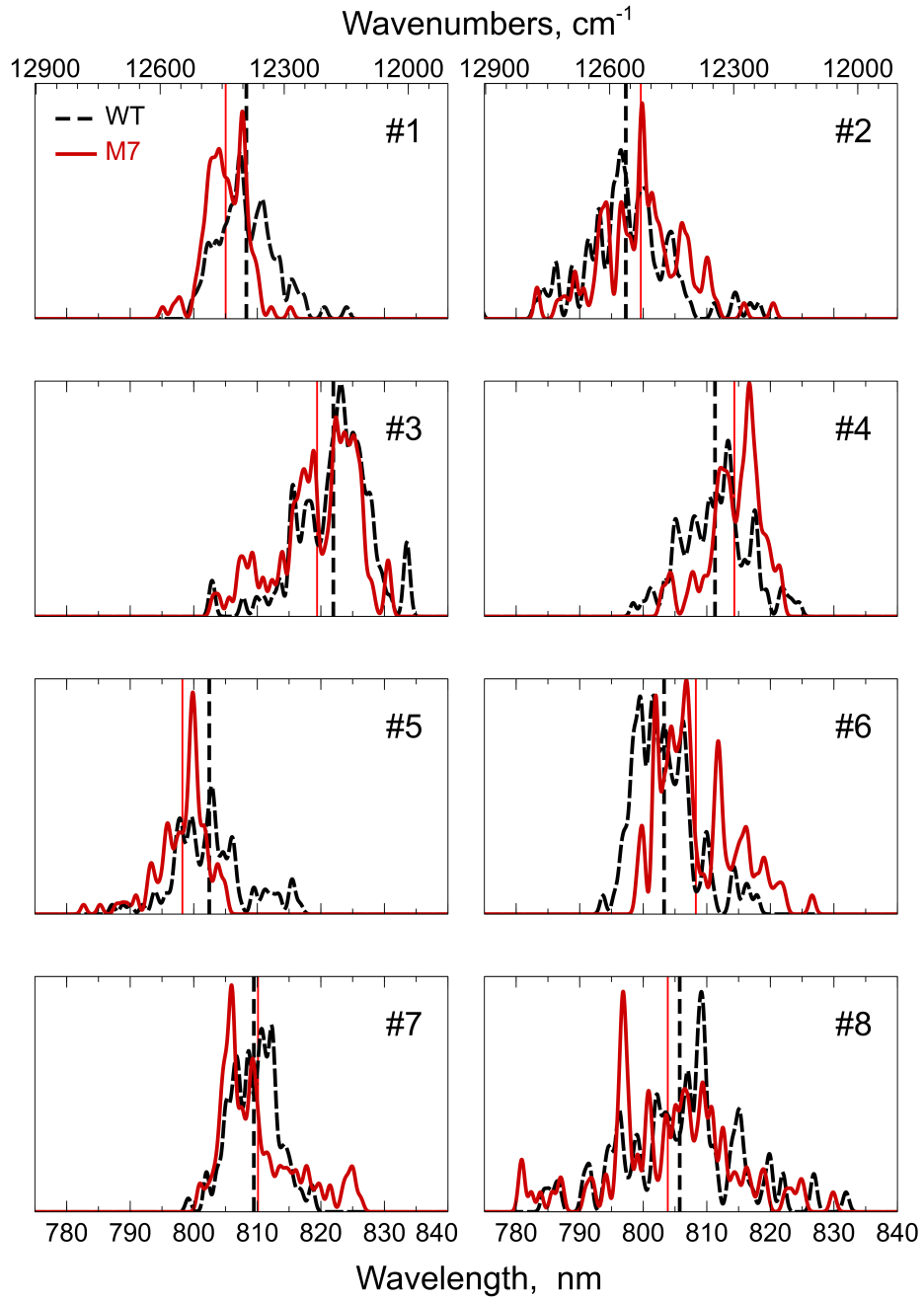

Figure 2.4. Distribution of pigment energies for M7 FMO (red, solid) compared with the distribution of pigment energies for WT FMO (black, dashed). The shifts relative to WT are minor.

already applied by the motion of the protein. In order to model low-temperature spectra, the YB Hamiltonians were "squeezed," meaning that the difference in diagonal energies between each snapshot and the average Hamiltonian was reduced by half. The bandwidths for each Hamiltonian at both RT and 77 K are shown in Table 2.1. These bandwidths were chosen to visually match experimental spectra at the respective temperatures.

Table 2.1. Bandwidths used to compute steady state spectra.

Hamiltonian	**77 K BW (cm^{-1})**	**RT BW (cm^{-1})**
YB (100)	70	140
Brixner	105	157.5
Kell	105	157.5

Structures were only available for WT, Y16F (mutant 3, M3), and Q198V (mutant 7, M7), so analysis will focus solely on these proteins. The spectra are computed as a mix of 45% 7-pigment and 55% 8-pigment spectra as the 8th pigment may be lost during sample preparation [61].

2.3 Results

The average YB WT Hamiltonian is shown in Table 2.2, and the deviations of the mutants from the WT Hamiltonian are shown in Tables 2.3 and 2.3. The spectra obtained from the YB Hamiltonian are in excellent agreement with 77 K experimental spectra, shown in Figure 2.5. The main difference between the modeled spectra and the experimental spectra is in the blue region below 800 nm. This difference can be attributed to the higher-energy sites having broader bandwidths and shorter lifetimes, which are effects that are more complex to model and are out of the scope of this work.

Experimental absorption spectra for the mutants were collected at 77 K and CD spectra were collected at RT. The modeled spectra presented here are modeled at the same temperatures as the experimental spectra.

Figure 2.6 shows the full set of absorption and CD spectra produced by averaging the spectra computed from each of the 100 YB Hamiltonians. The spectra are in good qualitative agreement with the experimental absorption and CD spectra.

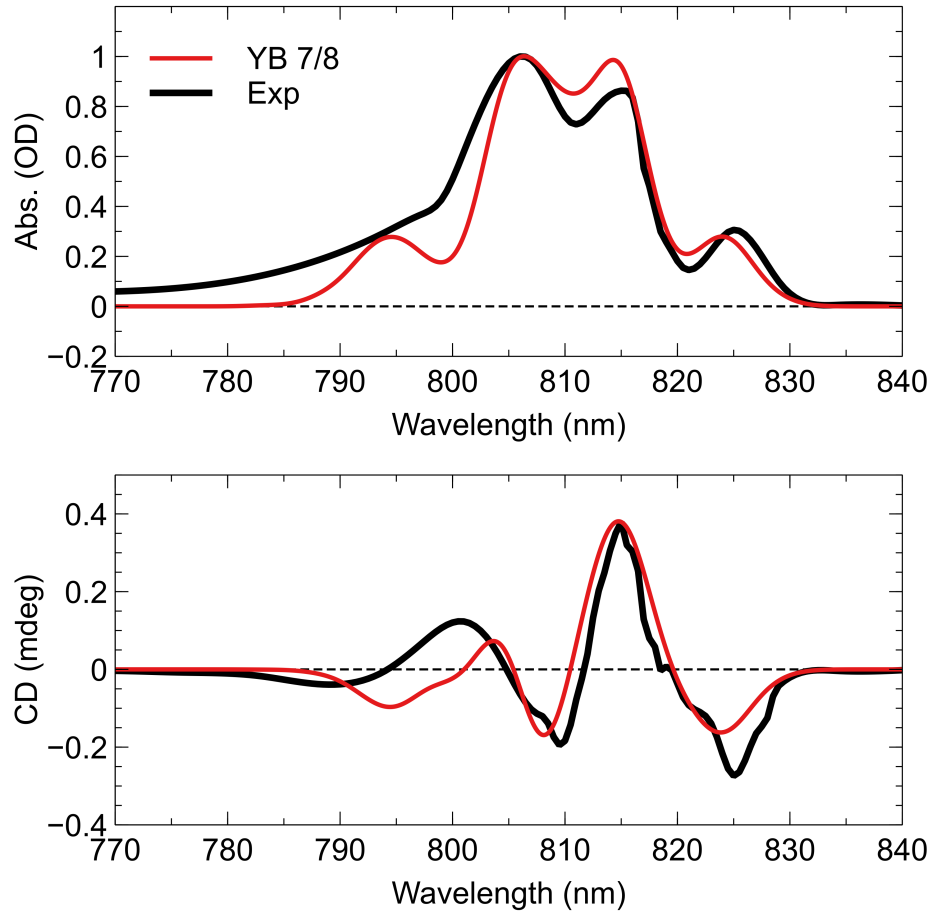

Figure 2.5. Comparison of experimental and modeled WT spectra at 77 K. The "YB 7/8" spectrum is a mix of 45% 7-pigment and 55% 8-pigment WT spectra. Pigment 8 may be lost during purification, so a more realistic model of the absorption spectrum includes a mix of both 7- and 8-pigment spectra. The occupancy of the pigment 8 site was found to be 55% via electrospray mass-spectrometry [61].

Figure 2.7 shows the "Mutant−WT" difference spectra computed from the YB Hamiltonians along with spectra computed from modified empirical Hamiltonians. The WT Brixner and Kell empirical Hamiltonians are shown in Tables 2.5 and 2.6 respectively. The empiricial mutant Hamiltonians are constructed by applying the diagonal shifts from Tables 2.3 and 2.4 to the Brixner and Kell Hamiltonians. It was found that the shifts from off-diagonal elements made little difference to the spectrum.

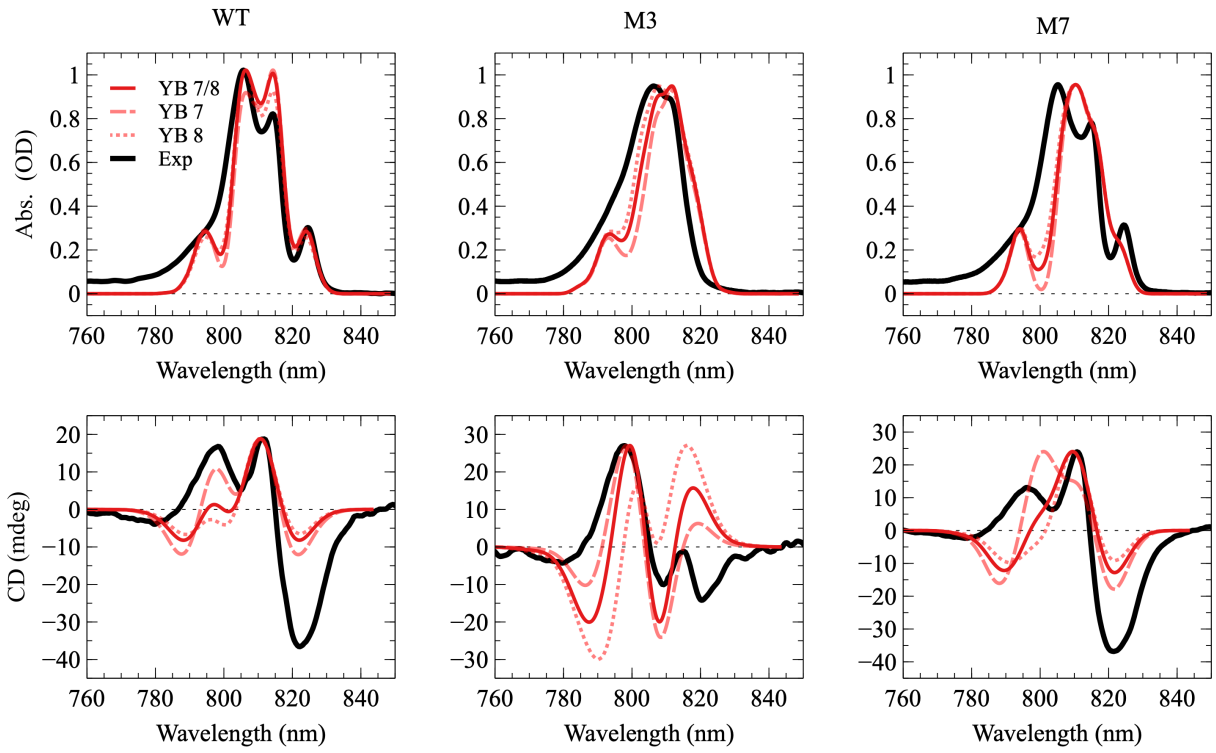

Figure 2.6. Steady state spectra of FMO WT, M3, and M7 computed from first principles with 100 Hamiltonians. The computed CD spectra are blue-shifted by 5 nm for visual comparison.

Table 2.2. Average of 100 WT Hamiltonians with diagonals shifted by $-2420\,\mathrm{cm}^{-1}$ to match experimental absorption spectrum. Elements are given in wavenumbers (cm^{-1}).

12373	-109.5	5.2	-6.4	6.5	-9.2	-2.6	22.5
-109.5	12544	36.9	9.4	1.6	11.9	6.7	5.7
5.2	36.9	12166	-50.1	-1.8	-10.2	6.7	1.4
-6.4	9.4	-50.1	12326	-82.6	-19.1	-54.1	-2.0
6.5	1.6	-1.8	-82.6	12463	54.1	4.2	4.4
-9.2	11.9	-10.2	-19.1	54.1	12450	28.6	-11.6
-2.6	6.7	6.7	-54.1	4.2	28.6	12354	-14.0
22.5	5.7	1.4	-2.0	4.4	-11.6	-14.0	12412

Table 2.3. Deviations of Mutant 3 Hamiltonians from average WT Hamiltonian. Elements are given in wavenumbers (cm^{-1}).

-2.3±9.5	-7.7	1.1	-1.3	1.9	-4.9	-4.1	13.1
-7.7	21.9±17	-0.1	-0.6	-0.4	0.9	2.3	3.6
1.1	-0.1	272.5±12	5.4	0.7	-0.6	9.8	0.7
-1.3	-0.6	5.4	-34.2±12	-5.9	-0.6	-8.6	0.2
1.9	-0.4	0.7	-5.9	2.7±14	10.7	-1.4	0.1
-4.9	0.9	-0.6	-0.6	10.7	-73.6±11	2.4	2.6
-4.1	2.3	9.8	-8.6	-1.4	2.4	20.3±10	1.2
13.1	3.6	0.7	0.2	0.1	2.6	1.2	41.9±20

Calculating the absorption and CD spectra from a Hamiltonian requires also knowing the pigment positions and transition dipole moments. Therefore when computing the spectra of the average Hamiltonian the average pigment positions and transition dipole moments are also necessary. The protein can both rotate and translate during MD simulations so it is necessary to align the structures before averaging. Efficient algorithms such as the Kabsch algorithm exist for alignment and do a good job as shown in Figure 2.8.

2.3.1 Discussion

The aim of this work is to show that first-principles modeling is able to accurately reproduce electronic properties of pigment-protein complexes. To demonstrate this we have computationally constructed FMO mutants and conducted simulations from which we have

Table 2.4. Deviations of Mutant 7 Hamiltonians from average WT Hamiltonian. Elements are given in wavenumbers (cm^{-1}).

49.4±9	-22.2	1.3	-0.8	1.0	-1.2	-1.1	4.6
-22.2	-37.3±15	1.0	-1.7	0.5	0.7	3.3	3.2
1.3	1.0	38.2±13	-8.2	0.9	-0.5	4.5	0.7
-0.8	-1.7	-8.2	-46.2±10	-5.4	-1.3	-7.9	-0.3
1.0	0.5	0.9	-5.4	65.5±11	11.0	-0.7	0.4
-1.2	0.7	-0.5	-1.3	11.0	-77.6±12	8.1	-0.3
-1.1	3.3	4.5	-7.9	-0.7	8.1	-9.4±11	-0.8
4.6	3.2	0.7	-0.3	0.4	-0.3	-0.8	29.3±21

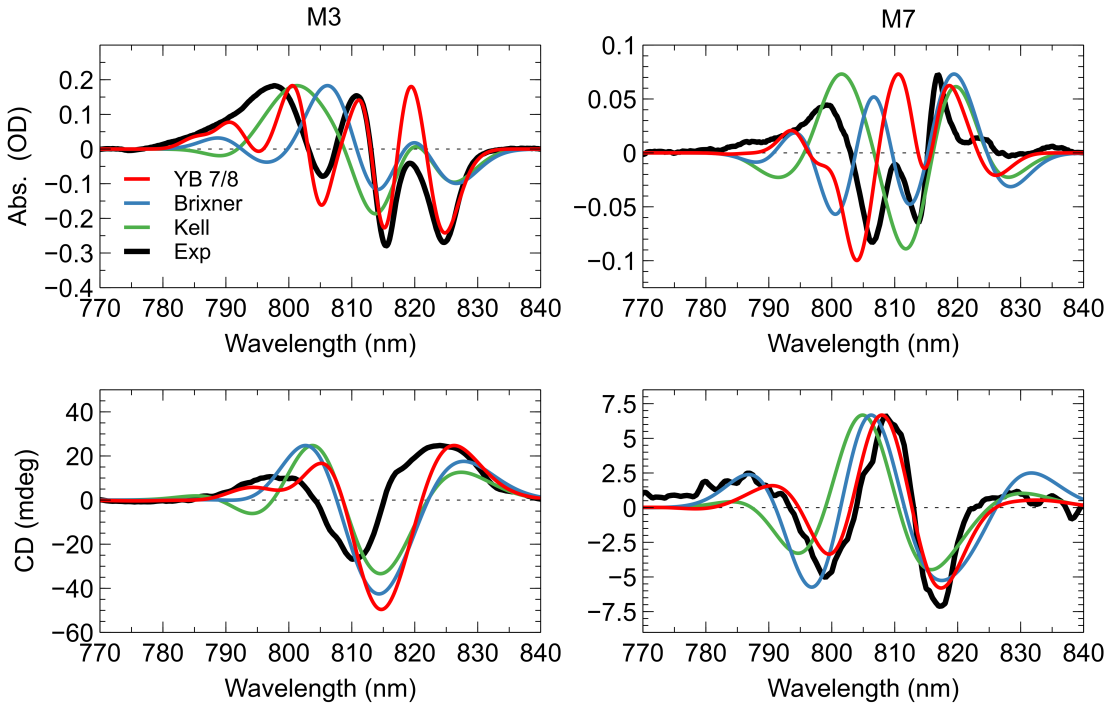

Figure 2.7. Mutant−WT difference spectra computed from first principles with 100 Hamiltonians. Also shown are difference spectra computed by applying diagonal shifts from Tables 2.3 and 2.4 to the Brixner and Kell Hamiltonians.

computed absorption and CD spectra. We have compared these modeled spectra against experimental mutant spectra and found them to be largely in agreement. In the discussion that follows we will compare against previous attempts to model mutant spectra and propose explanations for the spectral changes based on the first principles modeling efforts.

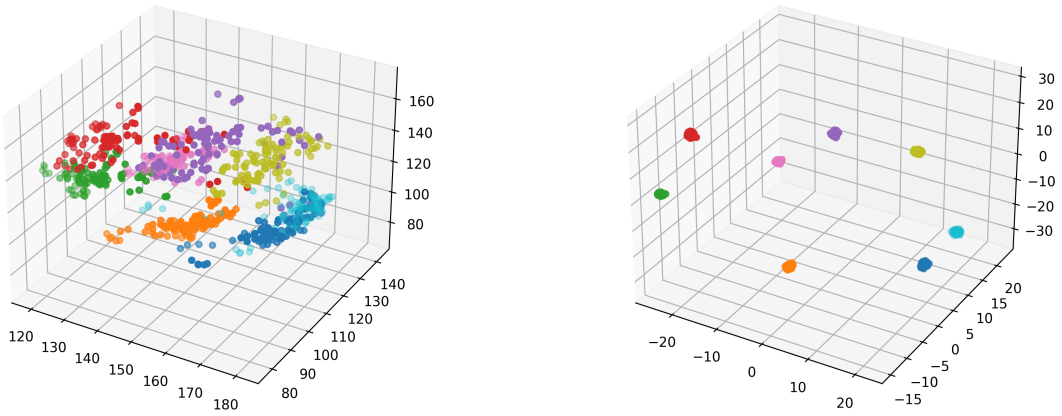

(a) Unaligned structures

(b) Aligned structures

Figure 2.8. Pigment positions from MD simulations before and after alignment. Pigments in a given color are the same pigment from different structures i.e. all red circles are pigment 1 from different structures.

Table 2.5. The Brixner Hamiltonian for FMO WT [56]. Note that the Brixner Hamiltonian only includes 7 pigments whereas the Kell and YB Hamiltonians include 8.

12420	-106	8	-5	6	-8	-4
-106	12560	28	6	2	13	1
8	28	12140	-62	-1	-9	17
-5	6	-62	12315	-70	-19	-57
6	2	-1	-70	12460	40	-2
-8	13	-9	-19	40	12500	32
-4	1	17	-57	-2	32	12400

Table 2.6. The Kell Hamiltonian for FMO WT [57].

12405	-87	4.2	-5.2	5.5	-14	-6.1	21
-87	12505	28	6.9	1.5	8.7	4.5	4.2
4.2	28	12150	-54	-0.2	-7.6	1.2	0.6
-5.2	6.9	-54	12300	-62	-16	-51	-1.3
5.5	1.5	-0.2	-62	12470	60	1.7	3.3
-14	8.7	-7.6	-16	60	12575	29	-7.9
-6.1	4.5	1.2	-51	1.7	29	12375	-9.3
21	4.2	0.6	-1.3	3.3	-7.9	-9.3	12430

It's interesting to note that averaging the spectra does not produce the same result as computing the spectrum of the average Hamiltonian even though analysis showed that there is no correlation in the differences between snapshots and thus the structural differences should be totally random. Figure 2.9 illustrates how different the spectrum of a single snapshot is both to other snapshots and the averaged spectrum. The average of the spectra agrees with experimental spectra better than the spectrum of the average Hamiltonian.

The mutant spectra computed from single-site shifts (Figure 2.10) generally do not reproduce experimental spectra as well as the first principles spectra, but a single-site shift reproduces M3 better than M7. This can be explained by examining the diagonal shifts in Tables 2.3 and 2.4. The largest average shift in the M3 Hamiltonian is a 272 cm^{-1} shift to pigment 3, where all other shifts are on the order of 20–30 cm^{-1}. In constrast with M3, the average shift to pigment 7 in the M7 Hamiltonian is -9 cm^{-1}, which is the smallest diagonal shift in the M7 Hamiltonian and is 30x smaller than the M3 shift to pigment 3. Further note

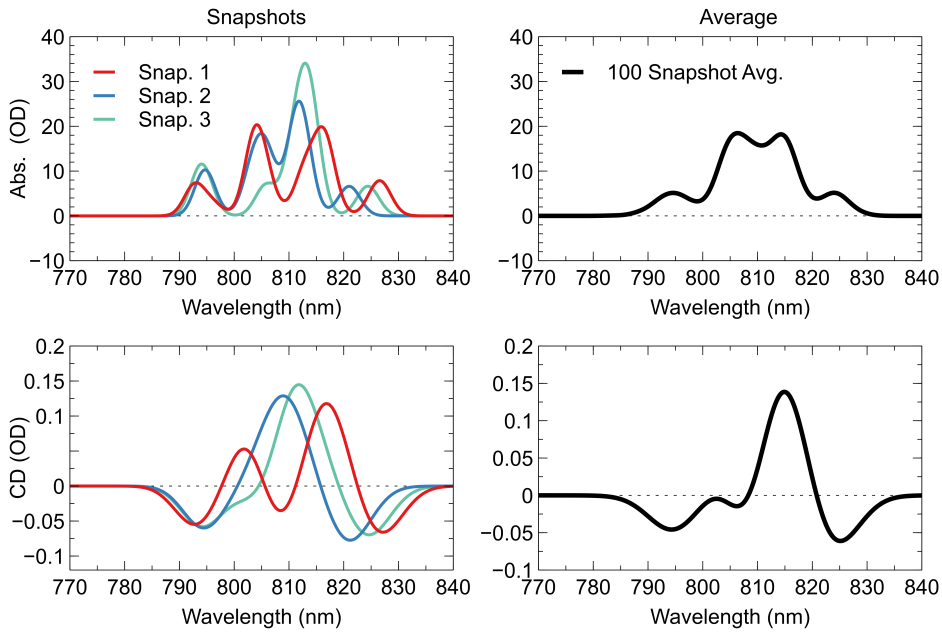

Figure 2.9. Spectra of 3 arbitrarily chosen snapshots from FMO WT compared to the average of 100 snapshot spectra. Individual spectra vary dramatically compared to the average.

that the diagonal shifts of the other pigments in M7 are still ∼3x smaller than the pigment 3 shift in M3, and thus are more comparable to the uncertainties of the diagonal energies. We can safely conclude that the effect of the mutation in M7 has no effect on pigment 7 in particular.

In this context it makes sense that the M7 spectrum would not be reproduced well by applying a single shift of the pigment 7 site energy to the WT Hamiltonian. This suggests that a mutation in the pocket of pigment 7 produces far-reaching effects felt by the other pigments in the monomer rather than a strong effect localized near pigment 7.

To determine the origin of the spectral changes introduced by each mutation Prof. Lyudmila Slipchenko and Jack Lawrence investigated mutant structural changes relative to WT. It is interesting to note that while the mutations introduce noticeable structural changes throughout the protein and most importantly near the pigments, only a fraction lead to noticeable energetic or spectral changes. Detailed analysis of the structural changes is outside the scope of this work, but I will summarize the most significant changes for each mutation. It is important to note that the amino acid residue numbers presented here are +8 higher

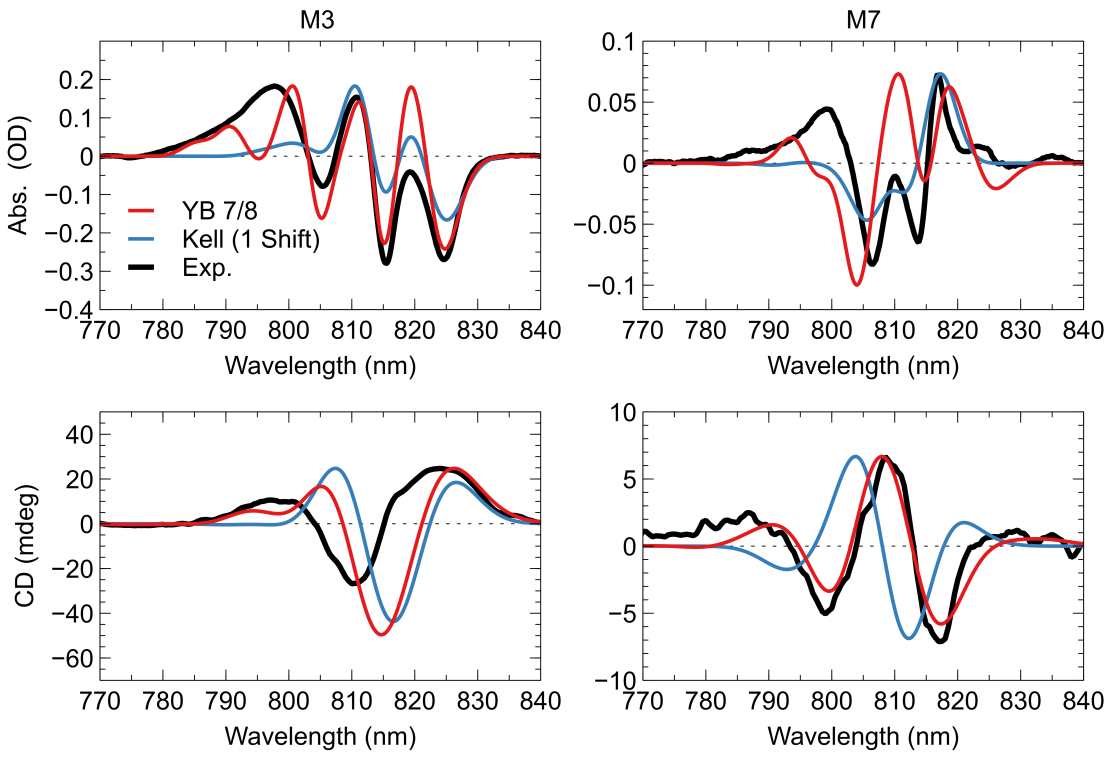

Figure 2.10. Mutant−WT difference spectra computed from the average of 100 first-principles spectra compared to a spectrum produced by shifting the site energy of a single pigment. The first-principles spectra (YB 7/8) are computed from a mix of 7- and 8-pigment spectra, while the single-site spectra are computed from the 8-pigment Kell Hamiltonian.

than the numbering in the protein database (PDB ID: 3ENI) for consistency with previous work in [60].

It was found that the largest structural changes are found in the flexible regions of the protein, whereas the more structured regions of the protein were less affected by individual mutations. For example, one of the largest effects in M3 is a distortion of a flexible region near pigment 2 shifting residues PRO 867 and ASN 868 by ∼2Å relative to pigment 2, as shown in Figure 2.11B. This distortion closes a pathway that lets water molecules near pigment 2 in WT such that no water is found coordinating the central Mg of pigment in M3. This large structural change results in a relatively minor energetic change to pigment 2 with a cumulative shift of $20 \pm 10.\,\mathrm{cm}^{-1}$ In the same vein, amino acids (LYS 239, SER

237, PRO 243) in a flexible region near pigment 5 see significant structural changes with no major change to the energy of pigment 5.

One would expect significant changes in the positions of multiple charged/polar amino acids near a pigment to produce a significant change in the electric field at the location of pigment and therefore cause a Stark shift to the pigment's transition energy. However, this is not what is observed for pigments 2 and 5. The electric field due to these amino acid residues could be screened by nearby water molecules or by opposing structural changes in other amino acids that move in concert with the residues near the pigment.

The largest effect of the M3 mutation is the energetic shift of the pigment 3 site energy by $272\,\mathrm{cm}^{-1}$. Interestingly, the structural changes near pigment 3 are small compared to the structural changes near pigments 2 and 5. The changes near pigment 3 are mainly located at turns of the peptide chain (e.g., ALA 30, ASN 298) and the structural changes here relative to WT are comparable to the fluctuations in the protein itself. Pigment 3 and the nearby shifted residues are shown in Figure 2.11C.

The large energetic change to pigment 3 is attributed to breaking the hydrogen bond (H-bond) to the pigment's carbonyl group as a result of the mutation replacing tyrosine with phenylalanine. The electron density on the carbonyl group is higher and therefore more negative in the excited state, and some of this extra electron density is donated to the H-bond with the nearby tyrosine leading to a red-shift of the excited state. With the mutation there is no H-bond, and thus the excited state on pigment 3 is blue-shifted relative to WT.

The mutation near pigment 7 in M7 does not significantly change the energy of the pigment as neither the glutamine nor the valine that replaces it in the mutant form an H-bond with the pigment. However, the mutation is in the middle of the protein and thus causes small structural changes throughout the protein that induce small shifts to the energies of all pigments. This makes modeling challenging as energetic changes cannot be assigned to a single dominating effect. Indeed, modeling shows that the changes are instead due to a collection of small effects that oppose each other to varying degrees. Regardless of the trouble determining the precise origin of spectral changes in the M7 mutant, the steady state spectra computed from the structures agree well with the experimental spectra.

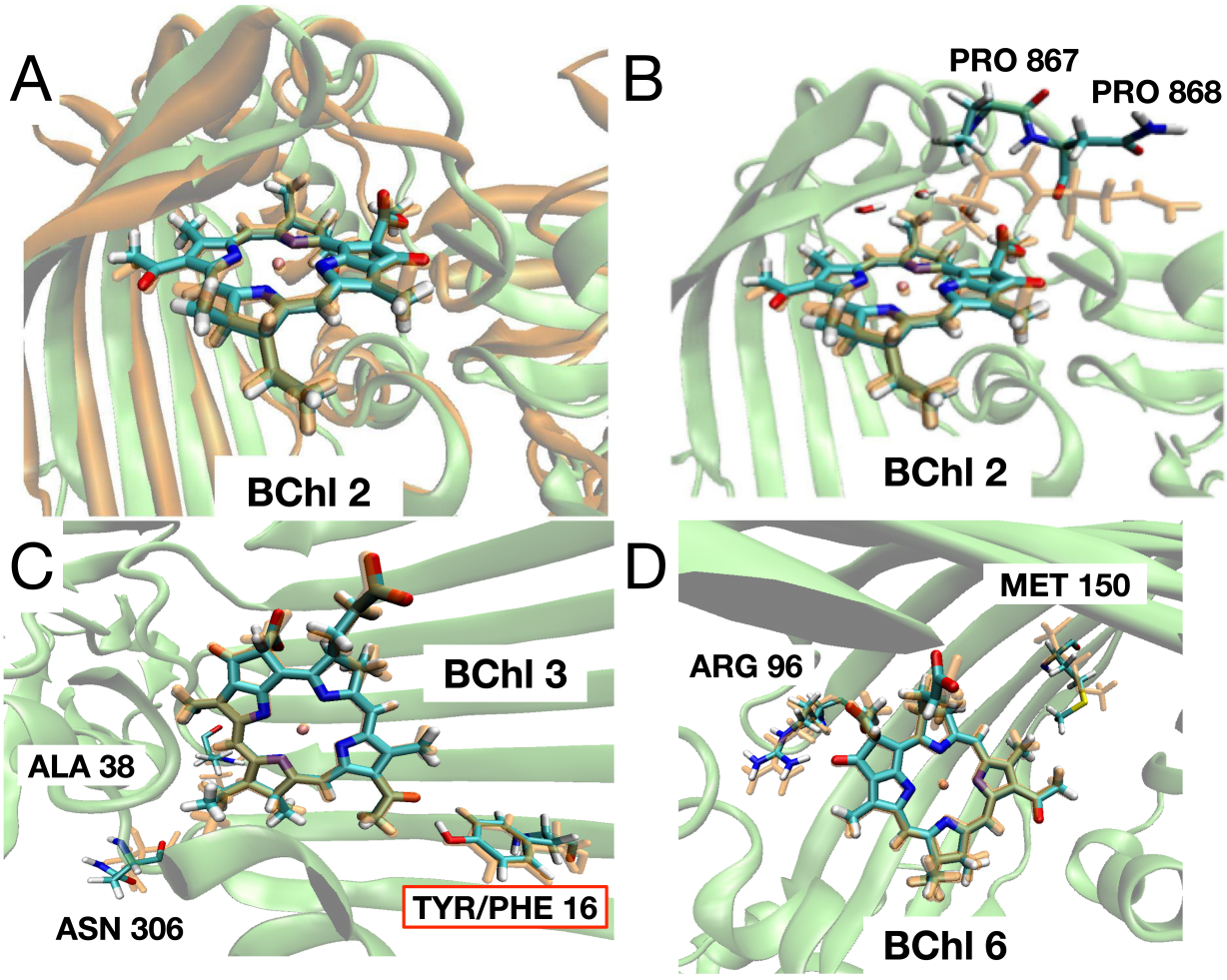

Figure 2.11. Structure of pigment pockets in M3 (solid) compared to WT (transparent). The structures were aligned by minimizing RMS error of the tetrapyrrole rings. The large structural changes near pigment 2 (A, B) produce minor spectral changes, whereas the small structural changes near pigment 3 (C, mutation outlined in red) and 6 (D) produce noticeable spectral differences.

As with M3 the largest structural change is in a flexible region of the protein near pigment 2. In a significant departure from M3, the water channel near pigment 2 remains open in M7 despite the structural changes. Another significant difference is that the relative orientation of pigments 1 and 2 are changed by ∼1Å, as shown in Figure 2.12A. The change in orientation causes a change of -22 cm^{-1} in the electronic coupling between the pigments. Similar to M3 the energy of pigment 6 is shifted by -77 cm^{-1} due to a combination of structural changes in the nearby ARG 96 (Figure 2.12B, not shown).

Based on this analysis we propose that the site energies of the pigments in FMO are determined predominantly by the Stark shifts due to the electric fields of nearby residues. Changes in residue positions produce changes in the net electric field at the location of the pigment and thus produce changes in the site energy of the pigment. The net effect may be the result of many residues with competing effects.

2.3.2 Conclusion

In this work I computed steady state absorption and CD spectra of WT, Y16F (M3), and Q198V (M7) FMO from 100 Hamiltonians each which were obtained from first principles modeling of the FMO protein at room temperature. I compared the modeled steady state spectra to experimental spectra and found them to be in good agreement. I then compared the "Mutant–WT" modeled difference spectra to the experimental spectra and found them to also be in good agreement. I constructed mutant empirical Hamiltonians by computing the site energy shifts of the mutants relative to WT and applying them to the empirical Brixner and Kell Hamiltonians. The first principles spectra performed as good or better than the empirical Hamiltonians in most cases.

Analysis of these modeled structures revealed that the shifts of the site energies were predominantly due to Stark shifts from structural changes of amino acid residues near the pigments. Furthermore, analysis revealed that large structural changes can have minimal spectral impact, and mutations in the pocket of a given pigment can have minimal spectral impact on that pigment. Instead, the transition energy of a pigment is the sum of contributions from many amino acid residues which may cancel each other out to some degree.

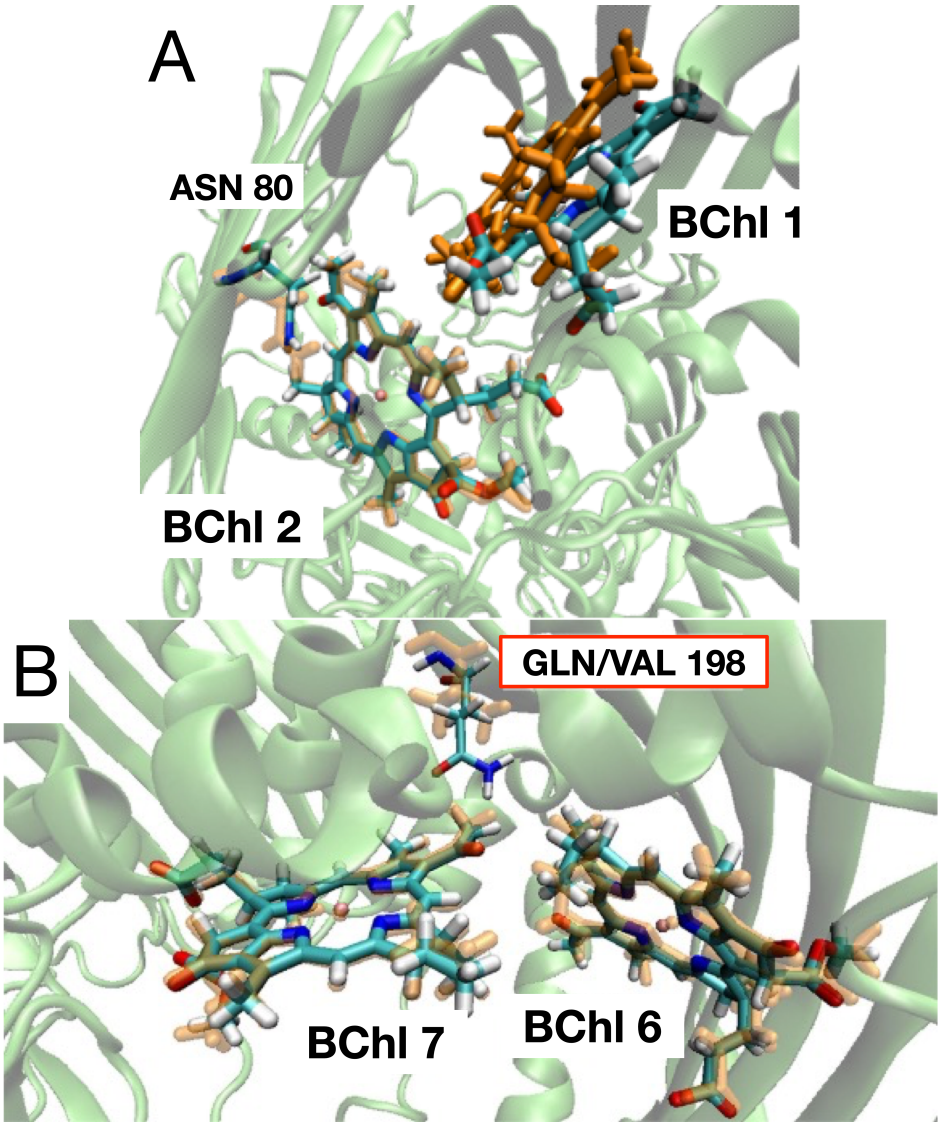

Figure 2.12. Structure of pigment pockets in M7 (solid) compared to WT (transparent). The structures were aligned by minimizing RMS error of the tetrapyrrole rings. A change in the orientation between pigments 1 and 2 (A) produces a noticeable spectral change. Pigment 6 (B) also experiences a large spectral change. The mutation near pigment 7 is outlined in red.

Future work will perform more detailed analysis on the contributions from the amino acids near each pigment for each mutant. This work may inform selection of mutations that produce significant spectral changes without substantial structural modification of the pigment pockets.

3. TIME-RESOLVED CIRCULAR DICHROISM OF THE FENNA-MATTHEWS-OLSON COMPLEX

3.1 Introduction

Time-resolved spectroscopy of the triplet states in FMO have been investigated for decades [37], [40], [41], [55], [57], [62]. Most recently our group has developed a shot-noise limited time-resolved circular-dichroism (TRCD) spectrometer and used it to obtain preliminary TRCD spectra of the FMO complex [41], [63].

The goal of this work is to improve upon the spectrometer developed in [63] and [41] in order to obtain ΔA and ΔA_{CD} spectra of WT FMO in addition to site-directed mutants near pigments 3, 4, and 7 of the FMO complex. The time resolved spectra obtained from these measurements will provide a unique set of high quality experimental data against which predictive modeling techniques may developed that can be applied to other pigment protein complexes. The TRCD spectra obtained here provide extra structural information not found in absorption measurements and thus provide extra checks against simulations.

The FMO complex is well-situated as a test sample for developing excitonic modeling techniques as it contains only 8 pigments yet still has rich excitonic structure. The steady-state spectra and electronic structures have been explored in detail in Chapter 2.

3.2 Materials and Methods

FMO WT, Y16F (pigment 3 mutant, M3), Y345F (pigment 4 mutant, M4), and Q198V (pigment 7 mutant, M7) cultures were prepared as in [60].

Concentrated FMO protein was diluted with CAPS buffer to an optical density (OD) of $\sim$1 OD at the Q_y peak (808 nm) in a 2 mm optical path length fused silica cuvette. Samples were prepared with a 10mM dithionite solution as dithionite has been shown to increase triplet yield [62]. All sample components were deoxygenated using the procedure described in [37] to preserve sample quality under illumination.

Steady state absorption spectra were collected with a Cary Varian 300 spectrophotometer immediately after sample preparation, then before and after transient measurements. Sam-

ples for time-resolved measurements were prepared in 2 mm fused silica cuvettes as described above.

3.2.1 Ellipsometric CD Detection Method

A custom time-resolved circular-dichroism (TRCD) spectrometer was built as described in [41] and further developed to decrease noise and artifacts in the TRCD signal. This system is an improvement to the original design of an ellipsometric detection technique reported by Lewis et. al [42] and has noise performance orders of magnitude better than previous designs [41], [42], [44]. Figure 3.1 shows a block diagram of the system including the improvements to the design in [41].

The ellipsometric detection method can be described using Jones calculus, in which each optical element is represented as a 2×2 matrix acting on a 2-vector representing the x- and y-components of the complex polarization vector. The relevant optical elements here are two crossed polarizers with a stress-plate and a sample between the two polarizers. The sample is assumed to have some CD.

$$\mathbf{E}_{out} = M_{P2} M_S M_{SP} M_{P1} \mathbf{E}_{in} \tag{3.1}$$

If we take P1 to be horizontal and P2 to be vertical M_{P1} and M_{P2} have the following form:

$$M_{P1} = \begin{pmatrix} 1 & 0 \\ 0 & 0 \end{pmatrix} \tag{3.2}$$

$$M_{P2} = \begin{pmatrix} 0 & 0 \\ 0 & 1 \end{pmatrix} \tag{3.3}$$

The CD of the sample is modeled by composing a left-circular absorber and a right-circular absorber with transmissions of k'^2 and k^2 respectively.

$$M_S = M_{RCA} M_{LCA} \tag{3.4}$$

$$M_S = \frac{1}{2}\begin{pmatrix} 2k-\rho & -i\rho \\ i\rho & 2k-\rho \end{pmatrix} \tag{3.5}$$

$$\rho = k - k' \tag{3.6}$$

The stress plate is modeled as a retarder with retardance δ. When angled at $+45°$ the stress plate takes the following form:

$$M_{SP} = \begin{pmatrix} \cos(\delta/2) & i\sin(\delta/2) \\ i\sin(\delta/2) & \cos(\delta/2) \end{pmatrix} \tag{3.7}$$

Composing the optical elements together yields the matrix M:

$$M = \frac{1}{2}\begin{pmatrix} 0 & 0 \\ (\rho\cos(\delta/2) + (2k-\rho)\sin(\delta/2))e^{i\pi/2} & 0 \end{pmatrix} \tag{3.8}$$

From Eq 3.8 we can see that any y-component of the input polarization will vanish and the output polarization will never have an x-component.

$$\mathbf{E}_{out} = M\begin{pmatrix} E_{in,x}e^{i\phi_x} \\ E_{in,y}e^{i\phi_y} \end{pmatrix} \tag{3.9}$$

$$E_{out,y} = E_{in,x}e^{i(\phi_x+\pi/2)}\left((2k-\rho)\sin(\delta/2) + \rho\cos(\delta/2)\right) \tag{3.10}$$

The retardance is typically small, with $\delta \sim 10^{-2}$, so we can Taylor expand the sine and cosines in Eq 3.8. Furthermore, the physical quantity measured by a photodiode is the intensity so we must square the fields.

$$I_{out} = \frac{1}{4}I_0\left(k^2\delta^2 + \rho^2 + 2k\rho\delta - k\rho\delta^2 - \rho^2\delta\right) \tag{3.11}$$

$$I_0 = E_{in,x}^2 \tag{3.12}$$

The quantity ρ is related to ΔA_{CD} via Eq 3.13. For experiments presented in this work $\rho \sim 10^{-4}$ and $\delta \sim 10^{-2}$. We can Taylor expand Eq 3.13 to obtain Eq 3.14.

$$\rho = k\left(1 - e^{1.15 A_{CD}}\right) \tag{3.13}$$

$$\rho = 1.15 k A_{CD} \tag{3.14}$$

By placing Eq 3.14 into Eq 3.11 and dropping higher terms we obtain an expression that relates the input and output intensities to ΔA_{CD}.

$$I_{out} = \frac{k^2 I_0}{4}\left(\delta^2 + 2.3\delta A_{CD}\right) \tag{3.15}$$

Given that k^2 is the transmission the quantity $k^2 I_0$ is the intensity after the sample. This portion of the beam is parallel to the first polarizer and so we refer to it as the "parallel" polarization. The beam passed by the second polarizer is referred to as the "perpendicular" polarization. With this naming scheme Eq 3.14 can be rewritten as Eq 3.16.

$$\frac{I_\perp}{I_\parallel} = \frac{1}{4}\left(\delta^2 + 2.3\delta A_{CD}\right) \tag{3.16}$$

Now consider a change in absorption induced by a pump pulse. By subtracting Eq 3.16 in the "with pump" from the "without pump" case we can obtain an expression for the pump-induced change in CD. In our experiments every measurement is acquired with a pump pulse and the "without pump" data is acquired from the portion of the kinetics captured before the pump pulse arrives. This cuts data acquisition time in half.

$$\left(\frac{I_\perp}{I_\parallel}\right)_{\text{with-pump}} - \left(\frac{I_\perp}{I_\parallel}\right)_{\text{without-pump}} = \frac{2.3\delta}{4}\Delta A_{CD} \tag{3.17}$$

$$\frac{4}{2.3\delta}\left[\left(\frac{I_\perp}{I_\parallel}\right)_{\text{with-pump}} - \left(\frac{I_\perp}{I_\parallel}\right)_{\text{without-pump}}\right] = \Delta A_{CD} \tag{3.18}$$

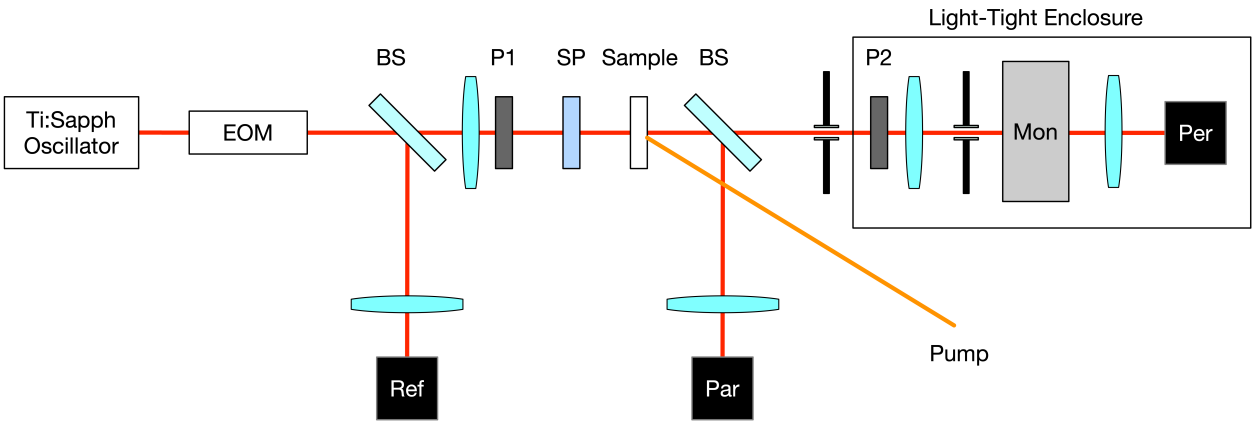

Figure 3.1. Block diagram of the TRCD spectrometer. A stress-plate (SP) is placed after a very high quality polarizer (P1) with the stress-axis 45° relative to P1 to prepare a very slightly elliptically polarized beam prior to the sample. A second high-quality polarizer is crossed relative to P1 and serves to pass the minor axis of the polarization ellipse. The intensity of the minor axis is detected by the "perpendicular" channel (Per). The first beam splitter (BS) directs a portion of the beam towards a "reference" detector which is used to correct for noise. The second beam splitter directs a portion of the beam towards the "parallel" detector (Par) which measures the intensity of the major axis of the polarization ellipse. The lenses and apertures serve to block stray light (dominated by fluorescence) to reduce artifacts in the TRCD signals. The monochromator (Mon) is synchronized with the wavelength of the Ti:Sapph oscillator to only pass through the probe wavelength and block stray light (fluorescence and scattered pump light). All the elements after the first aperture are enclosed in a light-tight box to further prevent stray light from reaching the perpendicular detector.

From Eq 3.18 it would appear that δ *reduces* our sensitivity since $\delta \sim 10^{-2}$. However, the ratio $I_\perp/I_\parallel$ is proportional to δ^2 as shown in Eq 3.19, so there is an enhancement of $1/\delta \sim 10^2$.

$$\delta = \frac{E_y}{E_x} = \sqrt{\frac{I_\perp}{I_\parallel}} \tag{3.19}$$

3.2.2 Experimental Apparatus

The sample is excited at 600 nm with a 5ns laser pulse from a tunable YAG:Nd^{3+} laser (Ekspla NT342B10SH-WW). This excitation wavelength is chosen because all Q_x excitonic bands are overlapping in this spectral region. The pump beam is made larger than the probe beam to ensure that the probe beam is uniformly excited. The intensity of the pump beam is tuned before the experiment to keep the ΔA signal linear in response to the pump.

The probe beam is provided by a custom Ti:Sapph oscillator tunable between 780 nm and 850 nm with a motorized birefringent etalon. An EOM (Conoptics 350-160 with Model 275 driver) after the oscillator blocks the probe between measurements to prevent premature sample degradation. No electrical interference was noticed due to the high-voltage switching of the EOM.

Several improvements were made to the detection system of the spectrometer described in [41]. The oscilloscope configuration at the start of an experiment was automated to the largest degree possible, which uncovered an error in the data collection in [41]. TRCD signals are quite small and exist on top of large DC offsets, and both the CD signal and the laser output vary widely over the range over the range of acquisition wavelengths. This means that the vertical resolution of the oscilloscope will always be suboptimal if set once before the experiment and in fact it was found that digital noise was a limiting factor to our signal to noise ratio. Periodic auto-ranging of each detector channel during the experiment was implemented to allow the optimal vertical resolution to be chosen for each detector during the course of the experiment.

Post-processing of experimental data was automated and performance was improved to such a degree that preliminary fits can now be obtained in an hour instead of days.

It was found that the limiting factor for signal to noise in the perpendicular channel (once stray light is eliminated) is electrical noise in the detector. To this end the perpendicular detector in [41] was replaced with a Thorlabs PDA8A2 detector, which has lower noise and higher gain.

The signals measured in the perpendicular channel are small enough that stray light of any kind can easily obscure them. As mentioned in [41] the detector is placed in a light tight

box to eliminate as much stray light as possible. However, this box was simply polycarbonate with a layer of paint. It was shown that scattered pump light was intense enough to pass through the paint, so the inside and outside of the box were covered in matte black anodized aluminum foil to provide extra shielding.

The high-quality polarizers used before and after the sample are constructed from polarizing prisms in metal housing which are themselves housed in a metal tube. The light that does not pass through the polarizer is reflected to the inside surface of this metal housing, and it was found that some of this light scatters back out of the prism. This scattered light was collected by a nearby lens and focused onto the detector. A mask made of matte black anodized aluminum foil with a small hole for the beam was placed over the back of the polarizer to block this scattered light.

Two other sources of stray light that can obscure the signals are sample fluorescence and pump light that scatters off the sample cuvette. Fluorescence and scattered pump light are both short-lived, but are emitted in all directions and can be intense enough to overload the detector and cause ringing for a short time after excitation. The pump wavelength is far enough away from the probe wavelength that it can be greatly reduced with filters, but fluorescence strongly overlaps with the probe beam during experiments and cannot be removed by filters alone.

The fluorescence and pump light were addressed both spatially and spectrally. A lens with a long focal length is placed before the first polarizer so that the probe beam is focused onto a very small aperture after the sample and right before entering the box. This greatly reduces the solid-angle of scattered light that makes it into the box. Inside of the box (after the polarizer) is a lens and another aperture to block scattered light rays that aren't parallel to the probe beam.

This lens inside the box focuses the beam onto an Optometrics SDMC1-04G motorized monochromator with PCM-02-110 controller, G1200R750QEAS gratings, and 1 mm input and output slits. The computer controlling the experiment synchronizes the monochromator wavelength with the probe wavelength so that the probe beam is passed through and stray light is spectrally filtered. The imaging system of the monochromator also provides a degree of spatial filtering.

A temperature controlled cuvette chiller holding the cuvette at 4°C, where the thermal expansion coefficient of water is zero, did not eliminate the acoustic oscillations reported in [41], so it is likely the circular geometry and very thin windows of the custom cell in [41] that were responsible for eliminating the oscillations. The measurements reported here compensate for the oscillations by collecting measurements at 850 nm, where there are oscillations but no CD signal, then subtracting the averaged oscillations from the measurements at other wavelengths. This practice substantially reduces the effort required to prepare a sample.

Each experiment consisted of 1500 measurements at each wavelength from 780 nm to 850 nm in 2.5 nm increments. Each experiment takes approximately 8 hours.

3.3 Results

Figure 3.2 shows the decay-associated difference spectra (DADS) collected for WT, Y16F (M3), Y345F (M4), and Q198V (M7) FMO.

In this work we have measured the first room-temperature TRCD spectra of FMO mutants. Furthermore, we have produced a unique set of experimental data that can be used to validate the effectiveness of first-principles simulations for predicting transient absorption spectra. Furthermore, we have produced a unique set of experimental data that can be used to develop computational techniques that quantitatively predict the electronic properties of pigments in pigment-protein complexes from first-principles based solely on X-ray crystal structures. Such computational methods need extensive experimental data to validate their results and the FMO complex has proven to be an excellent candidate for a model system.

Triplet lifetimes for WT FMO have been measured previously. The authors of Kihara et al.[37] reported lifetimes of 1 μs, 11 μs, 55 μs, and "long" at 20 K, where the long component is simply outside the measurement range of the system (>>1 ms). The authors also observed 1 μs, 50 μs, and 200 μs lifetimes at room temperature, but the 50 μs component obtained had one broad band with no structure. These lifetimes and an additional 100ns component were also used to fit the data from [41], but excitonic simulations were unable to explain the 100ns spectrum. Here we add TRCD spectra which have both positive and negative bands and carry additional structural information even at room temperature.

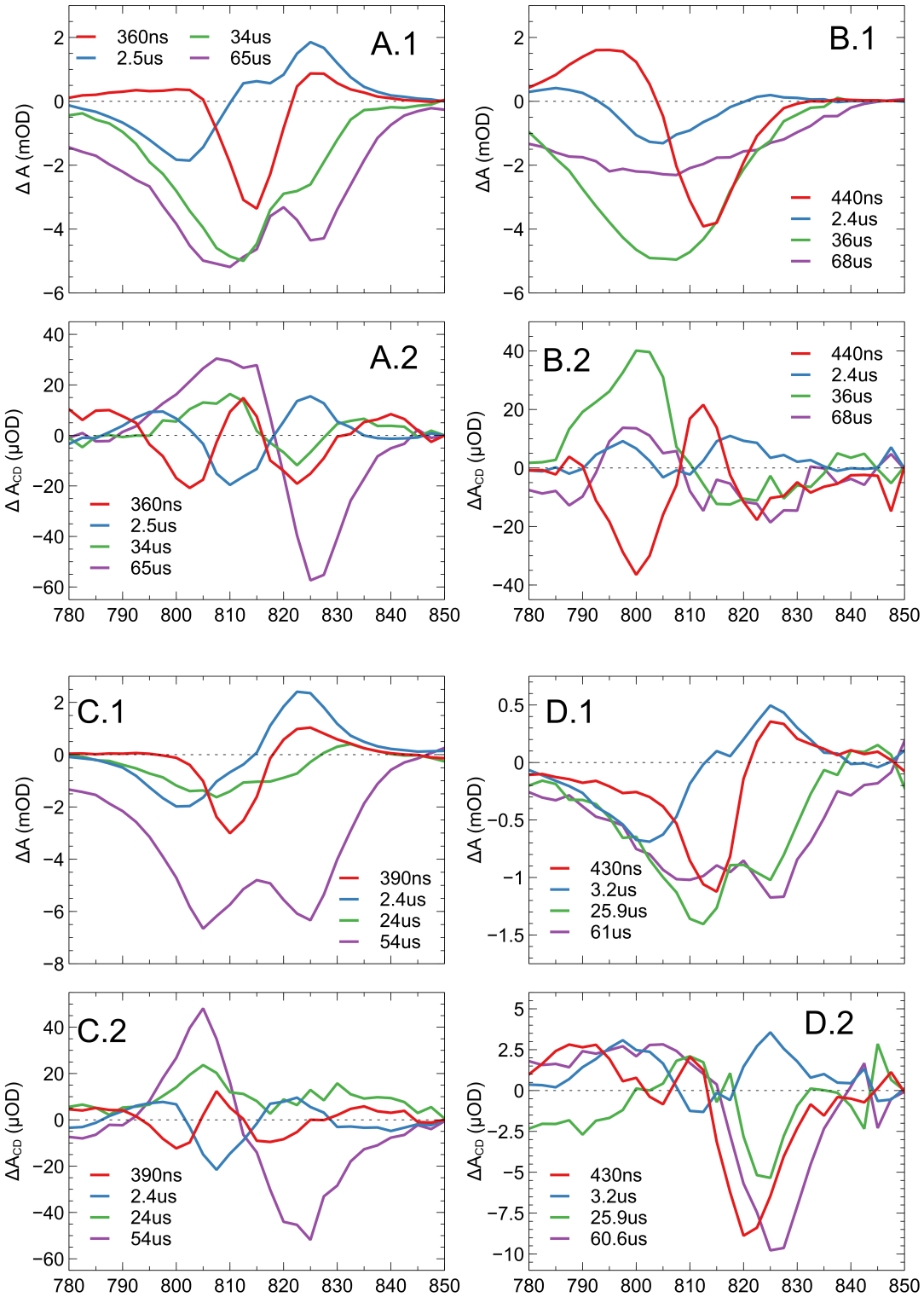

Figure 3.2. ΔA (x.1) and ΔA_{CD} (x.2) DADS spectra for WT (A), M3 (B), M4 (C), and M7 (D) FMO.

The lifetimes reported here were not fixed to match those from previous work, but were instead left as completely free parameters in the global analysis. The lifetimes from all four samples fall into the ranges of ∼400ns, ∼3 μs, ∼30 μs, and ∼60 μs.

In the following sections we will discuss each component of the DADS for each sample.

3.4 Discussion

As mentioned in Section 1.3.3, Dexter energy transfer is viable for energy transfer between closely spaced pigments like those in the FMO complex. Triplet-triplet coupling computations performed by our collaborator Prof. Lyudmila Slipchenko predict that the largest triplet-triplet coupling is on the order of $10^{-2}\,\mathrm{cm}^{-1}$, whereas the singlet-singlet couplings are on the order of 10^{1}–$10^{2}\,\mathrm{cm}^{-1}$. This means that the triplet-triplet couplings between pigments in the FMO complex are very small compared to the singlet-singlet couplings and triplet excitations are effectively localized on a single pigment in contrast with the delocalized singlet excited states. Furthermore, the triplet states in FMO do not strongly interact with other states as the oscillator strength is spread out and is not strongly resonant with the singlet states.

As a result of the weak interactions between triplet states and other states, triplet states have until now been modeled by simply removing the excited pigment from the Hamiltonian. I will show that this is insufficient for accurate modeling of triplet spectra.

Each DADS in Figure 3.2 represents the characteristic change in absorption due to one or more processes occurring at the same rate. In general a DADS could represent energy transfer between pigments, decay of an excited state to the ground state, or some other quenching mechanism. The predicted DADS are found by subtracting $I - F$ where I and F are the absorption spectra of the initial and final states respectively. Figure 3.3 illustrates the simulated DADS one would expect from the a triplet excitation on pigment 3 decaying to the ground state.

One notable difference between the WT data presented in this work and previous measurements is that neither of the longest components, 34μs or 65μs, match the 55μs lifetime found in [37] or [41]. As mentioned earlier, the lifetimes obtained from fits in [37] were set

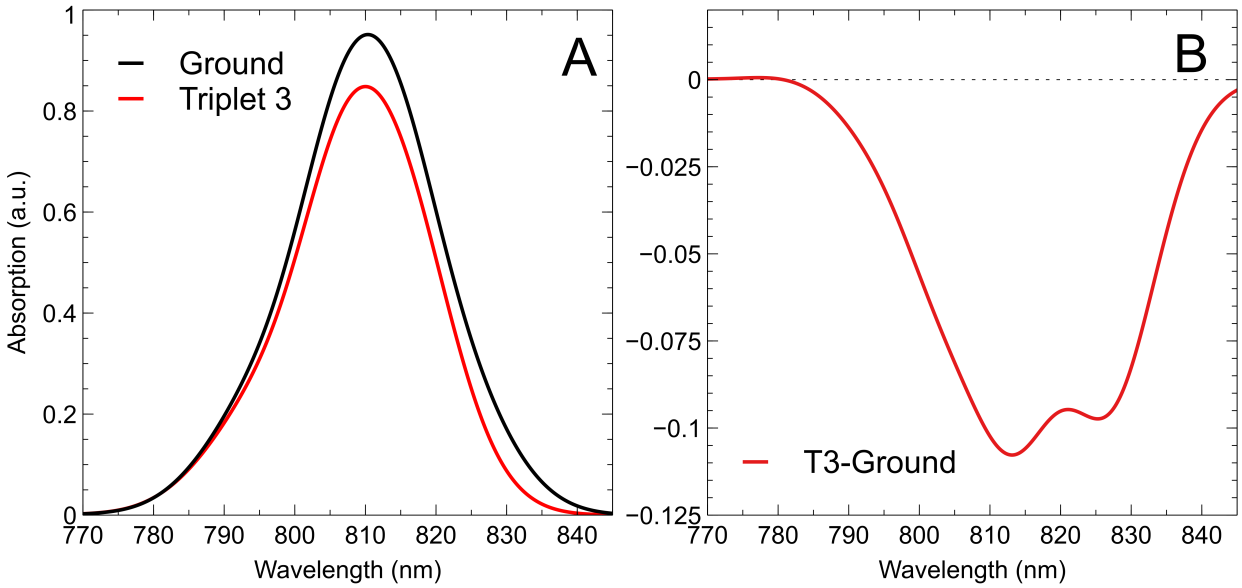

Figure 3.3. Decay-associated difference spectrum (DADS) associated with a triplet excitation on pigment 3 decaying to the ground state. The spectra in (A) are the simulated ground state and triplet excited state absorption spectra. The DADS associated with the decay is shown in (B) and is computed by subtracting the ground state spectrum from the excited state spectrum.

as fixed parameters in the fits computed in [41], so it is reasonable to assume that different lifetimes may have been obtained in [41] had they been left as free parameters. However, the 34μs and 65μs WT components have similar spectra and lifetimes to one another and when averaged present a spectrum remarkably similar to the previous 55μs spectrum. A likely explanation is that these spectra correspond to two different populations in the WT FMO sample. As mentioned in Chapter 2, it is known that pigment 8 may be lost during sample preparation, so these populations may be 7- and 8-pigment complexes. Modeling presented here will present a "55"μs component as an even mix of the 34μs and 65μs components.

Measurements in [37] obtained DADS for the FMO complex at 20 K, and the fit was explained well by a decay of a triplet excitation on pigment 3 to the ground state as shown in Figure 3.4. This makes sense as modeling predicts that pigment 3 is the lowest energy pigment in FMO. The DADS at room temperature, however, was not well explained by the decay of a single pigment as the negative band at 810 nm was missing from the modeled spectrum. This is born out by newly collected data as well, shown in Figure 3.5(A).

It is known that the singlet excited population within FMO reaches a Boltzmann equilibrium within a few picoseconds [64]–[66]. If we approximate an equal probability for each singlet state to enter a triplet state, then a short time after excitation there should be a distribution of triplet states that resembles the singlet state Boltzmann population. The triplet energies are not the same as the singlet energies, thus the Boltzmann population of triplet states will be different from that of the singlet states. The singlet and triplet energies were computed by Prof. Slipchenko from the first-principles structure simulations described in Chapter 2 and were used to compute the Boltzmann populations on each pigment for both singlet and triplet states as shown in Figure 3.6.

From Figure 3.6 it is evident that the population on pigment 3 is substantially larger in the triplet state, meaning that significant energy transfer must take place in order to equilibrate. With this in mind we modeled the decay as Boltzmann-equilibrated triplet populations decaying to the ground state rather than a single triplet decaying to the ground state. The spectrum of the decaying population was computed from a Boltzmann-weighted sum of single-pigment triplet spectra. The result is shown in Figure 3.5(B). The match

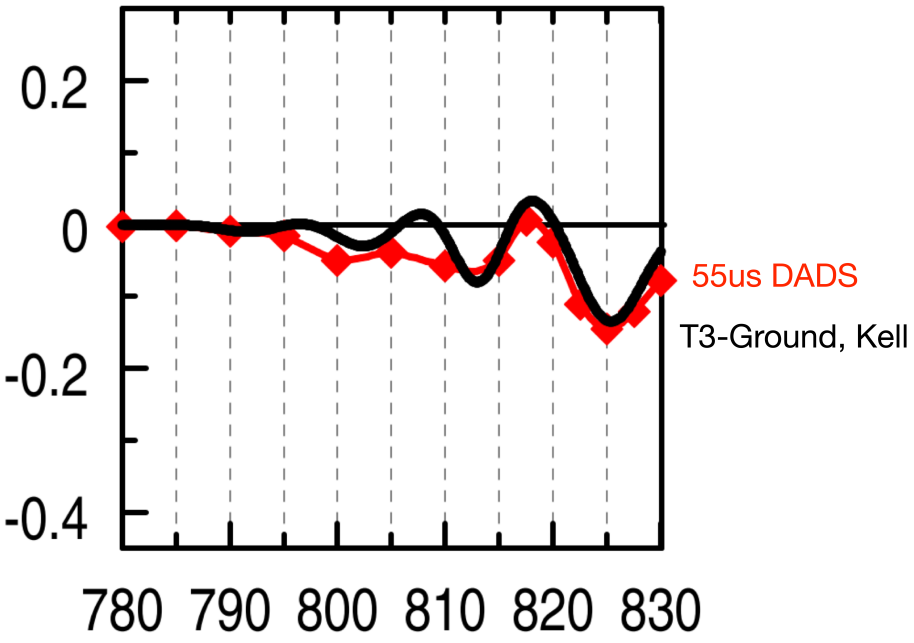

Figure 3.4. DADS of the 55μs component from [37] obtained at 20 K compared with a triplet excitation on pigment 3 decaying to the ground state modeled with the Kell Hamiltonian.

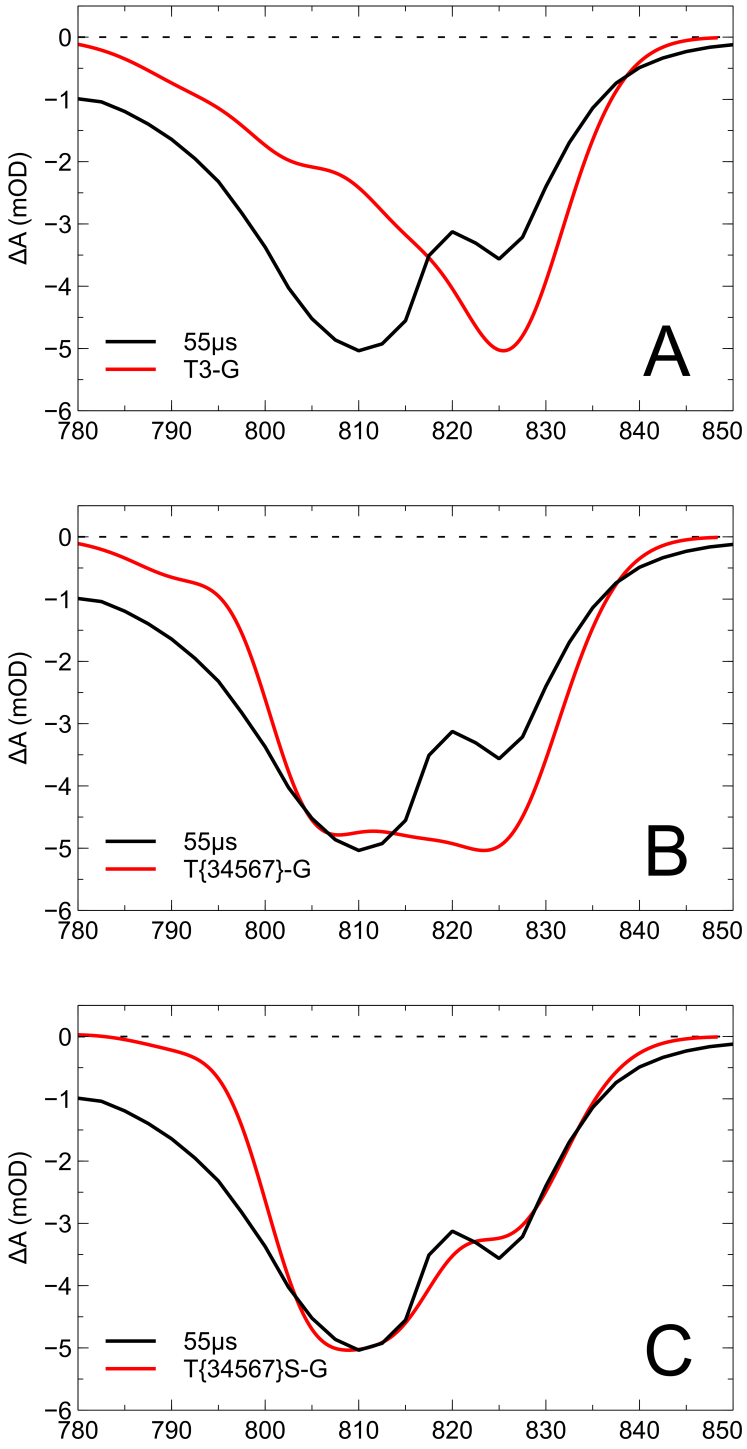

Figure 3.5. Evolution of DADS modeling efforts for the 55μs DADS component of WT FMO, including the decay of triplet 3 to the ground state (A, T3-G), decay of a Boltzmann population of triplet states (B, T{34567}-G), and decay of a Boltzmann population of triplet states experiencing a Stark shift due to triplet 3 (C, T{34567}S-G).

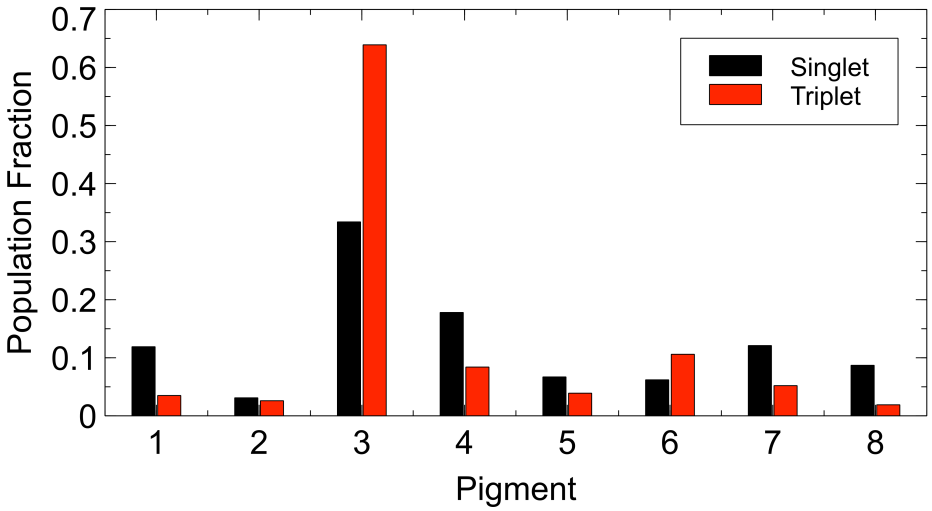

Figure 3.6. Boltzmann populations on the pigments of FMO in singlet and triplet states as computed from first-principles based on 100 snapshots of FMO WT structures for singlet states and 25 for triplet states.

with the experimental data improved substantially, but overestimated the amplitude of the 825 nm band. This indicated that there were still factors unaccounted for in the model.

DFT simulations by Prof. Slipchenko showed that when a BChl *a* pigment enters the triplet state its permanent dipole rotates 90° relative to the ground state. The rotation of the dipole moment causes a change in the electric field surrounding the triplet-excited pigment and thus causes a Stark shift in the surrounding pigments. To account for this effect when computing a triplet we removed the pigment from the Hamiltonian as before but also shifted the energies of the remaining pigments using the Stark shifts computed by Prof. Slipchenko. The results are shown in Figure 3.5(C) and are a near perfect match.

Thus, in modeling the experimental data we have collected, we have advanced the state of the art in predictive modeling by showing that modeling decays of Boltzmann equilibrated populations and accounting for the Stark shift due to triplet-excited pigments are crucial effects to include in future quantitive modeling efforts.

In our analysis we must also take into account which pigments can realistically transfer energy between one another. Table 3.1 shows the relative coupling sizes based solely on the distance between the pigments as described in Section 1.3.3. The non-negligible couplings in wavenumbers are shown in Table 3.2.

Table 3.1. Relative coupling strengths between pigments where couplings have been calculated as $e^{-R/L}$ with $L \approx 1$Å and R equal to the minimum distance found between the pigments.

#1	#2	#3	#4	#5	#6	#7	#8
	2.3E-02	1.0E-05	2.6E-10	1.7E-06	9.7E-03	1.7E-06	2.1E-11
		1.8E-02	1.0E-06	2.9E-08	4.7E-05	8.5E-03	3.3E-12
			2.1E-02	1.7E-04	2.2E-04	3.8E-02	2.3E-11
				2.3E-02	3.8E-06	1.2E-02	1.3E-11
					2.7E-02	1.7E-02	7.0E-08
						1.4E-02	5.3E-07
							3.8E-09

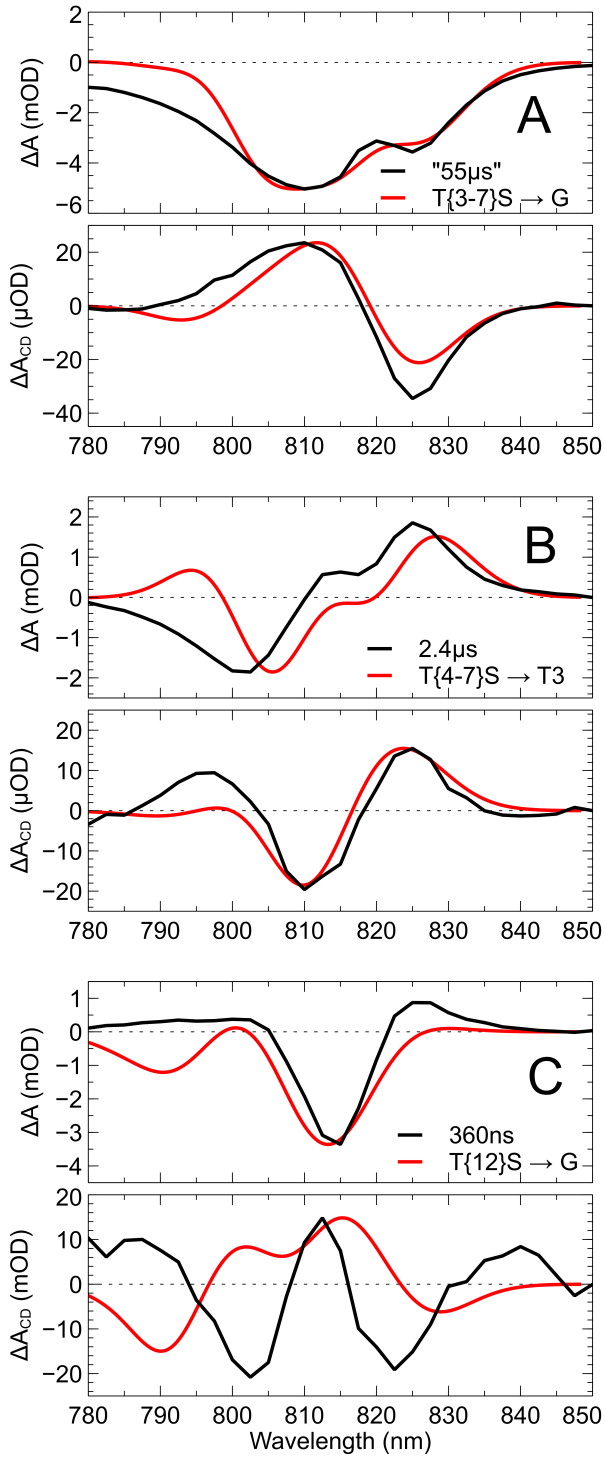

Figure 3.7. Modeled DADS for FMO WT obtained by matching kinetic models with the experimental DADS. **(A)** The "55"μs component was best fit by a decay of triplets on pigments 3–7 to the ground state (T{3-7}S $\rightarrow$ G). **(B)** The 2.4μs component was best fit by energy transfer from pigments 4–7 to pigment 3 (T{4-7}S $\rightarrow$ T3). **(C)** The 360ns component was best fit by a decay of triplets on pigments 1 and 2 to the ground state (T{12}S $\rightarrow$ G).

Table 3.2. Non-negligible triplet-triplet couplings between pigments in the WT FMO complex.

Pigments	Coupling (cm^{-1})
#1 ↔ #2	2.0E-02
#1 ↔ #6	7.6E-04
#3 ↔ #4	8.0E-03
#3 ↔ #7	2.1E-02
#4 ↔ #5	5.4E-03
#4 ↔ #7	1.6E-2
#5 ↔ #6	3.5E-02
#5 ↔ #7	1.7E-03
#6 ↔ #7	4.2E-03

3.4.1 WT FMO

The modeled DADS for the "55"μs, 2.4μs, and 360ns components are shown in Figure 3.7. The models for the 2.4μs and 360ns components were obtained using similar procedures as described above to obtain the model for the "55"μs component. As described above, the "55"μs component is explained by a decay of a triplet excitation on pigment 3 in Boltzmann equilibrium with triplet excitations on pigments 4–7 as well. Pigments 1, 2, and 8 are not included in this Boltzmann population because the coupling between pigments 1/2/8 and the remaining pigments are exceedingly small, meaning that these pigments essentially do not interact with the others. The modeled ΔA_{CD} spectrum of the "55"μs component is in good agreement with the experimental spectrum.

The 2.4μs component is modeled as triplet energy transfer from pigments 4–7 to pigment 3, which makes sense as pigment 3 is the lowest energy pigment in the FMO complex. Both the ΔA and ΔA_{CD} spectra are in very good agreement with the experimental spectra. How pigments 4–7 can be present in the DADS of both the "55"μs and 2.4μs components may not be obvious. As mentioned earlier we know that there must be significant equilibration between pigments 3–7. Pigments 4–7 must equilibrate with each other at a rate much faster than 2.4μs, otherwise there would be another component present in the DADS. Thus there is fast equilibration ($<<$ 2.4μs) between pigments 4–7, while there is also a 2.4μs channel

from pigments 4–7 to pigment 3, and a channel from each of the pigments 3–7 to the ground state ("55"μs).

The 360ns component is modeled as a decay of triplets 1 and 2 to the ground state. This fits with our predictions as the triplet-triplet couplings between pigments 1/2 and 3–8 are vanishingly small while the triplet-triplet coupling between pigments 1 and 2 is nearly the largest in the system. There is good agreement between experimental and modeled ΔA spectra, but the ΔA_{CD} spectra are substantially different. ΔA_{CD} spectra obtained at short times are the most likely to experience artifacts due to fluorescence and scattered pump light. The 360ns component has a similar lifetime to the 100ns lifetime in [41], but the spectral shapes are very different. The amplitude of the 100ns component was much larger than expected and to this date has not been explained. Given the improvements in shielding to the box surrounding the perpendicular detector in this work, it is reasonable to conclude that measurements at early times in [41] are less reliable. The relaxation of the fluorescence- and pump-overloaded perpendicular detector also likely affected the previously measured 100ns lifetime.

3.4.2 M3 FMO

The modeled DADS obtained for M3 are shown in Figure 3.8 and are the first transient ΔA and ΔA_{CD} measurements of an FMO mutant. A mutation near pigment 3 is of particular interest because pigment 3 is the lowest energy pigment and is suspected to be the quencher for triplet excitations in FMO. Therefore one would expect a mutation near pigment 3 to have a significant impact on the lifetime associated with the decay of pigment 3 to the ground state. That the lifetimes obtained for M3 are very similar to WT is surprising.

There are a few notable differences in the "55"μs spectrum as compared to WT. The "55"μs component in M3 is significantly broader than in WT, but the modeled peak matches the peak of the experimental spectrum. The 825 nm band in WT is also missing in M3, but this is not surprising as it is also missing in both experimental and modeled steady state spectra as described in Chapter 2.

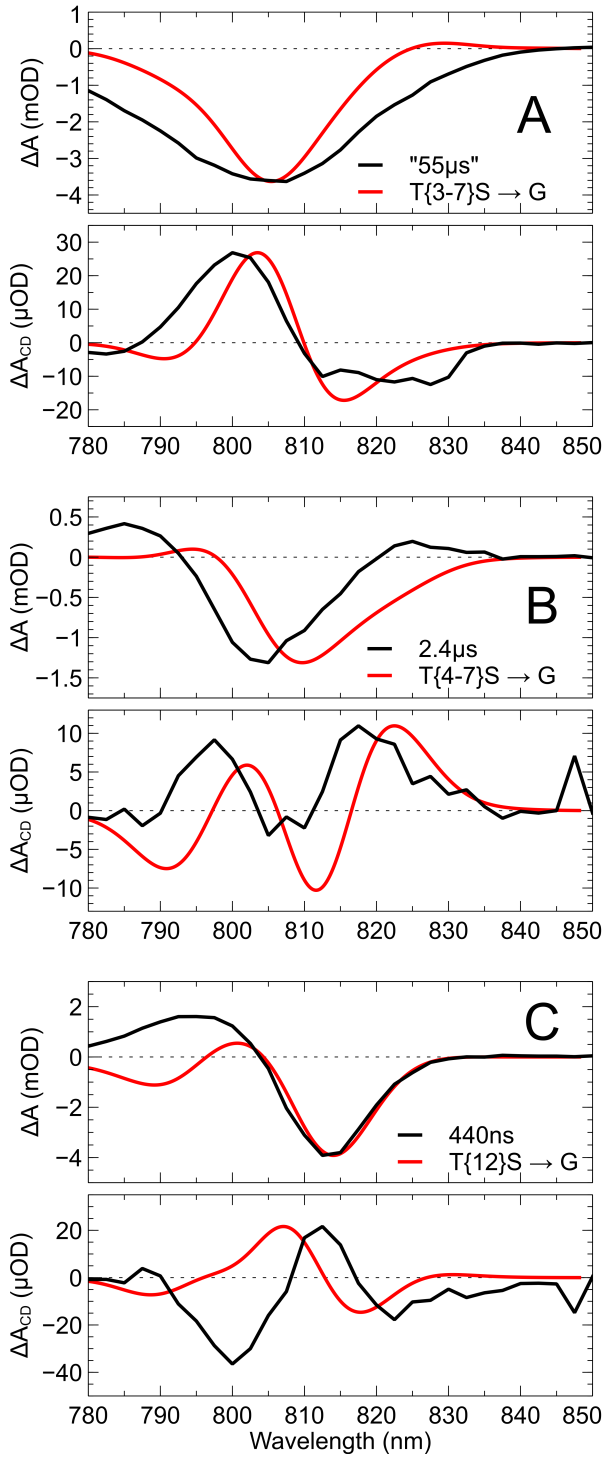

Figure 3.8. Modeled DADS for M3 FMO obtained by matching kinetic models with the experimental DADS. **(A)** The "55"μs component was best fit by a decay of triplets on pigments 3–7 to the ground state (T{3-7}S → G). **(B)** The 2.4μs component was best fit by energy transfer from pigments 4–7 to the ground state (T{4-7}S → G). **(C)** The 430ns component was best fit by a decay of triplets on pigments 1 and 2 to the ground state (T{12}S → G).

Another notable difference is that the 2.4μs component in M3 is explained best by a decay of triplet excitations on pigments 4–7 to the ground state as opposed to triplet energy transfer to pigment 3 in WT. The modeled spectra appear shifted relative to the experimental spectra, and provide good agreement when blue-shifted by 5 nm.

3.4.3 M4 FMO

Simulations of the M4 structures are not yet available, so modeled spectra for M4 could not be computed. The 24μs and 54μs components resemble the long components in WT, but whereas the average of the two lifetimes in WT is $\sim$50μs, the average of the two lifetimes in M3 is $\sim$40μs. The ΔA spectrum of the 2.4μs component bears strong resemblance to the corresponding components in WT and M7. The ΔA_{CD} spectrum is similar to the corresponding components in WT, M3, and M7. The ΔA spectrum of the 390ns component is similar to the other experimental spectra with a broad positive band below 805 nm, a negative band at 815 nm, and a broad positive band above 820 nm. The ΔA_{CD} spectrum resembles that of the corresponding components in WT and M3, but M7 is noticeably different.

3.4.4 M7 FMO

The modeled DADS obtained for M7 are shown in Figure 3.9 and are the first transient ΔA and ΔA_{CD} measurements of an FMO mutant. The M7 sample was challenging experimentally because there was only enough protein for a small number of experiments. The sample was also dilute making for smaller absolute signals.

As with the other samples, the "55"μs component is best explained by a decay of triplet excitations on pigments 3–7 to the ground state. The main difference to WT is that the modeled DADS fails to reproduce the 825 nm band at all in ΔA and fails to match the amplitude in ΔA_{CD}. This is unexpected because the modeled site energy shifts due to the M7 mutation are much smaller than those in M3, and predictions of M7 spectra are expected to be closer to experiment. The experimental spectra of all three components are close to WT, which is expected.

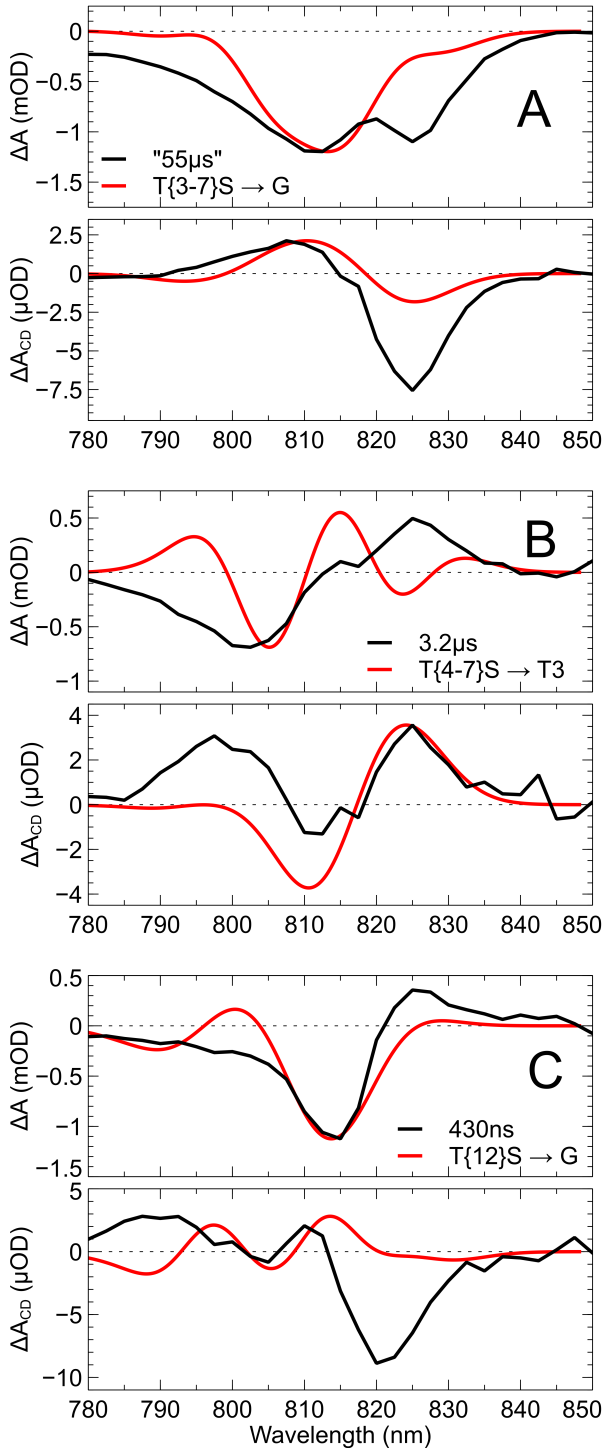

Figure 3.9. Modeled DADS for FMO WT obtained by matching kinetic models with the experimental DADS. **(A)** The "55"μs component was best fit by a decay of triplets on pigments 3–7 to the ground state (T{3-7}S $\rightarrow$ G). **(B)** The 2.4μs component was best fit by energy transfer from pigments 4–7 to pigment 3 (T{4-7}S $\rightarrow$ T3). **(C)** The 360ns component was best fit by a decay of triplets on pigments 1 and 2 to the ground state (T{12}S $\rightarrow$ G).

The 3.2μs component model qualitatively matches the experimental spectrum, but the 825 nm peak in ΔA is split or blue-shifted by 10 nm. As with WT, the 3.2μs component is best explained by triplet energy transfer from pigments 4–7 to pigment 3. The 430ns component is best explained by the decay of triplet excitations on pigments 1 and 2 to the ground state, as with the other samples.

3.5 Conclusion

In this work I enhanced the measurement system developed in [41] and used it to measure ΔA and ΔA_{CD} spectra of FMO mutants for the first time. I used first principles simulations of FMO structures to predict ΔA and ΔA_{CD} spectra for samples whose X-ray crystal structures have yet to be measured and found them to be in good agreement with experimental spectra. With this work we identified that excitonic models are improved by including the site energy shifts due to rotation of the permanent dipole moment upon entering the triplet state.

In the future this measurement system will be used to measure ΔA and ΔA_{CD} spectra of other FMO mutants, with a focus on a mutation near pigment 6. As shown in Chapter 2 spectral features are more easily predicted at low temperature, so future measurements may be conducted at 77 K in order to resolve more spectral features.

Another measurement system targeted at measuring singlet ΔA_{CD} spectra is currently in development. This system uses a heterodyne detection technique in which the amplitude of the pump beam is modulated at frequency ν_1, the handedness of the circularly polarized probe beam is modulated at frequency ν_2, and the resulting CD signal is detected at frequency $\nu_1 + \nu_2$. This detection technique has proved to have exceptional sensitivity when used to measure ΔA spectra, and this newly developed system has shown sensitivity on the order of 10^{-8} OD.

4. TOWARDS SHOT-NOISE LIMITED FEMTOSECOND CIRCULAR-DICHROISM SPECTROSCOPY

4.1 Introduction

Investigation of the rate of charge separation in Photosystem I has been an area of active research for decades due to its speed, efficiency, and implications for designing artificial photosynthetic systems [67], [68]. The intrinsic rate of charge separation is thought to be in the range 0.1–3 ps [69]–[74]. Spectral congestion makes direct measurement of the rate of charge separation impractical. The strong coupling of the special pair P_{700} produces a strong CD signal whereas the remaining Chl *a* pigments in the reaction center have no inherent CD and are far enough apart to have negligible excitonic CD. Time-resolved CD spectrometers have not yet been developed with sufficiently low noise and sufficiently high time resolution to measure the time-resolved CD of the PS I reaction center.

Similarly, the CD of the FMO complex is small enough that work by our group has only recently made time-resolved CD measurements possible. These measurements are on the nanosecond–microsecond timescale, meaning that measurements are restricted to the triplet state dynamics of the FMO complex. The singlet state dynamics of the FMO complex occur on the picosecond timescale, beyond the time-resolution of existing CD spectrometers [64]–[66], [75]–[79]. However, the CD signals in FMO are orders of magnitude smaller than the absorption signals, which are already small on the order of 10^{-5}.

In this work we present the development of a time-resolved CD spectrometer that approaches the shot-noise limit with 20 fs time-resolution.

4.2 Experimental Realization

Time-resolved circular-dichroism (TRCD) measurement techniques so far fall into two categories: absorptive [46], [47], [49], and elliptical [42], [48]. As described in [41] and Chapter 3 the elliptical method provides a background-free measurement, but is very sensitive to polarization artifacts such as optical rotatory dispersion (ORD) or circular birefringence (CB), linear dichroism (LD), and linear birefringence (LB) [80]. The LB and LD effects are

not observed if the observed lifetimes are much longer than the electronic reorganization lifetime of the pigments, and the ORD/CB effect can be mitigated by measuring at two different chiralities of the incident light. At shorter lifetimes the LB and LD effects must be addressed, which may explain why this method has, until recently, only been applied to systems at nanosecond and above timescales and systems with large CD signals.

The absorptive method detects small differences in absorption between left-hand and right-hand circularly polarized light. This method can further be divided based on which beam's polarization is modulated. In one scenario the pump chirality is modulated while the polarization of the probe beam is fixed, in which case the measurement will selectively excite the pigments that have CD in the ground state such as the strongly coupled pigments in P_{700}. In the other scenario the pump polarization is fixed while the chirality of the probe beam is modulated, in which case the measurement will reveal the change in CD due to excitation. Attempts have been made at developing spectrometers using the absorptive method in recent years with mixed success [50], [51], [81]–[84].

Exceptionally low noise transient absorption spectrometers with femtosecond time resolution have been developed using a heterodyne detection technique [64], [85]. In this scheme the intensities of the pump and probe beams are modulated at frequencies ν_{pump} and ν_{probe} respectively. The modulated pump and probe beams are mixed inside the sample, resulting in ΔA signals at the sum and difference frequencies as shown in 4.1.

$$\sin(\nu_{pump}x)\sin(\nu_{probe}x) = \frac{1}{2}\left(\cos((\nu_{pump}-\nu_{probe})x) + \cos((\nu_{pump}+\nu_{probe})x)\right) \tag{4.1}$$

A reference signal at the sum-frequency, $\nu_{ref} = \nu_{pump} + \nu_{probe}$, is generated by mixing the modulation signals. A lock-in amplifier is then used to select the portion of the detected signal that is in phase with the reference signal within a very narrow bandwidth. Noise outside the measurement bandwidth (typically <1 Hz as determined by the lock-in amplifier time constant) is rejected. Furthermore, noise within the measurement bandwidth is rejected if it is not in phase with the reference signal. Thus, this measurement technique leads to very good noise performance, which is essential for measuring small transient CD signals.

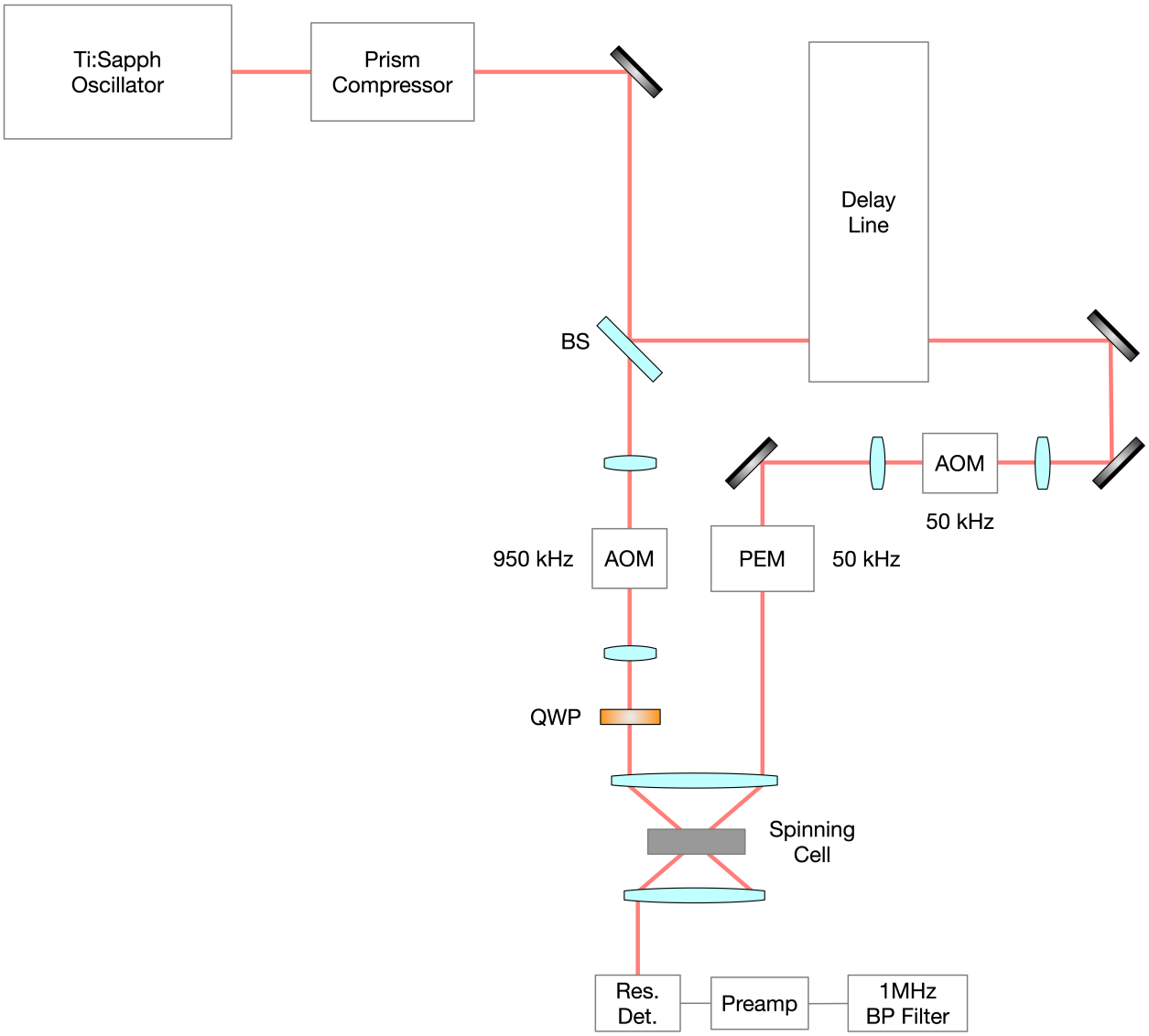

Figure 4.1. Block diagram of MHz system detection system. The system has a time resolution of ∼20 fs.

Our novel femtosecond CD spectrometer is based on this heterodyne detection technique. We refer to it as the "MHz system" as the pulse rate is 80 MHz as determined by the Ti:Sapph oscillator. A block diagram of our spectrometer design is shown in Figure 4.1.

In this design the pump polarization is fixed while the probe beam is modulated. This design allows for either intensity and polarization modulation of the probe beam so that absorption and CD measurements can be conducted with minimal modification to the system. Both pump and probe beams contain acousto-optic modulators (AOMs, Intra-action AOM-

80 with ME-80 driver) to modulate the intensity of each beam. The probe beam also contains a photo-elastic modulator (PEM, Hinds PEM-100) to modulate the polarization of the probe beam between left- and right-hand circularly polarized light. The modulation frequency of the PEM is fixed at 50 kHz. During ΔA measurements the probe AOM is turned on and the PEM is disabled, whereas during ΔA_{CD} measurements the PEM is turned on and the AOM is disabled. Note that it is also possible to modulate the intensity of the beam with just the PEM by placing a quarter-wave plate (QWP) and a polarizer immediately after the PEM. We have chosen to use an AOM so that no mechanical modifications to the system are necessary to switch between ΔA and ΔA_{CD} measurements.

The presence of even a very small ν_{ref} component in either ν_{pump} or ν_{probe} modulation signal produces a background signal with noise larger than the CD signal itself, so it is essential that the ν_{pump} and ν_{probe} signal paths be clean of ν_{ref} to at least 10x smaller than the ΔA or ΔA_{CD} signal being measured. In [85] the detection frequency is chosen to be in a region where the noise of the Ti:Sapph oscillator is low, but in our system ν_{ref} is dictated by both the modulation frequency of the PEM and the availability of electronics. We have chosen ν_{ref} to be 1 MHz due to the availability of high quality custom crystal bandpass filters at this frequency.

The probe detector is resonant at ν_{ref} so that the CD signal is amplified while noise at other frequencies and scattered pump light at ν_{pump} are suppressed. The resonant detector output is passed through a crystal bandpass filter whose pass band is 1 kHz FWHM centered on ν_{ref}, which is then passed to a low-noise pre-amplifier (Ithaco). The pre-amplifier output is then passed to the input of a lock-in amplifier (Stanford Research Systems SR865A).

The modulation signals at $\nu_{pump} = 950$ kHz and $\nu_{probe} = 50$ kHz (for the probe AOM) and the reference signal at $\nu_{ref} = 1$ MHz are produced by custom electronics shown in Figure 4.2. The sequence of amplifiers and attenuators in the signal path serve dual purposes. The first is to adjust the amplitude of the RF signal such that it matches the input range of the AOM driver input ($1\,V_{pp}$) as closely as possible. The second is isolate the ν_{pump} and ν_{probe} signal paths from the ν_{ref} signal path as much as possible. The amplifiers have good isolation between the input and output terminals so a downstream reflection of the ν_{ref} signal will be greatly attenuated.

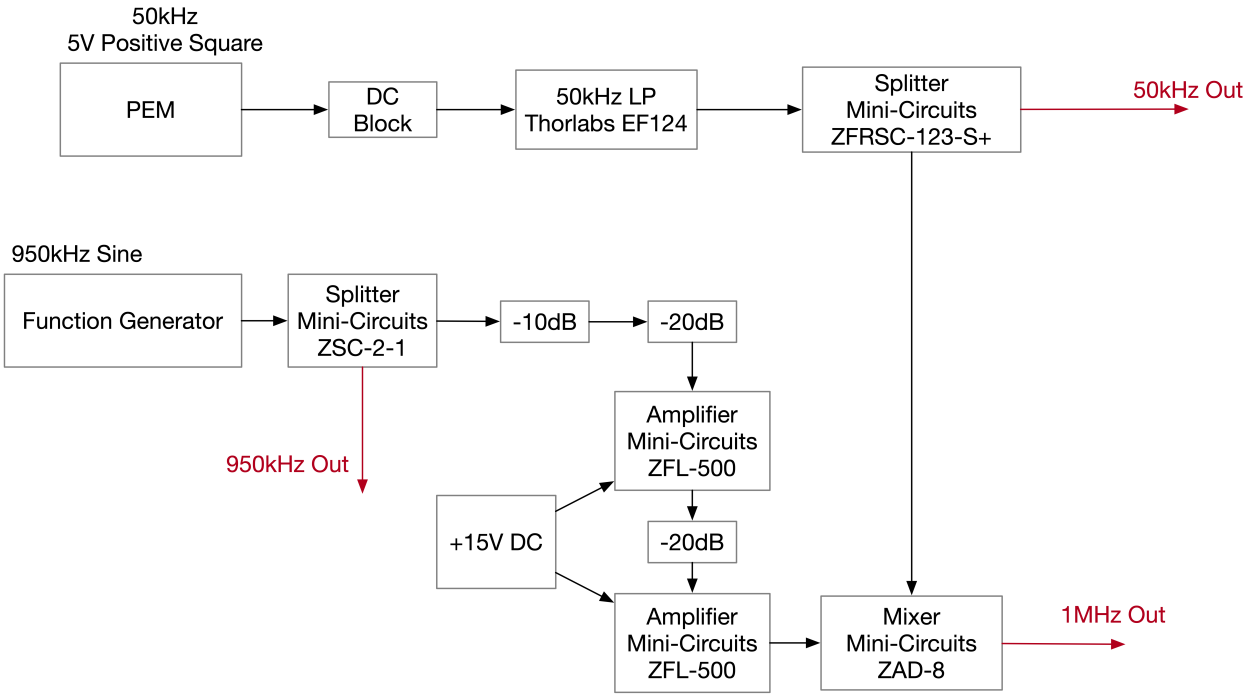

Figure 4.2. Block diagram of MHz system modulation scheme. The 50 kHz and 950 kHz outputs are scaled to provide signals slightly larger than 1 V_{pp}, which is the maximum signal size accepted by the AOM driver inputs without distortion. Variable attenuators are placed on the AOM driver inputs to optimize the modulation signals to provide the largest modulation signal short of distortion.

Several experimental difficulties were encountered in developing this system. The system is designed to measure extremely small signals and therefore is extremely sensitive to even small backgrounds and sources of noise that would be below the noise floor in other systems. These backgrounds may be larger than the signals being measured by this system. What follows is a list of i Low-noise cables improved noise performance by an order of magnitude. Electrical isolation between the modulation signals is critical, as described above.

The pulse rate of this system is 80 MHz, meaning that a pump pulse arrives every 12.5 ns. A stationary sample with a relatively high triplet yield such as FMO would quickly deplete the ground state and no longer produce a measurable ΔA signal. To prevent immediate depletion of the sample we use a spinning cell. By spinning the sample a given sample volume sees a substantially reduced number of pulses in a fixed time period, and the excited molecules in the sample have a chance to return to the ground state.

A spinning cell presents its own experimental difficulties. A sample prepared in a spinning cell is much harder to recover and transfer to another vessel as the interior of the spinning cell has a much larger surface area than the inside of a typical 1 mm cuvette and samples tend to evenly coat the inside of the spinning cell. Vibrations from the spinning cell and motor can travel through the optical table and cause mechanical vibrations in other optical elements. Mechanical vibrations cause a change in the angle of incidence in the beam, which in turns changes the reflectivity at the surface. As the reflectivity changes a beam whose polarization is modulated as in a ΔA_{CD} measurement gains an amplitude modulation. This amplitude modulation produces a background that can be on the same order of magnitude as the ΔA_{CD} signal. The lowest mechanical noise was produced with a drive motor harvested from a DC fan and a flexible rubber O-ring as a drive belt. Mechanical vibrations of optical elements can change the angle of incidence of a beam, which can change the amount of

The alignment of the driveshaft normal to the face of the spinning cell windows is also crucial. Misalignment causes the spinning cell to wobble, which translates the sample volume along the optical axis and can take the sample in and out of the region where the pump and probe beams overlap.

Both the PEM and the AOMs operate by inducing vibrations into a glass element via piezoelectrics. We found that the acoustic oscillations from the PEM element scattered off

of the optical elements in the system and into the pump AOM, causing the two signals to mix and produce a background at ν_{ref}. Sealing the input and output windows of the PEM with fused silica plates prevented the oscillations from escaping the PEM.

The PEM modulates the refractive index in a glass bar with a piezoelectric element that establishes an acoustic standing wave in the glass. The mechanical stress induced by the standing wave causes the refractive index to change. The standing wave and thus the modulation strength has a peak at the center of the bar which falls off with the distance from the center of the bar. This means that alignment of the beam in the center of the bar is critical as misalignment could reduce the modulation from $\pm\lambda/4$ to some fraction of that.

A PEM may not modulate uniformly in both directions out of the box, modulating between $-0.99\lambda/4$ and $1.01\lambda/4$ rather than $\pm\lambda/4$. This was the case with our PEM. The PEM driver modulation offset was recalibrated, but if the driver did not have an adjustable offset a precise adjustable retarder may have been placed after the PEM to achieve the same effect.

The major source of noise is instability of the Ti:Sapph oscillator. Slight misalignment of the oscillator

4.2.1 Results and Discussion

The exceptionally low noise provided by this detection technique makes for a very low transient absorption spectrometer while unlocking TRCD measurements. Using an IR140 laser dye test sample, ΔA as small as 5×10^{-8} OD with noise of 5×10^{-9} OD have been measured with this system as shown in Figure 4.3. Both ΔA and ΔA_{CD} of the IR140 laser dye at 815 nm are shown in Figure 4.4.

4.2.2 Conclusion

In this chapter we have demonstrated a proof of concept femtosecond TRCD spectrometer employing a heterodyne detection technique. The proposed design has measured changes in absorption as small as 5×10^{-8} with noise as small as 5×10^{-9}. This sensitivity is sufficient to measure predicted ΔA_{CD} signal sizes in the FMO complex.

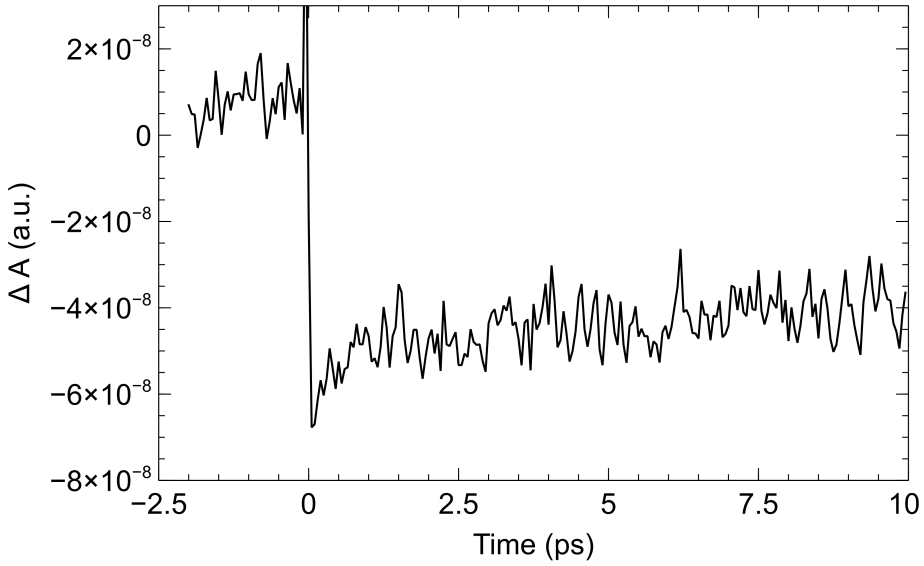

Figure 4.3. Smallest signal measured with the MHz system using IR-140 laser dye as the sample. The signal was measured by reducing the pump modulation intensity until just before the signal disappeared before the signal disappeared. Integration time is 10 s per point.

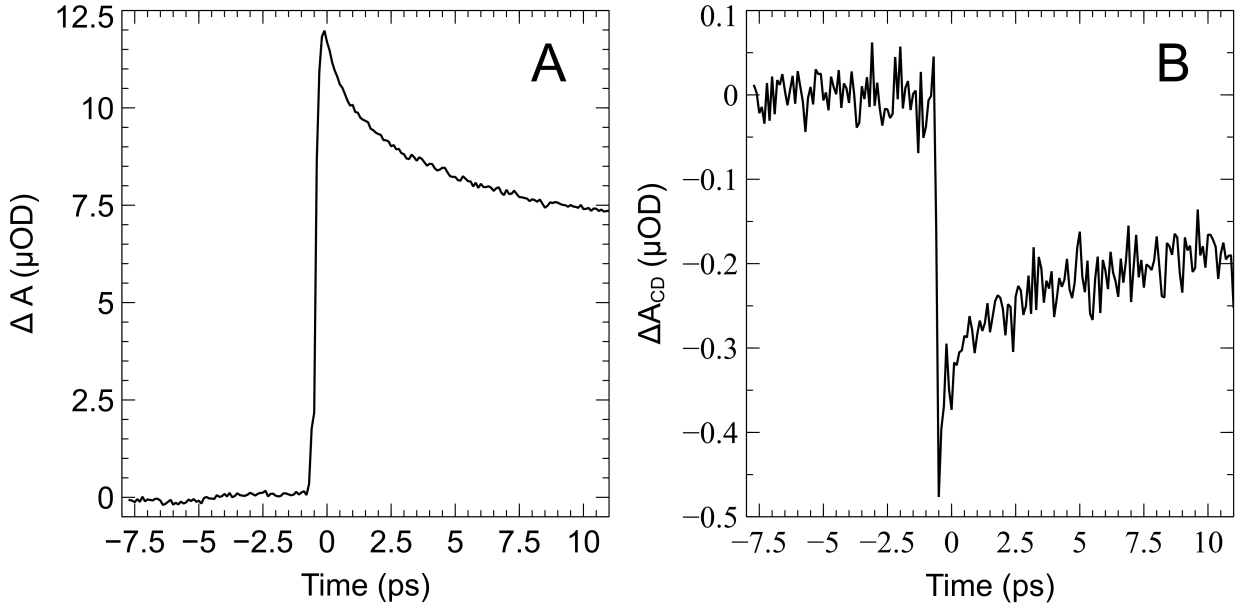

Figure 4.4. ΔA (A) and ΔA_{CD} (B) of the IR140 laser dye at 815 nm as measured with the proposed design with an integration time of 1 s per point.

5. SPECTROSCOPY OF PS I ACCESSORY CHLOROPHYLL MUTANTS

5.1 Introduction

Photosystem I is a pigment-protein complex in plants and cyanobacteria that contains both an antenna complex and a reaction center (RC) [68]. The antenna complex is made up of ∼100 Chl *a* pigments and ∼20 β-carotene pigments. The reaction center contains 6 Chl *a* pigments, 2 phylloquinones (PhQ), and 3 [4Fe-4S] iron-sulfur complexes. The RC is arranged in two pseudo-symmetric branches, labeled A- and B-branch based on which protein subunit (PsaA or PsaB) binds the branch, as shown in Figure 5.1. Electron transfer may proceed down either branch.

The origin of both branches is a pair of Chl *a*/Chl *a'* (Chl *a'* being an epimer of Chl *a*) referred to as the "special pair" P_{700} due to the absorption maximum at 700nm [68], [86]. The notation from [86] encodes both the binding protein subunit and position along the electron transfer chain, so this notation will be used to unambiguously identify the cofactor in question. With this notation, the Chl *a* in the special pair is eC-B1 and the Chl *a'* is eC-A1, and as a pair are referred to as eC-1. The special pair is thought to be the primary electron donor in the RC, losing an electron to the next cofactor along one of the branches upon excitation through energy transfer from the antenna [86]. The special pair is followed by the chlorophylls eC-A2/B2, also referred to as "accessory chlorophylls" or A_{-1} elsewhere in the literature. The pigments eC-A2/B2 are thought to play a role in charge separation, but the pigments themselves have not been identified spectroscopically. The chlorophylls eC-A3/B3 are typically referred to as the "primary electron acceptor" or A_0. The next cofactor along each branch is a phylloquinone (PhQ), labeled PhQ_A/PhQ_B, also referred to as the "secondary electron acceptor" or A_1. The branches meet at the iron-sulfur complexes F_X, F_A, and F_B, referred to as the "terminal electron acceptors." The cofactor F_X is bound by both PsaA and PsaB, whereas F_A and F_B are bound by PsaC [68].

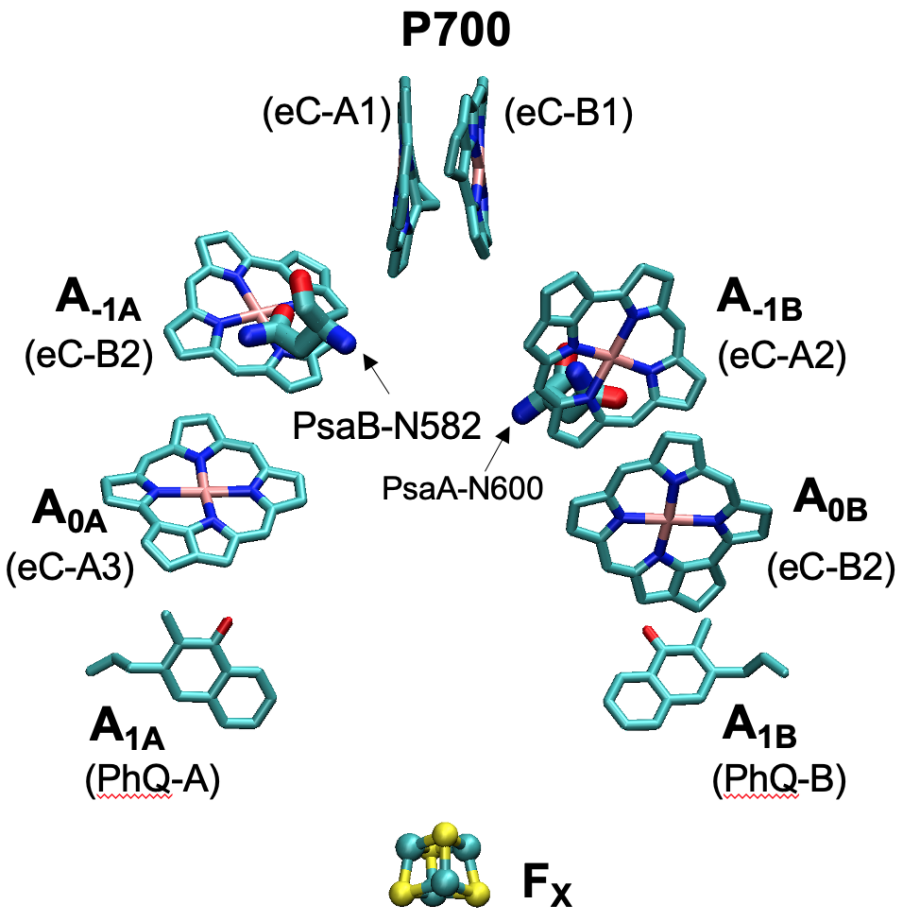

Figure 5.1. Reaction center of cyanobacterial PSI. The amino acid residues PsaA-N600 and PsaB-N582 coordinating the accessory chlorophylls eC-A2 and eC-B2 are shown for reference as well.

5.2 Electron Transfer in the PSI RC

Various time-resolved spectroscopic techniques have been used to examine the rates of steps in the electron transfer (ET) process that occurs in the PSI RC. This system presents difficulties that can be categorized as either temporal or spectral.

The temporal difficulties arise from the fact that when one measures the rate of some process, one necessarily measures the rates of all of the steps preceding it. Thus, the rates measured in experiments are typically referred to as "extrinsic" rates. Extrinsic rates are distinct from the "intrinsic" rates which are defined as the rate just from one cofactor to the next.

The spectral difficulties arise from the fact that PSI contains ∼100 Chl *a* pigments with largely overlapping absorption spectra, despite the wide variety of roles they play in energy and electron transfer in either the antenna or the RC. This is referred to as "spectral congestion."

Progress has been made measuring the rates of various ET steps in the RC despite these challenges. Energy transfer between individual pigments in the antenna have been identified on the order of 0.2 ps [68]. Formation of the charge-separated state $P700^+A_0^-$ has been observed in the range 0.1–3 ps [69]–[74]. The ET step from A_0 to A_1 has been observed in the range 13–50 ps [69]–[71]. The speed of the next ET step from A_1 to F_X depends on the branch, 200 ns for A-branch or 20 ns for B-branch, and the yield depends on the species [87]–[90]. The final ET step from F_X to either F_A or F_B takes 500 ns [69]–[74].

The six Chl *a* pigments in the RC are identical molecules, but the ET steps between them have different rates. The two PhQ cofactors are identical molecules, yet the rate of ET from eC-A3/B3 to $PhQ_{A/B}$ differs by 10x depending on the branch. It follows that the protein environment plays a significant role in determining the properties of the cofactors in the RC.

By replacing the amino acid residue near a cofactor the strength of the interaction between the cofactor and the protein environment may be investigated or intentionally manipulated. Common techniques for performing these measurements are ultrafast optical spectroscopy and electron paramagnetic resonance (EPR). A large number of studies have examined mutations near the eC-3 pigments in both *Synechocystis* sp. PCC 6803 and *Chlamydomonas reinhardtii* [91]–[96]. The central Mg^{2+} of eC-3 coordinates the sulfur atom in the nearby methionine (Met, M) residue. When this Met is replaced with other amino acids, electron transfer past eC-3 is often slowed or blocked entirely. In other studies mutations have allowed PhQ to be replaced with other quinones [97]–[101].

The role of eC-2 is not well understood and has not been studied as extensively as eC-3 or PhQ. The intermediate state between excited special pair and reduced eC-3 is not understood and may involve eC-2 accepting an electron from eC-1 before reducing eC-3 or donating its own electron to eC-3 [102]–[104]. Until recently it was not understood whether the A- and B-

branches operate entirely independently or if the instead compete for the electron produced during charge separation.

To investigate the role of eC-2 on charge separation and electron transfer dynamics, Cherepanov et al. [105] prepared mutants in which one or both of the PsaA-N600 and PsaB-N582 residues were replaced with Met, Leu, or Histidine (His, H). The PsaA-N600 and PsaB-N582 residues are hydrogen bonded to water molecules coordinating the central Mg^{2+} of eC-2B and eC-2A respectively [105].

The authors examined the PsaA-N600H, PsaA-N600L, PsaA-N600M, PsaB-N582H, PsaB-N582L, and PsaB-N582M single mutants in addition to WT via ultrafast spectroscopy. An elaborate analysis technique was used to extract spectra for the excited "long wavelength chlorophylls" (referred to as "red chlorophylls" elsewhere in the literature), the excited special pair $P700^*$, and the charge separated state $P700^+$ eC-2^- from the ΔA spectrum at 100 fs. The analysis from the authors identifies the difference spectrum for reduced eC-2 as having a peak at 688nm. Based on the analysis, the authors also state that the mutants PsaA-N600M and PsaA-N600H significantly reduced the formation of the charge separated state $P700^+$ eC-2^-.

This analysis relies on the pump preferentially exciting the red chlorophylls and P700. The pump was centered on 720nm, which is towards the red edge of the PS I absorption spectrum, but the FWHM of the pump spectrum was 38nm so it is highly unlikely to have preferentially excited the specific pigments mentioned by the authors. Furthermore, previous work on PS I has shown that spectral equilibration is still taking place long after 100 fs, yet spectral equilibration is not included in the analysis from the authors [38], [106], [107].

A study done with the same mutants and an additional PsaA-N600M/PsaB-N582M double mutant was performed by our group using ultrafast spectroscopy and $P_{700}^+ - P_{700}$ steady-state open-closed RC measurements [8]. It was shown that the PsaA-N600M and PsaB-N582M single mutants were spectrally and kinetically very similar to WT as shown in Figure 5.2. The lifetimes of the mutants and WT are within the measurement error of the system. Further measurements were collected at 390nm, where PhQ has an absorption band. Measurements at this wavelength allow direct measurements of PhQ reduction. These measurments showed that the single mutants PsaA-N600M and PsaB-N582M had no signif-

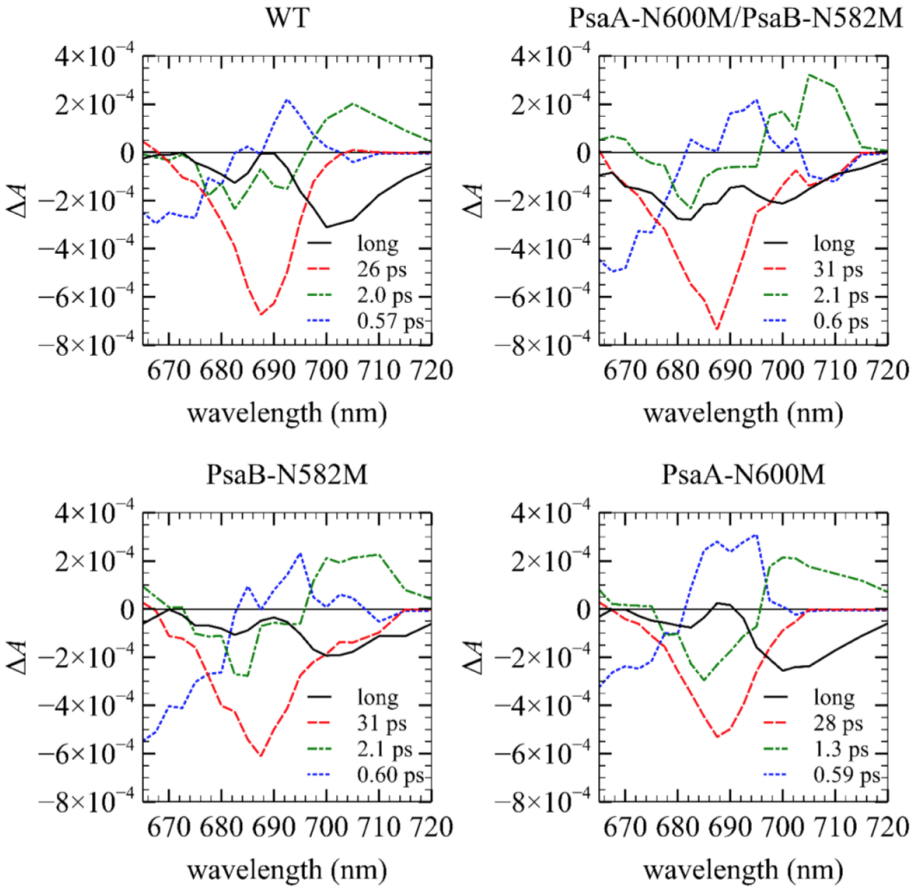

Figure 5.2. Decay associated difference spectra (DADS) for S. sp. PCC 6803 single and double mutants. The spectra and lifetimes in the single mutants are very similar to those of WT, but the double mutant has a much larger peak near 680nm in the long component. Figure from [8].

icant impact on the yield of PhQ reduction, whereas the double mutant decreased the yield by a factor of 3 [8].

While the spectra and lifetimes of the double mutant are largely similar to the WT spectra there is a noticeable difference between the "long" components, which are spectra whose lifetimes exceed the 600 ps measurement window. Comparisons of the $P_{700}^{+} - P_{700}$ spectra for each sample are shown in Figure 5.3. The most noticeable difference is an additional peak near 680nm in the double mutant.

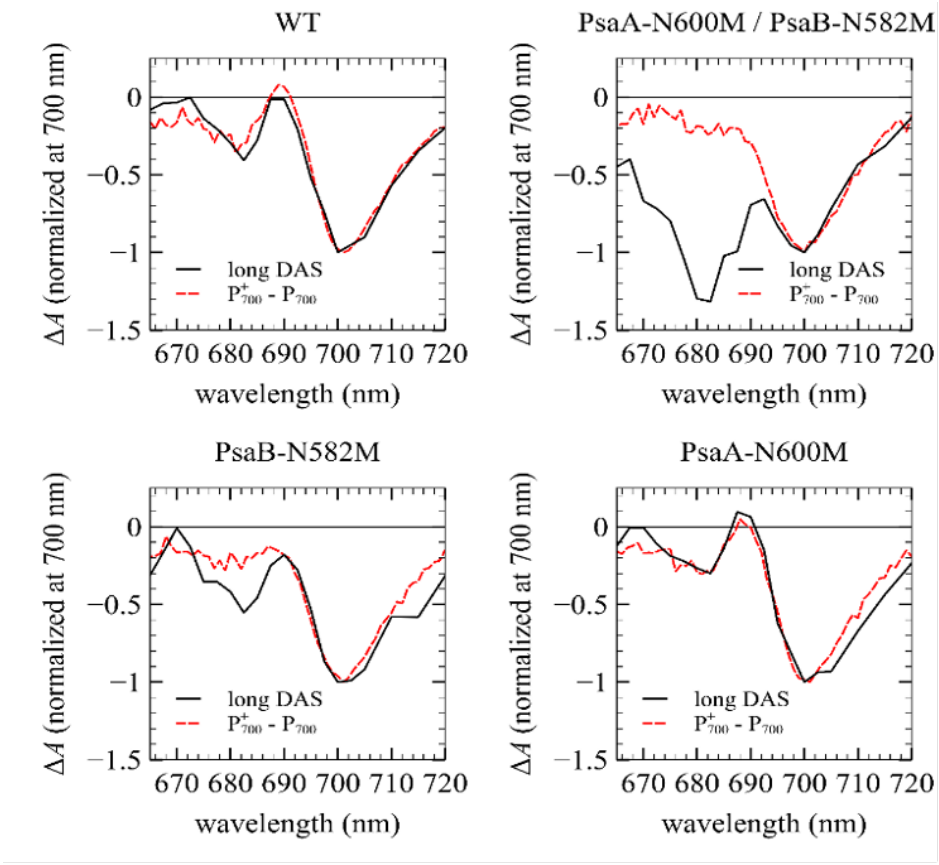

Figure 5.3. A comparison of the longest DADS component (>1ns) to the $P_{700}{}^{+} - P_{700}$ difference spectrum for WT, the PsaB-N582M A-side mutant, the PsaA-N600M B-side mutant, and the PsaB-N582M/PsaA-N600M double mutant. The A-side mutant and double mutant show an additional peak at 682.5nm, the origin of which is under investigation in this work. Figure from [8].

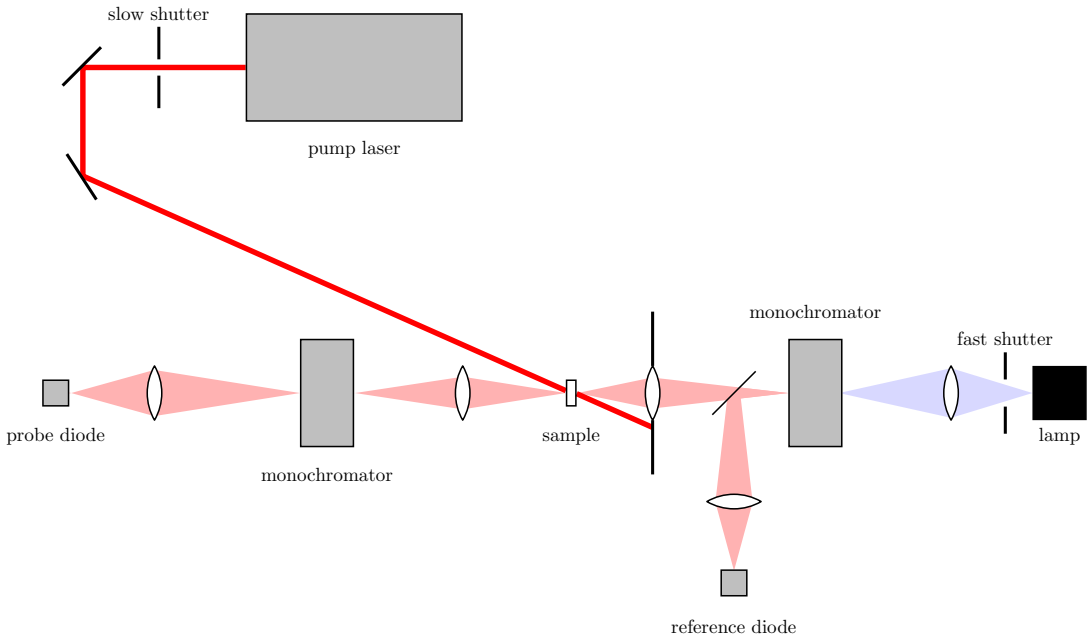

Figure 5.4. Illustration of the experimental apparatus.

5.3 Goals of this Study

From the results of the study in [8] there was still a question as to whether the double mutant "long" component was a single component or multiple components with lifetimes outside the 600 ps measurement window. Measurements on a longer timescale at 682.5nm and 700nm with both WT and the double mutant will reveal whether the peak near 680nm contains components that decay at different rates from WT.

5.4 Materials and Methods

5.4.1 Production of PS I Complexes

The details of purifying, isolating, and characterizing the PS I complexes are covered in [8].

5.4.2 Apparatus

A block diagram of the nanosecond absorption spectrometer is shown in Figure 5.4.

The probe beam is supplied by a pulsed xenon arc lamp (Applied Photophysics LKS 0.60). The 400μs region in which the lamp intensity is roughly constant determines the maximum duration of the measurement window. The sample is protected from the probe beam's constant illumination with a fast shutter (Vincent Associates VS-25 shutter, VCM-D1 driver) that opens for $\sim$1 ms during each measurement. The lamp is pulsed every $\sim$3 seconds, which is limited by the ability of the lamp pulser to dissipate the heat from the huge amount of current required to pulse the lamp. This is the bottleneck for data acquisition.

The pump pulse is provided by a tunable Nd:YAG laser (Ekspla NT342) with 5ns full-width at half-maximum pulse duration. The pump pulse is quite strong, and therefore it is critical for system performance at early times to reduce and contain pump scattering with a beam dump and opaque barriers. A home-built slow shutter alternates between open and closed to perform the with-pump and without-pump measurements respectively. The lamp and shutters are synchronized via the SYNC output of the laser power supply.

A monochromator (Oriel 77250) after the lamp narrows the spectrum of the probe to the region around the measurement wavelength so as not to prematurely degrade the sample with overexposure to probe light. An identical monochromator follows the sample and serves to both set the measurement wavelength and filter out scattered pump light. The width of the exit slit of the monochromator determines the spectral resolution of the measurement. The monochromators are set to each wavelength manually using a fiber spectrometer (Avantes AvaSpec-211C) connected to a computer for calibration.

A fast detector (Thorlabs PDA-10A) placed after the second monochromator records the probe intensity. A beamsplitter after the first monochromator splits the probe beam before the sample and an identical detector records the intensity of this beam. This "reference" detector increases the signal to noise ratio of the measurements by recording changes in probe intensity that are not due to the presence of the sample.

Both detectors are connected to a fast oscilloscope (Tektronix TDS7154B) with a hardware resolution of 1.6ns. The oscilloscope is triggered with a small photodiode near the

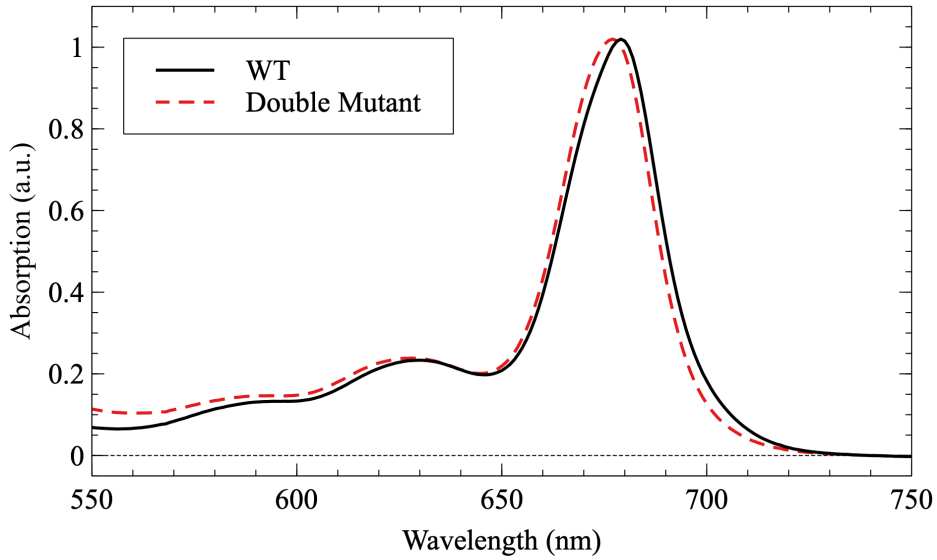

Figure 5.5. Steady state spectra of WT and PsaB-N582M/PsaA-N600M (Double Mutant).

output of the pump laser. The oscilloscope performs math operations on the traces recorded from the two detectors and computes an average ΔA over the course of the experiment. Digital noise is a concern for this system, so it is critical to remove the DC offset of signals and use the smallest vertical resolution possible for optimal signal to noise ratio.

Steady state absorption measurements were recorded with a Varian Cary Bio 300 UV-Vis spectrometer.

5.4.3 Spectroscopic Measurements

Samples were made with the WT and double mutant complexes prepared in 1 mm path length quartz cuvettes with OD of ~0.9 at 680nm. Samples were prepared with a final concentration of 80 mM sodium L-ascorbate (ascorbate) and 80 μM N-Methylphenazonium methyl sulfate (PMS), as in [8], to act as slow and fast reductants respectively. Steady state spectra are shown in Figure 5.5.

As mentioned in [8], the Q_y band is blue-shifted in the mutants, with the most likely explanation being that the mutants lack some of the pigments that absorb on the red side of the Q_y band.

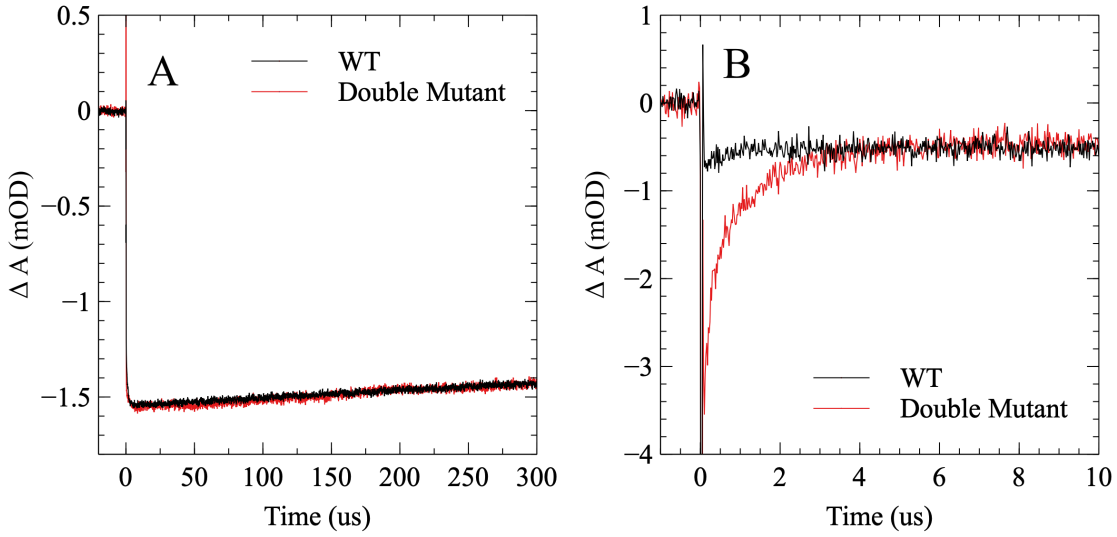

Figure 5.6. Nanosecond measurements of WT and the double mutant (DM) at 700nm (A) and 682.5nm (B). The WT trace in (A) is scaled by 0.615 to match the size of the DM signal and show the high degree of agreement between the kinetics in both samples. Both traces in (A) are smoothed with a moving window 10 points wide in total to further show the agreement. The traces in (B) are not smoothed, but WT is again scaled by 0.615.

Absorption difference traces $\Delta A(t)$ at 700nm and 682.5nm were recorded at 20ns resolution over a 400μs window for each sample. All samples were pumped in the Q_x band at 600nm. The pump beam was kept large enough that the entire probe beam fit inside to ensure that the region of the probe beam was uniformly excited. The measurements at 682.5nm and 700nm are shown in Figure 5.6.

5.5 Results

The ΔA measurements at 700 nm and 682.5 nm are shown in Figure 5.6. It is readily apparent that the dynamics at 700nm are identical, whereas the double mutant has an extra component at 682.5nm. This proves that the peak at 682.5nm in the double mutant is not due to $P700^+$.

5.6 Discussion

The decay at 682.5nm was fit with two major lifetimes: 210ns (51%) and 1.6μs (37%). The presence of two lifetimes suggests either that there are variations in the protein environment around one eC-2 site, or that there are different lifetimes from each branch.

If this peak is due to accumulation of $P700^+$ $eC\text{-}2^-$ then one would expect significant recombination with $P700^+$. The recombination time for $P700^+$ $eC\text{-}3^-$ has been reported to be 25ns [108]. This is an unlikely explanation for this signal as the distance between eC-2 and P700 is much smaller than the distance between eC-3 and P700 and therefore should not be as slow as 210ns or 1.6μs. Furthermore, recombination is an unlikely explanation because the 700nm double mutant kinetics would also contain this extra decay.

The mostly likely explanation is formation of a triplet state. Formation of this triplet state must occur very quickly since experiments in [8] did not detect DADS significantly different from WT. Another piece of evidence supporting this conclusion is that the double mutant did not grow photosynthetically. The amplitude of the 700 nm signal in the DM is ~40% of the WT signal, indicating that ~40% of excitations lead to triplet states. Without photoprotection mechanisms triplet states can generate singlet oxygen which can chemically oxidize and degrade the protein, so a substantial fraction of excitations forming triplet states would explain the growth inhibition [37].

Neither of the single mutants experienced significantly degraded electron transfer. This suggests that the effect of the double mutant is not simply the sum of the effects of the single mutants and that the single mutants effectively redirect electron transfer to the unmodified branch. This also suggests that the excited electron in the reaction center does not hop between branches on its path to the terminal electron acceptor.

5.7 Conclusion

The measurements at 682.5nm and 700nm prove that the peak at 682.5nm from the double mutant in [8] is not from $P700^+$. Furthermore, we have identified strong evidence for the location of the $eC\text{-}2^{-1}$ peak being at 682.5nm, which is significantly different from the previously suggested position of 688nm in [105].

REFERENCES

[1] IEA, *Key World Energy Statistics 2020*. Paris: OECD Publishing, 2020. [Online]. Available: https://www.iea.org/reports/key-world-energy-statistics-2020.

[2] R. K. Pachauri, M. R. Allen, V. R. Barros, *et al.*, *Climate Change 2014: Synthesis Report. Contribution of Working Groups I, II and III to the Fifth Assessment Report of the Intergovernmental Panel on Climate Change*. IPCC, 2014, ISBN: 92-9169-143-7.

[3] Nathan S. Lewis and Daniel G. Nocera, "Powering the Planet: Chemical Challenges in Solar Energy Utilization," *Proc Natl Acad Sci U S A*, vol. 103, no. 43, pp. 15 729–15 735, 2006, ISSN: 0027-8424. DOI: 10.1073/pnas.0603395103.

[4] IEA, *World Energy Outlook 2020*. Paris: OECD Publishing, 2020. [Online]. Available: https://www.iea.org/reports/world-energy-outlook-2020.

[5] T. Johansson, A. Patwardhan, N. Nakicenovic, L. Gomez-Echeverri, and W. Turkenburg, *GEA, 2012 : Global Energy Assessment - Toward a Sustainable Future*. 2012.

[6] M. Tawalbeh, A. Al-Othman, F. Kafiah, E. Abdelsalam, F. Almomani, and M. Alkasrawi, "Environmental impacts of solar photovoltaic systems: A critical review of recent progress and future outlook," *The Science of the total environment*, vol. 759, pp. 143 528–143 528, 2021, ISSN: 0048-9697. DOI: 10.1016/j.scitotenv.2020.143528.

[7] T. Cardona, "Early Archean origin of heterodimeric Photosystem I," *Heliyon*, vol. 4, no. 3, e00548–e00548, 2018, ISSN: 2405-8440. DOI: 10.1016/j.heliyon.2018.e00548.

[8] A. Martin, *Light Reactions of Photosynthesis: Exploring Early Energy and Electron Transfers in Cyanobacterial Photosystem I via Optical Spectroscopy*. 2021.

[9] B. Ke, *Photosynthesis Photobiochemistry and Photobiophysics*. Springer Science & Business Media, 2001, vol. 10, ISBN: 0-7923-6791-X.

[10] B. A. Whitton, *Ecology of Cyanobacteria II: Their Diversity in Space and Time*. Springer Netherlands, 2012, ISBN: 978-94-007-3855-3. [Online]. Available:
.

[11] E. Marschall, M. Jogler, U. Henßge, and J. Overmann, "Large-scale distribution and activity patterns of an extremely low-light-adapted population of green sulfur bacteria in the Black Sea," *Environ Microbiol*, vol. 12, no. 5, pp. 1348–1362, 2010, ISSN: 1462-2912. DOI: 10.1111/j.1462-2920.2010.02178.x.

[12] J. M. Linnanto and J. E. I. Korppi-Tommola, "Investigation on chlorosomal antenna geometries: Tube, lamella and spiral-type self-aggregates," *Photosynth Res*, vol. 96, no. 3, pp. 227–245, 2008, ISSN: 0166-8595. DOI: 10.1007/s11120-008-9304-3.

[13] J. M. Linnanto and J. E. I. Korppi-Tommola, "Exciton Description of Chlorosome to Baseplate Excitation Energy Transfer in Filamentous Anoxygenic Phototrophs and Green Sulfur Bacteria," *J. Phys. Chem. B*, vol. 117, no. 38, pp. 11 144–11 161, 2013, ISSN: 1520-6106. DOI: 10.1021/jp4011394.

[14] R. van Grondelle, J. P. Dekker, T. Gillbro, and V. Sundstrom, "Energy transfer and trapping in photosynthesis," *BBA - Bioenergetics*, vol. 1187, no. 1, pp. 1–65, 1994, ISSN: 0005-2728. DOI: 10.1016/0005-2728(94)90166-X.

[15] S. Sadekar, J. Raymond, and R. E. Blankenship, "Conservation of Distantly Related Membrane Proteins: Photosynthetic Reaction Centers Share a Common Structural Core," *Molecular Biology and Evolution*, vol. 23, no. 11, pp. 2001–2007, Nov. 1, 2006, ISSN: 0737-4038. DOI: 10.1093/molbev/msl079. [Online]. Available: https://doi.org/10.1093/molbev/msl079.

[16] G. S. Orf, C. Gisriel, and K. E. Redding, "Evolution of photosynthetic reaction centers: Insights from the structure of the heliobacterial reaction center," *Photosynthesis Research*, vol. 138, no. 1, pp. 11–37, Oct. 1, 2018, ISSN: 1573-5079. DOI: 10.1007/s11120-018-0503-2. [Online]. Available: https://doi.org/10.1007/s11120-018-0503-2.

[17] N. Hartmann, *Chlorosome*, 2008. [Online]. Available: https://en.wikipedia.org/wiki/File:Chlorosome.PNG.

[18] N.-U. Frigaard and D. A. Bryant, "Complex Intracellular Structures in Prokaryotes," pp. 79–114, 2006, ISSN: 1862-5576. DOI: .

[19] J. M. Olson, "The FMO Protein," *Photosynth Res*, vol. 80, no. 1, pp. 181–187, 2004, ISSN: 0166-8595. DOI: 10.1023/B:PRES.0000030428.36950.43.

[20] Y. Kim, D. Morozov, V. Stadnytskyi, S. Savikhin, and L. V. Slipchenko, "Predictive First-Principles Modeling of a Photosynthetic Antenna Protein: The Fenna–Matthews–Olson Complex," *J. Phys. Chem. Lett*, vol. 11, no. 5, pp. 1636–1643, 2020, ISSN: 1948-7185. DOI: 10.1021/acs.jpclett.9b03486.

[21] B. W. Matthews, R. E. Fenna, M. C. Bolognesi, M. F. Schmid, and J. M. Olson, "Structure of a bacteriochlorophyll a-protein from the green photosynthetic bacterium Prosthecochloris aestuarii," *Journal of molecular biology*, vol. 131, no. 2, pp. 259–285, 1979.

[22] R. E. Fenna and B. W. Matthews, "Chlorophyll arrangement in a bacteriochlorophyll protein from Chlorobium limicola," *Nature*, vol. 258, no. 5536, pp. 573–577, 1975.

[23] C. R. Larson, C. O. Seng, L. Lauman, *et al.*, "The three-dimensional structure of the FMO protein from Pelodictyon phaeum and the implications for energy transfer," *Photosynthesis research*, vol. 107, no. 2, pp. 139–150, 2011.

[24] H. van Amerongen, *Photosynthetic Excitons* (Excitons), red. by L. Valkūnas and R. van Grondelle. Singapore: World Scientific, 2000.

[25] A. V. Ruban, *The Photosynthetic Membrane*, 1. Aufl. New York: Wiley, 2012.

[26] G. Kurisu, H. Zhang, J. L. Smith, and W. A. Cramer, "Structure of the Cytochrome b_6f Complex of Oxygenic Photosynthesis: Tuning the Cavity," *Science*, vol. 302, no. 5647, p. 1009, Nov. 7, 2003. DOI: 10.1126/science.1090165. [Online]. Available: http://science.sciencemag.org/content/302/5647/1009.abstract.

[27] A. S. Davydov, *Theory of Molecular Excitons.* New York: McGraw-Hill, 1962.

[28] W. W. Parson, *Modern Optical Spectroscopy.* Berlin, Heidelberg: Springer Berlin / Heidelberg, 2007. DOI: 10.1007/978-3-540-37542-5.

[29] A. Aubret, M. Orrit, and F. Kulzer, "Understanding Local-Field Correction Factors in the Framework of the Onsager-Bottcher Model," *Chemphyschem*, vol. 20, no. 3, pp. 345–355, 2019, ISSN: 1439-4235. DOI: 10.1002/cphc.201800923.

[30] J. Frenkel, "On the Transformation of light into Heat in Solids. I," *Physical review*, vol. 37, no. 1, pp. 17–44, 1931, ISSN: 0031-899X. DOI: 10.1103/PhysRev.37.17.

[31] J. Peatross and M. Ware, *Physics of Light and Optics*, 2015 Edition. available at optics.byu.edu.

[32] J. A. Schellman, "Circular dichroism and optical rotation," *Chemical Reviews*, vol. 75, no. 3, pp. 323–331, Jun. 1, 1975, ISSN: 0009-2665. DOI: 10.1021/cr60295a004. [Online]. Available: https://doi.org/10.1021/cr60295a004.

[33] G. Zumofen, N. M. Mojarad, V. Sandoghdar, and M. Agio, "Perfect Reflection of Light by an Oscillating Dipole," *Physical Review Letters*, vol. 101, no. 18, p. 180 404, Oct. 29, 2008. DOI: 10.1103/PhysRevLett.101.180404. [Online]. Available: https://link.aps.org/doi/10.1103/PhysRevLett.101.180404.

[34] D. Abramavicius, B. Palmieri, D. V. Voronine, F. Šanda, and S. Mukamel, "Coherent Multidimensional Optical Spectroscopy of Excitons in Molecular Aggregates; Quasiparticle versus Supermolecule Perspectives," *Chemical reviews*, vol. 109, no. 6, pp. 2350–2408, 2009, ISSN: 0009-2665. DOI: 10.1021/cr800268n.

[35] M. Cho, "Coherent Two-Dimensional Optical Spectroscopy," *Chemical reviews*, vol. 108, no. 4, pp. 1331–1418, 2008, ISSN: 0009-2665. DOI: 10.1021/cr078377b.

[36] S. I. E. Vulto, A. M. Streltsov, and T. J. Aartsma, "Excited State Energy Relaxation in the FMO Complexes of the Green Bacterium Prosthecochloris aestuarii at Low Temperatures," *The journal of physical chemistry. B*, vol. 101, no. 24, pp. 4845–4850, 1997, ISSN: 1520-6106. DOI: 10.1021/jp964040u.

[37] S. Kihara, D. A. Hartzler, G. S. Orf, R. E. Blankenship, and S. Savikhin, "The fate of the triplet excitations in the Fenna-Matthews-Olson complex," *J Phys Chem B*, vol. 119, no. 18, pp. 5765–5772, 2015, ISSN: 1520-6106. DOI: 10.1021/jp512222c.

[38] S. Savikhin, W. Xu, P. R. Chitnis, and W. S. Struve, "Ultrafast Primary Processes in PS I from Synechocystis sp. PCC 6803: Roles of P700 and A0," *Biophysical journal*, vol. 79, no. 3, pp. 1573–1586, 2000, ISSN: 0006-3495. DOI: 10.1016/S0006-3495(00)76408-3.

[39] T. J. Aartsma, R. J. Louwe, and P. Schellenberg, "Accumulated photon echo measurements of excited state dynamics in pigment-protein complexes," in *Biophysical Techniques in Photosynthesis*, Springer, 1996, pp. 109–122.

[40] D. A. Hartzler, *Triplet Excitons in Natural Photosynthetic and Artificial Light Harvesting Systems: Measurement and Modeling*, red. by Purdue University. Physics and Astronomy. degree granting institution. Ann Arbor : ProQuest Dissertations & Theses, 2015.

[41] V. Stadnytskyi, *Toward Time-Resolved Circular Dichroism Spectroscopy of Photosynthetic Proteins: Accessing Excitonic States*, red. by Purdue University. Physics and Astronomy. degree granting institution. Ann Arbor : ProQuest Dissertations & Theses, 2017.

[42] J. W. Lewis, R. F. Tilton, C. M. Einterz, S. J. Milder, I. D. Kuntz, and D. S. Kliger, "New technique for measuring circular dichroism changes on a nanosecond time scale. Application to (carbonmonoxy) myoglobin and (carbonmonoxy) hemoglobin," *The Journal of Physical Chemistry*, vol. 89, no. 2, pp. 289–294, 1985.

[43] C. F. Zhang, J. W. Lewis, R. Cerpa, I. D. Kuntz, and D. S. Kliger, "Nanosecond circular dichroism spectral measurements: Extension to the far-ultraviolet region," *The Journal of Physical Chemistry*, vol. 97, no. 21, pp. 5499–5505, 1993.

[44] S. C. Bjorling, C. F. Zhang, D. L. Farrens, P. S. Song, and D. S. Kliger, "Time-resolved circular dichroism of native oat phytochrome photointermediates," *Journal of the American Chemical Society*, vol. 114, no. 12, pp. 4581–4588, 1992.

[45] R. M. Esquerra, R. A. Goldbeck, D. B. Kim-Shapiro, and D. S. Kliger, "Fast time-resolved magnetic optical rotatory dispersion measurements. 1. Mueller analysis of optical and photoselection-induced artifacts," *The Journal of Physical Chemistry A*, vol. 102, no. 45, pp. 8740–8748, 1998.

[46] M. Anson and P. M. Bayley, "Measurement of circular dichroism at millisecond time resolution: A stopped-flow circular dichroism system," *Journal of Physics E: Scientific Instruments*, vol. 7, no. 6, p. 481, 1974.

[47] X. Xie and J. D. Simon, "Picosecond time-resolved circular dichroism spectroscopy: Experimental details and applications," *Review of scientific instruments*, vol. 60, no. 8, pp. 2614–2627, 1989.

[48] X. Xie and J. D. Simon, "Picosecond circular dichroism spectroscopy: A Jones matrix analysis," *JOSA B*, vol. 7, no. 8, pp. 1673–1684, 1990.

[49] X. Xie and J. D. Simon, "A picosecond circular dichroism study of photosynthetic reaction centers from Rhodobacter sphaeroides," *Biochimica et Biophysica Acta (BBA)-Bioenergetics*, vol. 1057, no. 1, pp. 131–139, 1991.

[50] A. Trifonov, I. Buchvarov, A. Lohr, F. Würthner, and T. Fiebig, "Broadband femtosecond circular dichroism spectrometer with white-light polarization control," *Review of Scientific Instruments*, vol. 81, no. 4, p. 043 104, 2010.

[51] K. Hiramatsu and T. Nagata, "Communication: Broadband and ultrasensitive femtosecond time-resolved circular dichroism spectroscopy," *The Journal of Chemical Physics*, vol. 143, no. 12, p. 121 102, 2015.

[52] T. Renger and F. Müh, "Understanding photosynthetic light-harvesting: A bottom up theoretical approach," *Phys Chem Chem Phys*, vol. 15, no. 1, pp. 3348–3371, 2013, ISSN: 1463-9076. DOI: 10.1039/c3cp43439g.

[53] C. Olbrich, T. L. C. Jansen, J. Liebers, *et al.*, "From Atomistic Modeling to Excitation Transfer and Two-Dimensional Spectra of the FMO Light-Harvesting Complex," *J. Phys. Chem. B*, vol. 115, no. 26, pp. 8609–8621, 2011, ISSN: 1520-6106. DOI: 10.1021/jp202619a.

[54] M. T. Milder, M. Milder, B. Brüggemann, R. van Grondelle, and J. L. Herek, "Revisiting the optical properties of the FMO protein," *Photosynth Res*, vol. 104, no. 2-3, pp. 257–274, 2010, ISSN: 0166-8595. DOI: 10.1007/s11120-010-9540-1.

[55] S. I. E. Vulto, M. A. de Baat, R. J. W. Louwe, *et al.*, "Exciton Simulations of Optical Spectra of the FMO Complex from the Green Sulfur Bacterium Chlorobium tepidum at 6 K," *J. Phys. Chem. B*, vol. 102, no. 47, pp. 9577–9582, 1998, ISSN: 1520-6106. DOI: 10.1021/jp982095l.

[56] G. R. Fleming, J. Stenger, R. E. Blankenship, T. Brixner, M. Cho, and H. M. Vaswani, "Two-dimensional spectroscopy of electronic couplings in photosynthesis," *Nature*, vol. 434, no. 7033, pp. 625–628, 2005, ISSN: 0028-0836. DOI: 10.1038/nature03429.

[57] A. Kell, R. E. Blankenship, and R. Jankowiak, "Effect of Spectral Density Shapes on the Excitonic Structure and Dynamics of the Fenna-Matthews-Olson Trimer from Chlorobaculum tepidum," *J Phys Chem A*, vol. 120, no. 31, pp. 6146–6154, 2016, ISSN: 1089-5639. DOI: 10.1021/acs.jpca.6b03107.

[58] A. Kell, X. Feng, M. Reppert, and R. Jankowiak, "On the Shape of the Phonon Spectral Density in Photosynthetic Complexes," *J. Phys. Chem. B*, vol. 117, no. 24, pp. 7317–7323, 2013, ISSN: 1520-6106. DOI: 10.1021/jp405094p.

[59] L. Monticelli and E. Salonen, *Biomolecular Simulations Methods and Protocols* (Methods in Molecular Biology, 924), 1st ed. 2013. Totowa, NJ: Humana Press, 2013, ISBN: 1-62703-017-4. DOI: 10.1007/978-1-62703-017-5.

[60] R. G. Saer, V. Stadnytskyi, N. C. Magdaong, C. Goodson, S. Savikhin, and R. E. Blankenship, "Probing the excitonic landscape of the Chlorobaculum tepidum Fenna-Matthews-Olson (FMO) complex: A mutagenesis approach," *Biochimica et Biophysica Acta (BBA) - Bioenergetics*, vol. 1858, no. 4, pp. 288–296, Apr. 1, 2017, ISSN: 0005-2728. DOI: 10.1016/j.bbabio.2017.01.011. [Online]. Available: https://www.sciencedirect.com/science/article/pii/S0005272817300191.

[61] J. Wen, H. Zhang, M. L. Gross, and R. E. Blankenship, "Native Electrospray Mass Spectrometry Reveals the Nature and Stoichiometry of Pigments in the FMO Photosynthetic Antenna Protein," *Biochemistry*, vol. 50, no. 17, pp. 3502–3511, May 3, 2011, ISSN: 0006-2960. DOI: 10.1021/bi200239k. [Online]. Available: https://doi.org/10.1021/bi200239k.

[62] G. S. Orf, D. M. Niedzwiedzki, and R. E. Blankenship, "Intensity Dependence of the Excited State Lifetimes and Triplet Conversion Yield in the Fenna–Matthews–Olson Antenna Protein," *The journal of physical chemistry. B*, vol. 118, no. 8, pp. 2058–2069, 2014, ISSN: 1520-6106. DOI: 10.1021/jp411020a.

[63] V. Stadnytskyi, G. S. Orf, R. E. Blankenship, and S. Savikhin, "Near shot-noise limited time-resolved circular dichroism pump-probe spectrometer," *Review of scientific instruments*, vol. 89, no. 3, pp. 033 104–033 104, 2018, ISSN: 0034-6748. DOI: 10.1063/1.5009468.

[64] S. Savikhin and W. S. Struve, "Ultrafast Energy Transfer in FMO Trimers from the Green Bacterium Chlorobium tepidum," *Biochemistry*, vol. 33, no. 37, pp. 11 200–11 208, Sep. 1, 1994, ISSN: 0006-2960. DOI: 10.1021/bi00203a016. [Online]. Available: https://doi.org/10.1021/bi00203a016.

[65] S. Savikhin, W. Zhou, R. Blankenship, and W. Struve, "Femtosecond energy transfer and spectral equilibration in bacteriochlorophyll a–protein antenna trimers from the green bacterium Chlorobium tepidum," *Biophysical Journal*, vol. 66, no. 1, pp. 110–113, Jan. 1, 1994, ISSN: 0006-3495. DOI: 10.1016/S0006-3495(94)80769-6. [Online]. Available: https://www.sciencedirect.com/science/article/pii/S0006349594807696.

[66] S. Savikhin, D. R. Buck, and W. S. Struve, "Toward Level-to-Level Energy Transfers in Photosynthesis: The Fenna-Matthews-Olson Protein," *The Journal of Physical Chemistry B*, vol. 102, no. 29, pp. 5556–5565, Jul. 1, 1998, ISSN: 1520-6106. DOI: 10.1021/jp981186f. [Online]. Available: https://doi.org/10.1021/jp981186f.

[67] N. Nelson and W. Junge, "Structure and Energy Transfer in Photosystems of Oxygenic Photosynthesis," *Annual review of biochemistry*, vol. 84, no. 1, pp. 659–683, 2015, ISSN: 0066-4154. DOI: 10.1146/annurev-biochem-092914-041942.

[68] J. H. Golbeck, *Photosystem I: The Light-Driven Plastocyanin: Ferredoxin Oxidoreductase*. Springer Science & Business Media, 2007, vol. 24, ISBN: 1-4020-4256-6.

[69] K. Brettel, "Electron transfer and arrangement of the redox cofactors in photosystem I," *BBA - Bioenergetics*, vol. 1318, no. 3, pp. 322–373, 1997, ISSN: 0005-2728. DOI: 10.1016/S0005-2728(96)00112-0.

[70] K. Brettel and W. Leibl, "Electron transfer in photosystem I," *Biochimica et Biophysica Acta (BBA)-Bioenergetics*, vol. 1507, no. 1-3, pp. 100–114, 2001.

[71] G. Hastings, F. A. Kleinherenbrink, S. Lin, T. J. McHugh, and R. E. Blankenship, "Observation of the reduction and reoxidation of the primary electron acceptor in photosystem I," *Biochemistry*, vol. 33, no. 11, pp. 3193–3200, 1994.

[72] S. Savikhin, "Ultrafast optical spectroscopy of photosystem I," in *Photosystem I*, Springer, 2006, pp. 155–175.

[73] I. V. Shelaev, F. E. Gostev, M. D. Mamedov, *et al.*, "Femtosecond primary charge separation in Synechocystis sp. PCC 6803 photosystem I," *Biochimica et Biophysica Acta (BBA)-Bioenergetics*, vol. 1797, no. 8, pp. 1410–1420, 2010.

[74] N. T. White, G. S. Beddard, J. R. Thorne, T. M. Feehan, T. E. Keyes, and P. Heathcote, "Primary charge separation and energy transfer in the photosystem I reaction center of higher plants," *The Journal of Physical Chemistry*, vol. 100, no. 29, pp. 12 086–12 099, 1996.

[75] M. Maiuri and G. D. Scholes, "2D Spectroscopy Helps Visualize the Influence of Spectral Motion on Chromophore Response," *Chem*, vol. 4, no. 1, pp. 20–21, 2018.

[76] V. R. Policht, A. Niedringhaus, and J. P. Ogilvie, "Characterization of vibrational coherence in monomeric bacteriochlorophyll a by two-dimensional electronic spectroscopy," *The Journal of Physical Chemistry Letters*, vol. 9, no. 22, pp. 6631–6637, 2018.

[77] E. Thyrhaug, K. Zidek, J. Dostál, D. Bína, and D. Zigmantas, "Exciton structure and energy transfer in the Fenna–Matthews–Olson complex," *The Journal of Physical Chemistry Letters*, vol. 7, no. 9, pp. 1653–1660, 2016.

[78] E. Thyrhaug, R. Tempelaar, M. J. Alcocer, *et al.*, "Identification and characterization of diverse coherences in the Fenna–Matthews–Olson complex," *Nature chemistry*, vol. 10, no. 7, pp. 780–786, 2018.

[79] A. Khmelnitskiy, R. G. Saer, R. E. Blankenship, and R. Jankowiak, "Excitonic Energy Landscape of the Y16F Mutant of the Chlorobium tepidum Fenna–Matthews–Olson (FMO) Complex: High Resolution Spectroscopic and Modeling Studies," *The Journal of Physical Chemistry B*, vol. 122, no. 14, pp. 3734–3743, 2018.

[80] S. C. Bjorling, R. A. Goldbeck, S. J. Milder, C. E. Randall, J. W. Lewis, and D. S. Kliger, "Analysis of optical artifacts in ellipsometric measurements of time-resolved circular dichroism," *The Journal of Physical Chemistry*, vol. 95, no. 12, pp. 4685–4694, Jun. 1, 1991, ISSN: 0022-3654. DOI: 10.1021/j100165a018. [Online]. Available: https://doi.org/10.1021/j100165a018.

[81] C. Niezborala and F. Hache, "Measuring the dynamics of circular dichroism in a pump-probe experiment with a babinet-soleil compensator: Erratum," *JOSA B*, vol. 24, no. 4, pp. 1012–1012, 2007.

[82] L. Mangot, G. Taupier, M. Romeo, A. Boeglin, O. Cregut, and K. D. H. Dorkenoo, "Broadband transient dichroism spectroscopy in chiral molecules," *Optics letters*, vol. 35, no. 3, pp. 381–383, 2010.

[83] J. Meyer-Ilse, D. Akimov, and B. Dietzek, "Recent advances in ultrafast time-resolved chirality measurements: Perspective and outlook," *Laser & Photonics Reviews*, vol. 7, no. 4, pp. 495–505, 2013.

[84] J. W. Lewis, R. A. Goldbeck, D. S. Kliger, X. Xie, R. C. Dunn, and J. D. Simon, "Time-resolved circular dichroism spectroscopy: Experiment, theory, and applications to biological systems," *The Journal of Physical Chemistry*, vol. 96, no. 13, pp. 5243–5254, 1992.

[85] P. Anfinrud and W. S. Struve, "Optical shot-noise-limited detection: A single-sideband technique with flexible modulation frequencies," *Rev. Sci. Instrum.; (United States)*, vol. 57, no. 3, pp. 380–383, 1986, ISSN: 0034-6748. DOI: 10.1063/1.1138950.

[86] S. L. Badshah, J. Sun, S. Mula, *et al.*, "Mutations in algal and cyanobacterial Photosystem I that independently affect the yield of initial charge separation in the two electron transfer cofactor branches," *Biochimica et Biophysica Acta (BBA) - Bioenergetics*, vol. 1859, no. 1, pp. 42–55, Jan. 1, 2018, ISSN: 0005-2728. DOI: 10.1016/j.bbabio.2017.10.003. [Online]. Available: https://www.sciencedirect.com/science/article/pii/S000527281730155X.

[87] K. Brettel, "Electron transfer from A- 1 to an iron-sulfur center with t= 200 ns at room temperature in photosystem I Characterization by flash absorption spectroscopy," *FEBS letters*, vol. 239, no. 1, pp. 93–98, 1988.

[88] P. Joliot and A. Joliot, "In vivo analysis of the electron transfer within photosystem I: Are the two phylloquinones involved?" *Biochemistry*, vol. 38, no. 34, pp. 11 130–11 136, 1999.

[89] P. Mathis and P. Sétif, "Kinetic studies on the function of A1 in the Photosystem I reaction center," *FEBS letters*, vol. 237, no. 1-2, pp. 65–68, 1988.

[90] P. Setif and K. Brettel, "Forward electron transfer from phylloquinone A1 to iron-sulfur centers in spinach photosystem I," *Biochemistry*, vol. 32, no. 31, pp. 7846–7854, 1993.

[91] R. O. Cohen, G. Shen, J. H. Golbeck, *et al.*, "Evidence for asymmetric electron transfer in cyanobacterial photosystem I: Analysis of a methionine-to-leucine mutation of the ligand to the primary electron acceptor A0," *Biochemistry*, vol. 43, no. 16, pp. 4741–4754, 2004.

[92] N. Dashdorj, W. Xu, R. O. Cohen, J. H. Golbeck, and S. Savikhin, "Asymmetric electron transfer in cyanobacterial Photosystem I: Charge separation and secondary electron transfer dynamics of mutations near the primary electron acceptor A0," *Biophysical journal*, vol. 88, no. 2, pp. 1238–1249, 2005.

[93] M. D. McConnell, J. Sun, R. Siavashi, *et al.*, "Species-dependent alteration of electron transfer in the early stages of charge stabilization in Photosystem I," *Biochimica et Biophysica Acta (BBA)-Bioenergetics*, vol. 1847, no. 4-5, pp. 429–440, 2015.

[94] S. Santabarbara, K. Reifschneider, A. Jasaitis, *et al.*, "Interquinone electron transfer in photosystem I as evidenced by altering the hydrogen bond strength to the phylloquinone (s)," *The Journal of Physical Chemistry B*, vol. 114, no. 28, pp. 9300–9312, 2010.

[95] J. Sun, S. Hao, M. Radle, *et al.*, "Evidence that histidine forms a coordination bond to the A0A and A0B chlorophylls and a second H-bond to the A1A and A1B phylloquinones in M688HPsaA and M668HPsaB variants of Synechocystis sp. PCC 6803," *Biochimica et Biophysica Acta (BBA)-Bioenergetics*, vol. 1837, no. 8, pp. 1362–1375, 2014.

[96] A. van der Est, S. Chirico, I. Karyagina, R. Cohen, G. Shen, and J. H. Golbeck, "Alteration of the axial Met ligand to electron acceptor A0 in photosystem I: An investigation of electron transfer at different temperatures by multifrequency time-resolved and CW EPR," *Applied Magnetic Resonance*, vol. 37, no. 1, pp. 103–121, 2010.

[97] A. Chauvet, N. Dashdorj, J. H. Golbeck, T. W. Johnson, and S. Savikhin, "Spectral resolution of the primary electron acceptor A0 in photosystem I," *The Journal of Physical Chemistry B*, vol. 116, no. 10, pp. 3380–3386, 2012.

[98] S. Mula, A. Savitsky, K. Möbius, *et al.*, "Incorporation of a high potential quinone reveals that electron transfer in photosystem I becomes highly asymmetric at low temperature," *Photochemical & Photobiological Sciences*, vol. 11, no. 6, pp. 946–956, 2012.

[99] Y. N. Pushkar, I. Karyagina, D. Stehlik, S. Brown, and A. van der Est, "Recruitment of a foreign quinone into the A1 site of photosystem I: Consecutive forward electron transfer from A0 to A1 to FX with anthraquinone in the A1 site as studied by transient EPR," *Journal of Biological Chemistry*, vol. 280, no. 13, pp. 12 382–12 390, 2005.

[100] K. P. Bandaranayake, R. Wang, T. W. Johnson, and G. Hastings, "Time-resolved FTIR difference spectroscopy for the study of photosystem I particles with plastoquinone-9 occupying the A1 binding site," *Biochemistry*, vol. 45, no. 42, pp. 12 733–12 740, 2006.

[101] H. Makita and G. Hastings, "Time-resolved visible and infrared absorption spectroscopy data obtained using photosystem I particles with non-native quinones incorporated into the A1 binding site," *Data in brief*, vol. 7, pp. 1463–1468, 2016.

[102] M. G. Müller, J. Niklas, W. Lubitz, and A. R. Holzwarth, "Ultrafast transient absorption studies on photosystem I reaction centers from Chlamydomonas reinhardtii. 1. A new interpretation of the energy trapping and early electron transfer steps in photosystem I," *Biophysical journal*, vol. 85, no. 6, pp. 3899–3922, 2003.

[103] M. G. Müller, C. Slavov, R. Luthra, K. E. Redding, and A. R. Holzwarth, "Independent initiation of primary electron transfer in the two branches of the photosystem I reaction center," *Proceedings of the National Academy of Sciences*, vol. 107, no. 9, pp. 4123–4128, 2010.

[104] F. Rappaport, B. A. Diner, and K. Redding, "Optical measurements of secondary electron transfer in photosystem I," in *Photosystem I*, Springer, 2006, pp. 223–244.

[105] D. A. Cherepanov, I. V. Shelaev, F. E. Gostev, *et al.*, "Primary charge separation within the structurally symmetric tetrameric Chl2APAPBChl2B chlorophyll exciplex in photosystem I," *Journal of Photochemistry and Photobiology B: Biology*, vol. 217, p. 112 154, Apr. 1, 2021, ISSN: 1011-1344. DOI: 10.1016/j.jphotobiol.2021.112154. [Online]. Available: https://www.sciencedirect.com/science/article/pii/S1011134421000324.

[106] S. Savikhin, W. Xu, V. Soukoulis, P. R. Chitnis, and W. S. Struve, "Ultrafast primary processes in photosystem I of the cyanobacterium Synechocystis sp. PCC 6803," *Biophysical journal*, vol. 76, no. 6, pp. 3278–3288, 1999.

[107] G. Hastings, S. Hoshina, A. N. Webber, and R. E. Blankenship, "Universality of energy and electron transfer processes in photosystem I," *Biochemistry*, vol. 34, no. 47, pp. 15 512–15 522, 1995.

[108] P. V. Warren, J. H. Golbeck, and J. T. Warden, "Charge recombination between P700+ and A1- occurs directly to the ground state of P700 in a photosystem I core devoid of FX, FB, and FA," *Biochemistry (Easton)*, vol. 32, no. 3, pp. 849–857, 1993, ISSN: 0006-2960. DOI: 10.1021/bi00054a016.